F. KÖSEOĞLU

EFFECTS OF SOLUTIONIZING AND AGING CONDITIONS ON THE HARDNESS, MICROSTRUCTURE AND WEAR RESISTANCE OF CAST FE-MN-AL-C-SI LIGHTWEIGHT STEEL

THE GRADUATE SCHOOL OF NATURAL AND APPLIED SCIENCES
OF
ATILIM UNIVERSITY

FATİH KÖSEOĞLU

A MASTER OF SCIENCE THESIS
IN
THE DEPARTMENT OF METALLURGICAL AND MATERIALS ENGINEERING

JUNE 2025

ATILIM UNIVERSITY 2025

EFFECTS OF SOLUTIONIZING AND AGING CONDITIONS ON THE HARDNESS, MICROSTRUCTURE AND WEAR RESISTANCE OF CAST FE-MN-AL-C-SI LIGHTWEIGHT STEEL

A THESIS SUBMITTED TO
THE GRADUATE SCHOOL OF NATURAL AND APPLIED SCIENCES
OF
ATILIM UNIVERSITY

BY

FATİH KÖSEOĞLU

IN PARTIAL FULFILLMENT OF THE REQUIREMENTS
FOR
THE DEGREE OF MASTER OF SCIENCE
IN
THE DEPARTMENT OF METALLURGICAL AND MATERIALS ENGINEERING

JUNE 2025

Approval of the Graduate School of Natural and Applied Sciences, Atılım University.

_____

Assoc. Prof. Dr. Gökhan TUNÇ
Director

I certify that this thesis satisfies all the requirements as a thesis for the degree of the **Master of Sciences in Metallurgical and Materials Engineering, Atılım University**.

_____

Assoc. Prof. Dr. Erkan KONCA
Acting Head of Department

This is to certify that we have read this thesis " EFFECTS OF SOLUTIONIZING AND AGING CONDITIONS ON THE HARDNESS, MICROSTRUCTURE AND WEAR RESISTANCE OF CAST FE-MN-AL-C-SI LIGHTWEIGHT STEEL" submitted by FATİH KÖSEOĞLU and that in our opinion it is fully adequate, in scope and quality as a thesis for the degree of Master of Science.

_____

Assoc. Prof. Dr. Erkan KONCA
Supervisor

Examining Committee Members:

Assoc. Prof. Dr. Ebru SARALOĞLU GÜLER
Department of Mechanical Eng.,
Başkent University _____

Assoc. Prof. Dr. Erkan KONCA
Department of Metallurgical and Materials Eng.,
Atılım University _____

Asst. Prof. Dr. Ozan ÖZKAN
Department of Metallurgical and Materials Eng.,
Atılım University _____

Date: *27.06.2025*

I hereby declare that all information in this document has been obtained and presented in accordance with academic rules and ethical conduct. I also declare that, as required by these rules and conduct, I have fully cited and referenced all materials and rules that are not original to this work.

Name, Last Name: Fatih Köseoğlu

Signature:

ABSTRACT

EFFECTS OF SOLUTIONIZING AND AGING CONDITIONS ON THE HARDNESS, MICROSTRUCTURE AND WEAR RESISTANCE OF CAST FE-MN-AL-C-SI LIGHTWEIGHT STEEL

Köseoğlu, Fatih
MSc., Department of Metallurgical and Materials Engineering
Supervisor: Assoc. Prof. Dr. Erkan Konca

June 2025, 121 pages

This study aimed to investigate the effects of solutionizing and aging treatments on the mechanical properties and microstructure of an experimentally cast Fe-Mn-Al-C-Si lightweight steel of austenite matrix. Castings of target composition were made with a density of 6.60 g/cm³. Solutionizing treatments were applied at 950°C-1150°C for 2, 4, and 16 hours, followed by aging at temperatures ranging from 400°C to 700°C for 4, 16, and 64 hours. Macro/nano hardness measurements, optical microscopy, electron microscopy with energy-dispersive spectroscopy, electron backscatter diffraction, x-ray diffraction analyses, and wear tests were performed to evaluate the effects of heat treatments. Based on the obtained data, it was found that solution treatment at 1000°C for 4 hours prior to aging provided the optimum results in terms of microstructural stability and mechanical properties. Aging for 16 hours within the 400°C–700°C temperature range was suggested as the most promising condition, particularly for hardness improvement. Notably, aging treatments resulted in the formation of κ-carbides within the microstructure, contributing to hardness enhancement. However, aging for even longer times induced undesirable grain boundary precipitations, which adversely affected the mechanical properties.

Keywords: Fe-Mn-Al-C-Si, Lightweight Steel, Low Density, κ-carbide, Solutionizing, Aging, Precipitation, Wear

ÖZ

ÇÖZÜNDÜRME VE YAŞLANDIRMA KOŞULLARININ DÖKÜM FE-MN-AL-C-Sİ HAFİF ÇELİĞİNİN SERTLİK, İÇYAPI VE AŞINMA DİRENCİNE ETKİLERİ

Köseoğlu, Fatih
Yüksek Lisans, Metalurji ve Malzeme Mühendisliği Bölümü
Tez Yöneticisi : Doç. Dr. Erkan Konca

Haziran 2025, 121 sayfa

Bu çalışma, çözündürme ve yaşlandırma ısıl işlemlerinin östenit matrisli deneysel döküm Fe-Mn-Al-C-Si hafif çeliğinin mekanik özellikleri ve içyapısı üzerine etkilerini incelemeyi amaçlamıştır. Hedeflenen kompozisyonda ve 6,60 g/cm³ yoğunluğunda dökümler yapılmıştır. Çözündürme işlemleri 950°C-1150°C arasında 2, 4 ve 16 saat uygulanmış, ardından 400°C ile 700°C arasında 4, 16 ve 64 saat yaşlandırma işlemleri gerçekleştirilmiştir. Isıl işlemlerin etkilerini değerlendirmek amacıyla makro/nano sertlik ölçümleri, optik mikroskopi, enerji saçılım spektroskopisi ve elektron geri saçılma kırınımı ile donatılmış elektron mikroskobu, x-ışını kırınım analizleri ve aşınma testleri yapılmıştır. Elde edilen verilere göre, yaşlandırma öncesinde 1000°C'de 4 saat süreyle uygulanan çözündürme ısıl işleminin iç yapısal kararlılık ve mekanik özellikler açısından en uygun sonucu verdiği görülmüştür. 400°C–700°C sıcaklık aralığında 16 saat süreyle uygulanan yaşlandırmanın özellikle sertlik artışı açısından en uygun koşul olduğu söylenebilir. Yaşlandırma işlemleri içyapı içerisinde sertlik artışına katkıda bulunan κ-karbürlerin oluşumuyla sonuçlanmıştır. Ancak, yaşlandırmanın çok uzun süreyle yapılması mekanik özellikleri olumsuz etkilemesi nedeniyle istenmeyen tane sınırı çökeltilerinin oluşumuna yol açmıştır.

Anahtar Kelimeler: Fe-Mn-Al-C-Si, Hafif Çelik, Düşük Yoğunluk, κ-karbür, Çözündürme, Yaşlandırma, Çökelme, Aşınma

To my family…

ACKNOWLEDGMENTS

First and foremost, I would like to express my sincere gratitude to my supervisor, Assoc. Prof. Dr. Erkan Konca, for his continuous encouragement and support in my research and learning throughout my graduate studies.

I would like to express my gratitude to Akdaş Döküm for providing all the necessary materials, tests, and support for my thesis. In particular, I am deeply thankful to Mehmet Niyazi Akdaş, Necdet Akdaş, R&D Director Ayşe Gül Mangan, and the R&D team members Uğur Kuruoğlu, Berkay Yılmaz, Yağmur Laleci, Alperen Çolak, Beyza Onaran and Miraç Akhan for their goodwill and positive approach throughout this process. I would also like to thank the Akdaş Döküm Quality Department, Atılım University Metal Forming Center of Excellence, and Tenmak Boren for their ongoing support throughout my thesis work.

A special thank you goes to my friend Can Zümrüt, with whom I walked this path together. His unwavering support and positive approach were invaluable, and without him, this thesis could not have been completed on time.

Finally, I extend my deepest gratitude to my family and friends for their unwavering support and encouragement throughout this journey.

TABLE OF CONTENTS

LIST OF FIGURES

FIGURES

LIST OF TABLES

TABLES

LIST OF ABBREVIATIONS

AHSS	Advanced High Strength Steel
DP	Dual Phase
EBSD	Electron Backscatter Diffraction
EDM	Electrical Discharge Machining
EDS	Energy Dispersive Spectroscopy
HB	Brinell Hardness
HV	Vickers Hardness
SEM	Scanning Electron Microscope
ST	Solutionizing Treatment
TRIP	Transformation Induced Plasticity
TWIP	Twinning Induced Plasticity
UTS	Ultimate Tensile Strength
HB	Brinell Hardness
HV	Vickers Hardness

CHAPTER 1

INTRODUCTION

1.1. The Need for and Concept of Lightweight Steels

One of the major fields of focus in recent years has been the development of Advanced High Strength Steels (AHSS) with high strength and good ductility, such as, TRIP, TWIP, and DP (*Figure 1.1*). They have a similar density to conventional steels but exhibit higher formability and superior mechanical properties. These features make AHSS steels attractive in many areas and they continue to evolve.

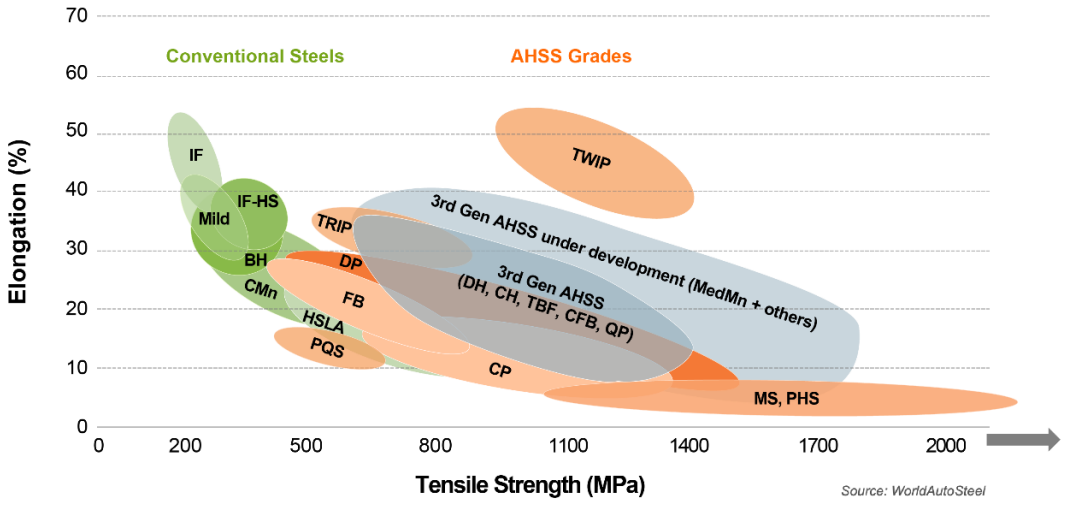

Figure 1.1 Strength and elongation of developing and existing steel grades compared in the 2021 Global Formability Diagram [1]

The superior formability of advanced steels allows for the development of more competitive and innovative products. These materials provide the necessary strength in thinner cross-sections and structures across various industries. This capability leads to the creation of environmentally friendly products that require less raw material for long-term use.

As many countries strive for carbon neutrality, a key requirement is that products produced have longer lifespans and are lightweight. AHSSs play a crucial role in meeting these requirements. For example, if traditional steel used in automobiles is replaced with AHSS, which has a similar density but superior mechanical properties, vehicles can be made lighter while still meeting safety standards. Lighter vehicles contribute to reduced gasoline and electricity consumption, leading to less environmental pollution. Additionally, the decrease in fuel consumption plays a significant role in lowering CO_2 emissions, ultimately making a valuable contribution towards achieving carbon neutrality. As illustrated in *Figure 1.2*, the development of more environmentally friendly products is crucial, particularly given the significant increase in CO_2 emissions since the 1950s.

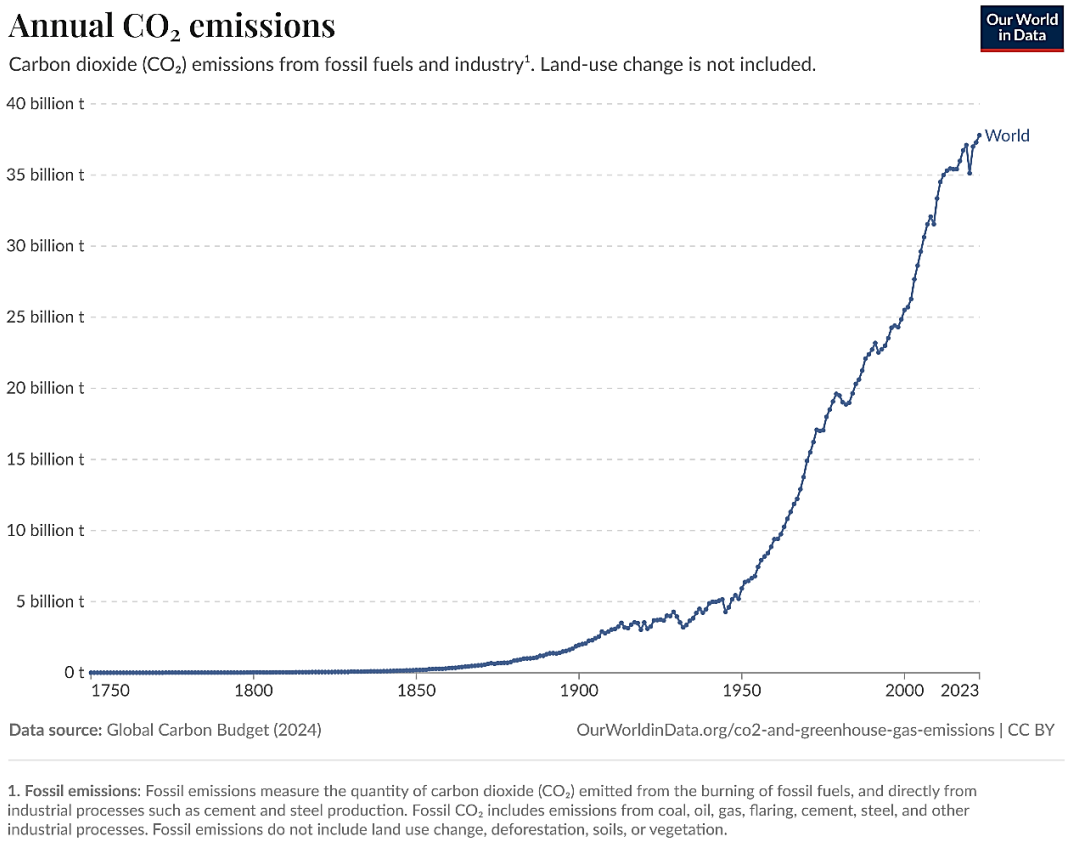

Figure 1.2 Emissions of carbon dioxide (CO_2) from industry and fossil fuels [2]

As mentioned above, AHSSs aim to achieve a higher strength-to-density ratio by improving mechanical properties. From another perspective, higher strength-to-density ratio values can also be obtained by reducing the density of steel while maintaining good mechanical properties. To produce low-density steels, alloying elements like Al and Si are used. The alloying elements mentioned are usually added to the Fe–Mn–C system, and one of the most common is Fe-Mn-Al-C-Si. *Figure 1.3* shows that the density of lightweight steel containing high levels of Mn and Al can be 18% lower than that of conventional steel. This indicates that adding approximately 1 wt.% Al will decrease the overall density by 1.3% [3].

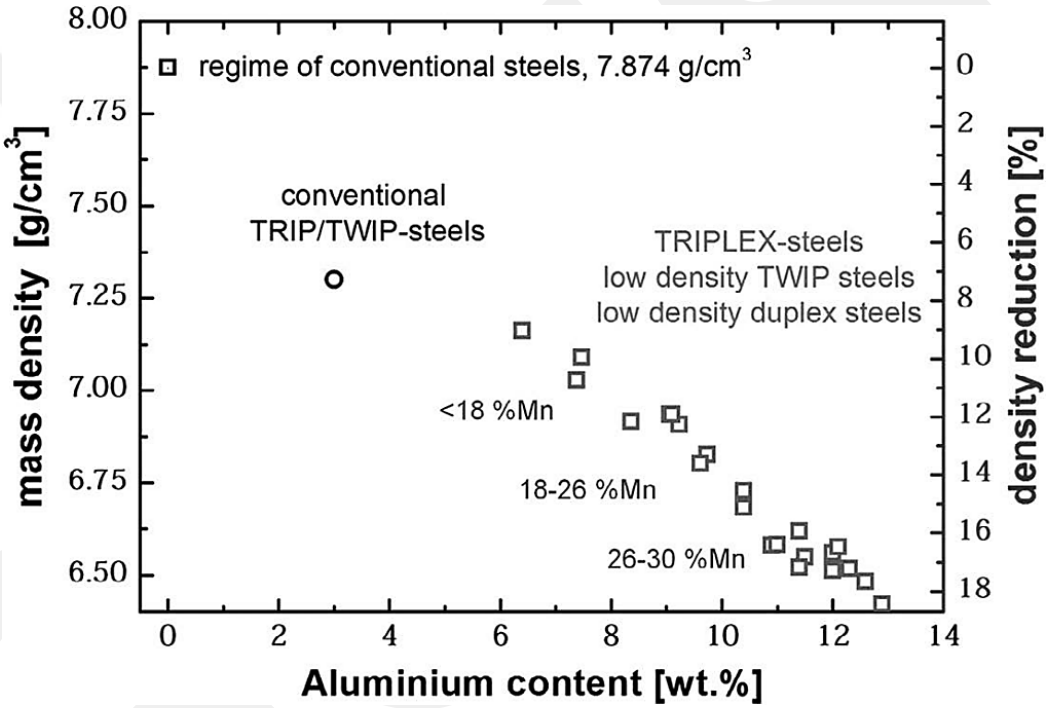

Figure 1.3 Density reduction depends on the Al wt% in the Fe–Mn–Al–C system [3]

Fe-Mn-Al-C and similar steels were originally intended as alternatives to stainless steels. However, recent studies have focused on developing lightweight, crash-resistant structures for car bodies and structural components for use in the cryogenic industry, thanks to their low density [4]. Research and development activities for these steels can lead to more sustainable products by contributing to the creation of environmentally friendly, lightweight, and long-lasting items.

1.2. Fe-Mn-Al-C-Si System

Lightweight steels, particularly the Fe-Mn-Al-C system, have been popular since the 1950s and have been extensively studied by academia, industry, and research institutions. One of the primary reasons for their continued popularity is their low density, which ranges from 6.5 to 7.0 g/cm³ depending on the chemical composition [3]. Additionally, these steels exhibit high mechanical properties both in room and cryogenic environments, making them attractive for a wide range of applications. Ongoing research focuses on developing various compositions of Fe-Mn-Al-C alloys for use in several industries, including aviation and space, defense, transportation, automobile chassis, and applications requiring oxidation and corrosion resistance [5]. According to *Scopus* data given in *Figure 1.4*, there has been a dramatic increase in interest and research in these types of steels, especially after the 2000s. The graph indicates a rising interest in this type of steel over recent years, along with ongoing research. This trend suggests that lightweight steel compositions suitable for industrial use are likely to be adopted across various sectors in the near future.

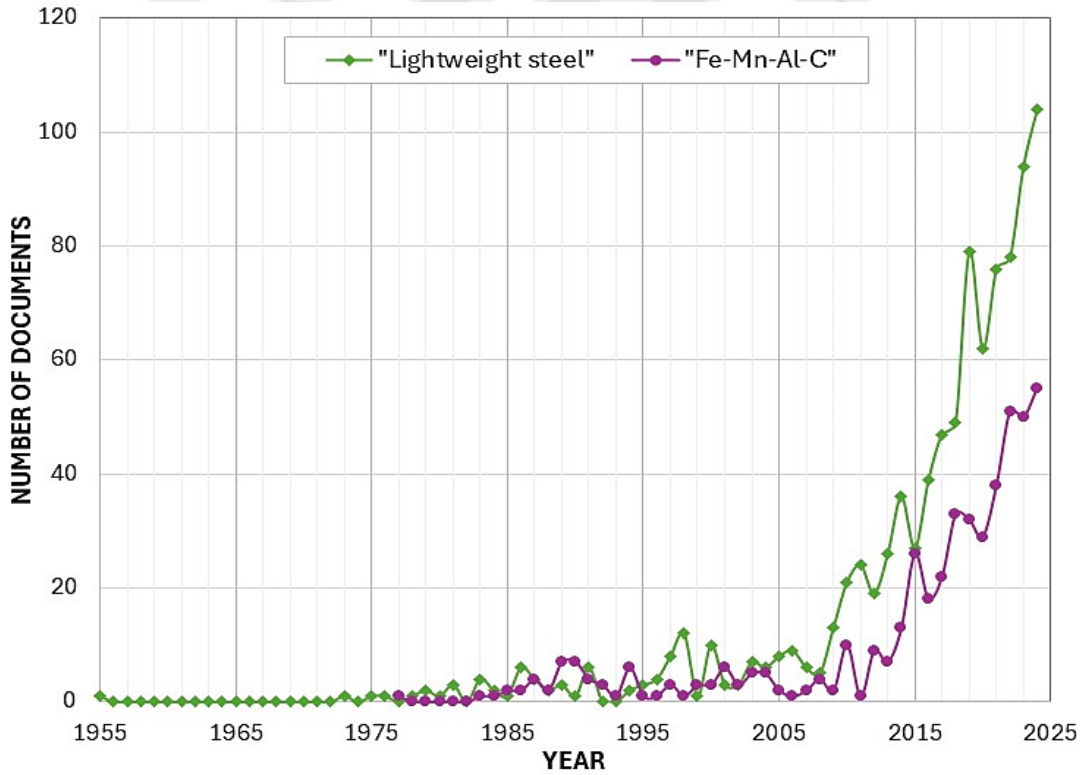

Figure 1.4 Number of documents published annually in Scopus since 1950 on the topics of "Fe–Mn–Al–C" and "Lightweight steel" [6]

The historical development of lightweight steel begins with high manganese steel. In 1938, *Sir Robert Hadfield* published an article discussing an alloy steel that contained 11 to 14 wt.% manganese and approximately 1.25 wt.% carbon. This alloy was first discovered in 1882 and is still referred to today as "Hadfield Steel", in honour of his contributions to the field [7]. In 1943, *Reginald S. Dean and Clarence T. Anderson* were granted a patent for compositions that exhibit high corrosion resistance and good ductility. These compositions contain between 3% and 12% aluminum, 45% to 75% iron, at least 20% manganese (and in some cases, up to 50%), and 1% to 2% chromium and/or silicon [8]. In 1958, *Ham and Cairns* studied the mechanical properties of Fe-34Mn-10Al-0.76C (in wt. %) and found that it had Ultimate Tensile Strength (UTS) of 750 MPa and an %EL of 70 [9]. The research conducted by *Kayak* in 1969 focused on determining the optimal composition of the Fe-Mn-Al alloy system and examining the effects of heat treatment on mechanical properties and this work is crucial for understanding the aging mechanisms in these steels [10]. In 1981, *Banerji* researched Fe-Mn-Al steels as an alternative to stainless steels. In his study, chromium was substituted with aluminum, while nickel and carbon were replaced with manganese [11]. In 1985, *Benz and Leavenworth, Jr*. conducted a study on alternatives to austenitic stainless steels, focusing on compositions of Fe-34.5Mn-10Al-0.76C and Fe-30Mn-8Al-1.5Si-1.0C [12]. A study conducted in 1985 by *Kim, Park, and Han* examined the mechanical properties of two compositions with low amounts of niobium and vanadium, specifically for the chemical composition Fe-30Mn-5Al-0.3C [13]. In the Material Handbook published in 1989, it was reported that the tensile strength of steel with a chemical composition of 30% manganese, 9% aluminum, 1% carbon, and 1% silicon—*developed by Ford Motor Company*—was 2068 MPa after rolling and heat treatment [14]. In 1993, *Chao and Liu* investigated the precipitates formed by aging Fe-7.8Al-29.5Mn-1.5Si-1.05C at various times between 550°C and 850°C, and they also examined the effect of silicon addition on the composition [15]. In 2006, *Frommeyer and Bruex* studied Fe-Mn-Al-C (18-28% Mn, 9-12% Al, 0.7-1.2% C) to investigate the microstructure, mechanical properties, and deformation mechanisms of high-strength, lightweight TRIPLEX steels for potential automotive and structural applications [16].

Due to its historical development and recent studies, the features of lightweight steels and their potential for further development remain subjects of ongoing research. Obtaining various phases, such as ferritic, austenitic, ferrite-based duplex, and austenite-based duplex, according to their chemical compositions, is essential for developing lightweight steels with desirable properties [3]. The key feature of these lightweight steels lies in their ability to attain the desired mechanical properties through solutionizing and aging treatments, depending on their specific chemical compositions [17].

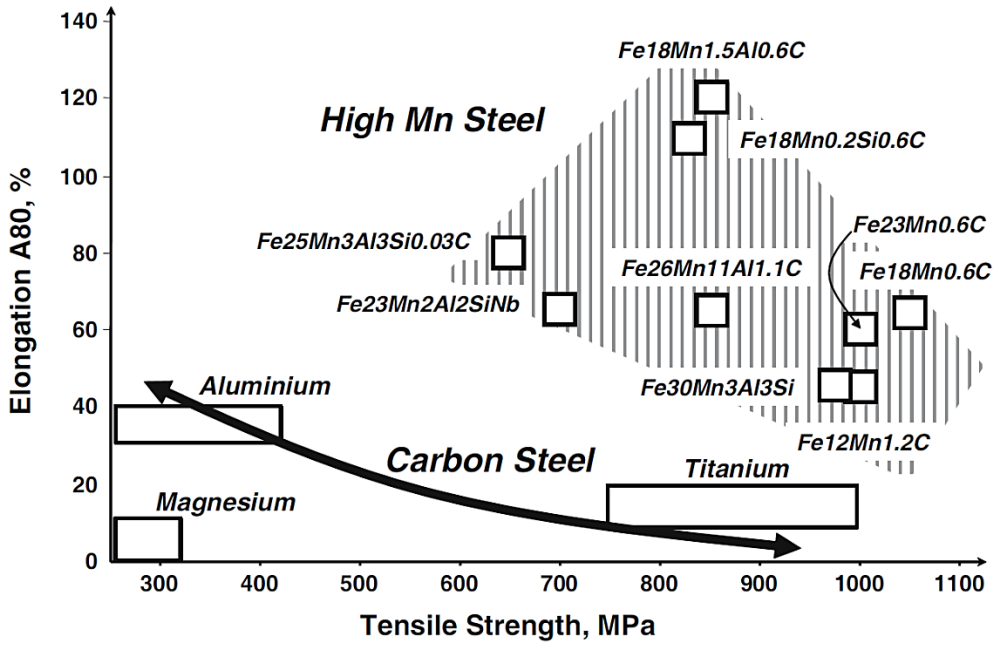

Figure 1.5 The mechanical properties of lightweight steels with various chemical compositions [18]

Today, researchers from many different countries continue to work on lightweight steels, especially the Fe-Mn-Al-C system and have made many important publications. These studies continue to work in many different areas such as understanding the heat treatment properties of steels in relevant compositions, observing the effects of precipitates formed by aging on mechanical and physical properties, and phase diagrams, thus contributing to the emergence of lightweight steel that can be used industrially in the not-too-distant future.

1.3. Scope and Aim of the Current Study

The current study aims to characterize the as-cast Fe-Mn-Al-C-Si experimental lightweight steel and explore optimal parameters for enhancing its mechanical and tribological properties through solutionizing and aging treatments.

Specifically, the study intends to conduct both mechanical and microstructural characterization of the as-cast Fe-Mn-Al-C-Si lightweight steel. The selected chemical composition was aimed at obtaining an austenitic microstructure. First, the as-cast samples were characterized. Then, a thermodynamic analysis of the cast composition was conducted to determine the phase equilibria of the possible phases within the temperature range of 25-1400°C. The results of the thermodynamic analysis and literature data were used to determine the conditions of solutionizing and aging treatments to be applied to disk samples. Characterization results of these samples, including microstructural examination, hardness measurements, XRD analysis, and SEM observations, were used to determine the optimum thermal processing conditions of the samples. Overall, the results are discussed in the context of developing sustainable and more competitive products in subsequent processes, and suggestions are made.

1.4. Outline of the Thesis

This thesis consists of 6 main chapters. The first chapter discusses the development of light steels, their areas of use, and their potential for development. The second chapter explains the types of lightweight steels, the effects of main alloying elements, phase diagrams, heat treatment conditions, and mechanical properties. The third chapter includes the details of experimental work done in this thesis, such as testing, analysis and heat treatment. The fourth chapter includes the results obtained from these tests and experiments. The fifth chapter discusses the results obtained from these tests and their comparison with literature. Finally, the sixth chapter includes conclusions and suggestions for future studies.

CHAPTER 2

THEORY & LITERATURE SURVEY

2.1. Types of Lightweight Steels

Lightweight steels may have different matrix phase structures, depending on their chemical composition (*Table 2.1*).

Table 2.1 Compositional characteristics of low-density Fe–Mn–Al–C steels [3]

TYPE	*Ferritic*	*Ferrite Based Duplex*	*Austenitic*	*Austenite Based Duplex*
COMPOSITION (wt%)	Mn: < 5 Al: 5 - 9 C <0.1	Mn: 3 – 10 Al: 3 – 9 C < 0.4	Mn: 15 – 30 Al: 2 – 12 C: 0.5 – 2.0	Mn: 10 – 25 Al: 5 – 12 C: 0.6 - 1

Ferritic Fe–Mn–Al–C steels have low Mn contents (<5 wt%), intermediate Al contents (5–9 wt%), and low C contents (<0.1 wt%). Si, Nb, Ti, V, or Ta are occasionally alloyed with these metals for carbide precipitation and grain refining [3]. **Ferrite-Based Duplex,** and triplex Fe-Mn-Al-C steels contain amounts of Mn contents (2–12 wt%) and C contents (0.05–0.5 wt%). Their microstructures consist of a combination of austenite and delta/alpha ferrite in duplex steels, while triplex steels include austenite, delta/alpha ferrite, and martensite, with the ferrite component exceeding 50% [5]. **Austenitic Lightweight Steels**, higher Mn contents (12–30 wt%), Al contents (>12 wt%), and C contents (0.6–2.0 wt%) are seen in austenitic low-density steels. At high temperatures, these alloys can have a fully equiaxed-austenitic microstructure, and upon rapid cooling, the austenite becomes metastable [19]. **Austenite-Based Duplex**, $\gamma + \delta/\alpha$ ferrite or $\gamma + \alpha$ ferrite are characteristics of austenite-based Fe-Mn-Al-C steels with a higher Mn content, usually between 8 and 32 wt%, Al content up to 12 wt%, and C between 0.3 and 1.2%. In contrast to ferrite-duplex steels, austenite makes up over 50% of austenite-based duplex steels, and because of the significant alloying elements, austenite has a high degree of stability [5].

2.1.1. Effect of Alloying Elements

In lightweight steels, the main alloying elements are Mn, Al, and C. In addition, elements such as Si and P also have important effects on phase constitution and precipitation. According to *Table 2.2*, if an austenitic steel is desired, the Mn and C content should be high [20]. However, if it contains high amounts of Mn, undesirable β-Mn formation can be observed in the microstructure, this structure is brittle and adversely affects the mechanical properties. Carbon is very important for stabilizing austenitic, another important aspect is that it must be present in high amounts in austenitic Fe-Mn-Al-C steels as it participates in the formation of κ-carbide with aging. For the formation of κ-carbide, the aluminum content must be more than 5% and the carbon content must be more than 0.3 [21]. The solid solution of C into austenite proposes being below 1.2 wt% in Fe–Mn–C–Al low-density steel to prevent crack formation of secondary phase and/or carbides during the plastic deformation stage, even if the inclusion of C reduces density by around four times when compared to the Al element [20]. Since aluminum, like carbon, is involved in the formation of κ-carbide, it must be present in high amounts in the structure, but since the presence of high amounts of aluminum will also support the formation of ferrite if an austenitic structure is desired, the amount of aluminum should be limited accordingly. If a high aluminum content of austenitic steel is desired, adding 1% carbon suppresses the ferrite base even at 10% aluminum content. Aluminum is also the element that causes Fe-Mn-Al-C steels to be called "*lightweight steel*", 1 wt.% Al will decrease the overall density by 1.3% [3].

Table 2.2 Summary of the alloy elements effects in the Fe–Mn–Al–C system [22]

ELEMENT	MAIN EFFECT
Mn	Stabilize the γ phase. It can promote the β-Mn phase.
C	Stabilize the γ phase.
Al	Stabilize the α phase. Reduce the density of the steel.
Si	Increase the kinetics of zone formation before κ-carbide precipitation. Prevent the β-Mn phase reaction.
High-C *High-Al*	Stabilizes the κ-carbide.

As shown in *Figure 2.1* in the study by *Ishida et al.*, in the diagrams drawn for Fe-20Mn-9Al-XC and Fe-30Mn-9Al-XC, austenite can be obtained at lower carbon levels as the manganese amount increases from 20% to 30%, and the austenitic region expands [23].

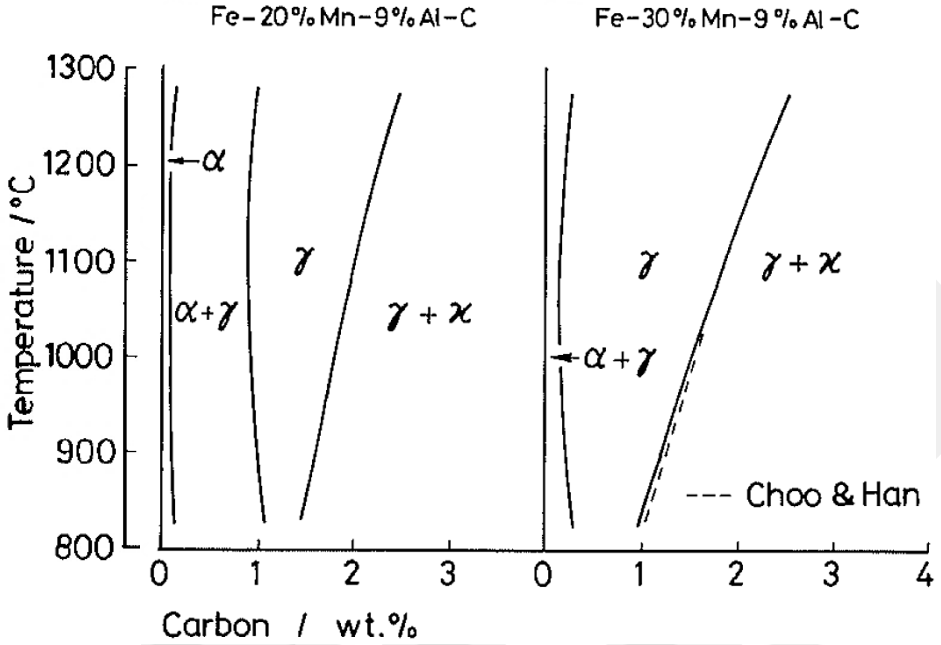

Figure 2.1 Diagrams showing vertical sections of Fe-(20-30)Mn-9Al-XC alloys [23]

As mentioned above, manganese is important to stabilize the austenite phase, but β-Mn formation is observed in a Fe-Mn-Al-C steel with a high amount of manganese content. β-Mn was first discovered by Schmatz in 1959 [24]. Si addition lowers the melting temperature and inhibits β-Mn formation [25]. The decrease in melting temperature also reduces the activation energy required for diffusion, resulting in larger grain size [26]. However, the most important feature of silicon addition is that it prevents β-Mn formation. In the study conducted by *Acselrad et al.*, they examined the phases formed by aging steel with the chemical composition Fe-28Mn-8.5Al-1C-1.25Si between 300°C and 700°C. It was observed that β-Mn, which is generally formed in long aging periods at 500-650°C, did not form β-Mn even after 300 hours at 650°C after silicon addition in this study. The reason for this is that silicon shifts the manganese from the matrix towards κ-carbide and there is not enough manganese left in the matrix for the formation of β-Mn [27]. A similar study was carried out by

Bartlett et al. for the chemical composition of Fe-30Mn-9Al-1Si-0.9C-0.5Mo, and no β-Mn formation was observed in samples with silicon addition after aging at 530°C for 140 hours [28]. In the graph shown in *Figure 2.2*, the increase in silicon composition at 1100°C causes an increase in aluminum and carbon activity, which in turn causes the formation of κ-carbide to accelerate, resulting in the depletion of manganese in the matrix. The addition of silicon prevents the formation of brittle and undesirable β-Mn in the matrix and promotes the formation of κ-carbide, which positively affects the mechanical properties.

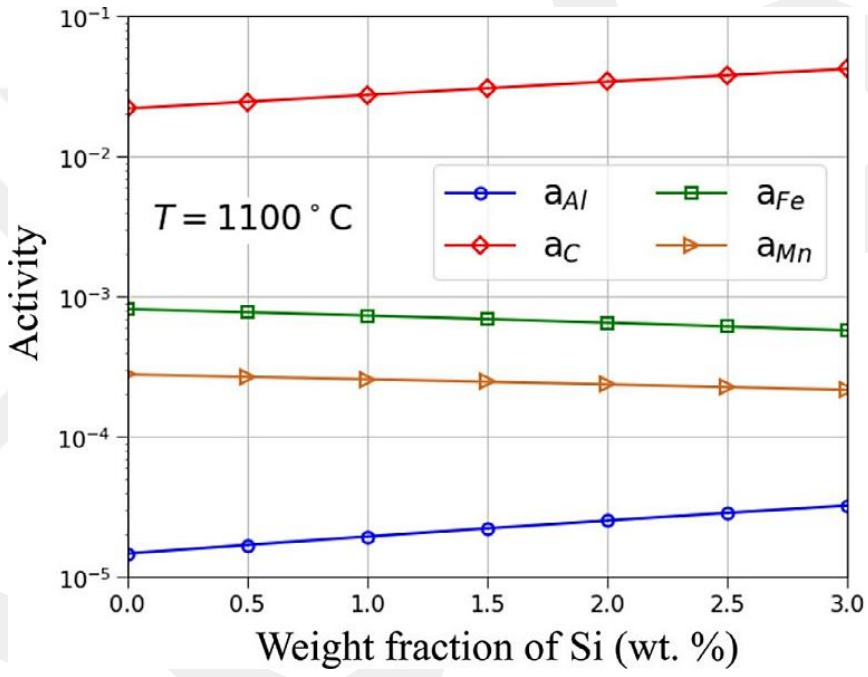

Figure 2.2 The activities of some elements (Fe, Mn, Al, and C) in austenite at 1100°C as a function of Si content [26]

Phosphorus causes higher hardness values to be obtained during aging. One of the main reasons is that the activation energy for the precipitation of κ-carbide reduces with increasing phosphorus levels. Additionally, microstructural evidence indicates that phosphorus increases the size and quantity of grain boundary κ-carbides and segregates to interdendritic zones [28].

2.2. Phase Equilibrium in Fe-Mn-Al-C System

In Fe-Mn-Al-C systems, various phases and precipitates can be obtained depending on the chemical composition. If these phases and precipitates are listed, they can be categorized as Austenite (γ), Ferrite (α, δ), B_2, $D0_3$, κ-Carbide.

According to *Figure 2.3*, for the relevant chemical composition Fe-30Mn-8Al-1.2C (wt%), a completely FCC (austenite) phase is observed at 1000°C in the phase distribution graph prepared using the *PrecHiMn-4* database. In addition, with the increase in carbon content, the FCC (austenite) phase continued as a single phase even at higher aluminum composition at the same temperature (1000°C). Additionally, BCC (Ferrite), Cementite, κ-Carbide, and intermetallic phases can be observed in different carbon and aluminum compositions at 1000°C. In studies using the *PrecHiMn-4* database for 600°C, there is no single-phase FCC (austenite) phase. In addition to the phases found at 1000°C, β-Mn, and different intermetallic phases were observed. κ-carbides are produced at 600°C when Al > 5 wt% and C > 1 wt% weight percent. Cementite and $M_{23}C_6$-type carbides can develop in place of κ-carbides at low Al contents (Al<6 wt%).

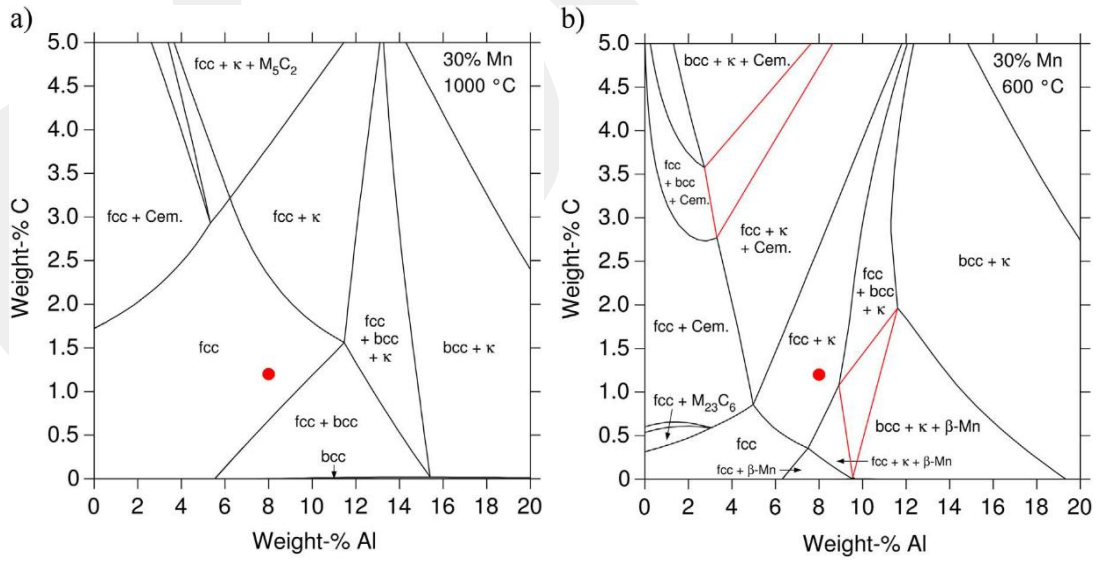

Figure 2.3 The Fe–Mn–Al–C system calculated using the PrecHiMn-4 database for 30 wt.% Mn at a) 1000°C and b) 600°C. The red dot represents an alloy with 30% Mn, 8% Al, and 1.2 wt% C [29]

Ishida et al. investigated the phases formed after heat treatment between 900°C and 1200°C for 14-210 hours for the chemical composition of Fe-30Mn-9Al-XC (*Figure 2.4*) [23]. The findings obtained from the study indicate that single-phase FCC (austenite) can be obtained at the relevant temperatures. The austenite phase region expands with increasing temperature. In addition, high carbon and aluminum values are needed to obtain κ-carbide at high temperatures.

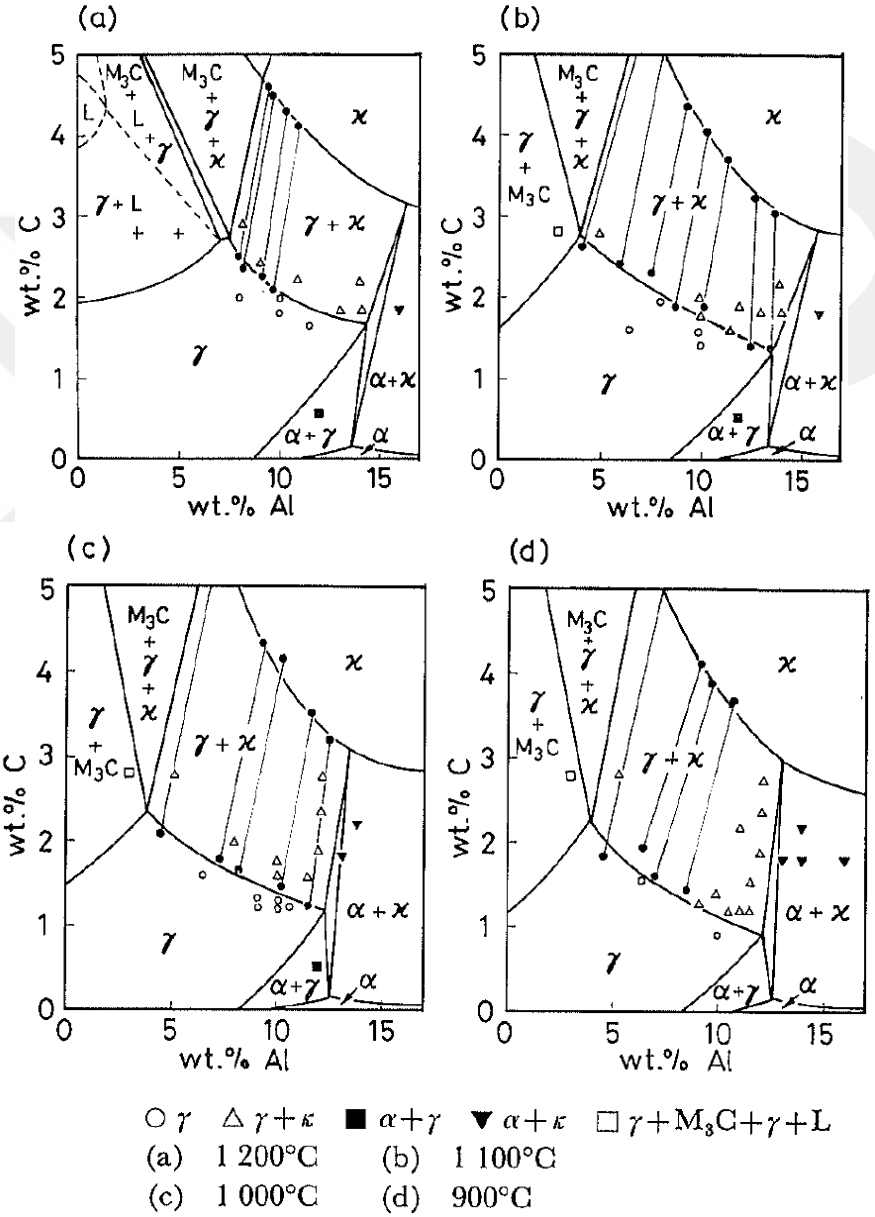

Figure 2.4 Fe-30Mn-Al-C alloys isothermal section diagrams for (a) 1200°C, (b) 1100°C, (c) 1000°C, and (d) 900°C [23]

In the study conducted by *Li et al.* for Fe-30Mn-XAl-1C wt%, the phase distribution at high temperatures is shown in the diagram below (*Figure 2.5*), depending on the aluminum content [30]. With the increase in the aluminum content, the single-phase austenite area shifted towards higher temperatures. Depending on the aluminum composition, austenite and intergranular κ*-Carbide formation is observed between 950-1050°C. With the decrease in temperature, austenite and intergranular/intragranular κ-carbide are observed.

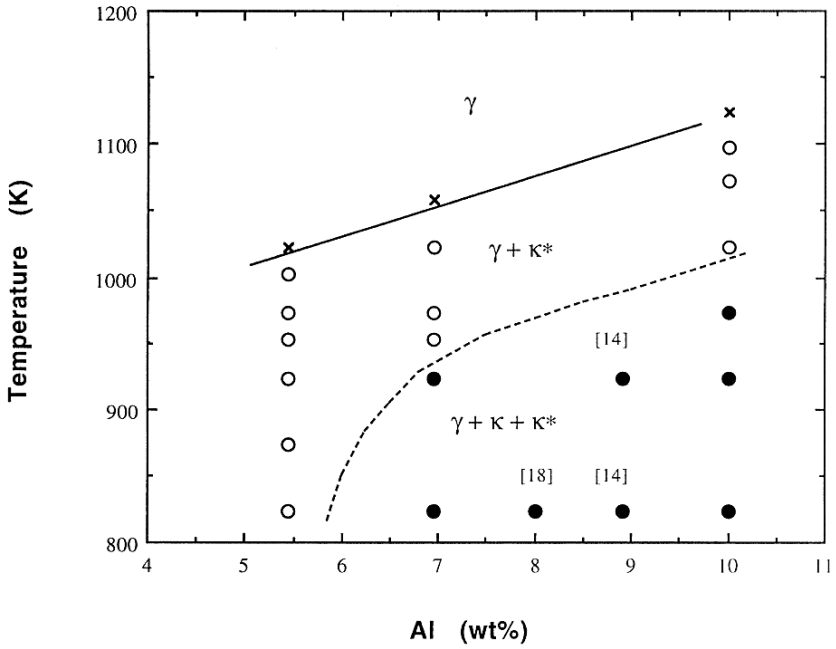

Figure 2.5 Effect of Al percentage on Fe-30Mn-Al-1C alloy κ phase solvus [30].

As seen in the studies, different phases and precipitates are obtained at different compositions and temperatures. The desired phases and precipitates can be obtained by adjusting the necessary chemical composition, considering the intended use of the steel to be produced. For example, if an austenitic steel is desired, high manganese and carbon are required. Phases such as κ-carbide, β-Mn, B_2, $D0_3$ that may form in these steels directly affect the mechanical properties. While precipitates that form especially at the grain boundaries negatively affect the mechanical properties, the contribution of precipitates that are homogeneously distributed within the grain can be positive. For this reason, the precipitates that may form should be examined in further detail: κ-carbide, B_2, $D0_3$, and β-Mn in the following pages.

- **κ-carbide**

The most well-known precipitate of the Fe-Mn-Al-C system, κ-carbide, is actually an $E2_1$ structure (Strukturbericht Designation) based on the $L1_2$ structure, and $(Fe,Mn)_3AlC$ formula (*Figure 2.6*) [31]. It has aluminum atoms at the corners, carbon atoms in the center, and Fe or Mn on the surfaces. κ-carbide is named according to the region where it is formed. If it is on the γ/γ grain boundary, it is called intergranular **κ*-carbide**. κ*-carbide creates stress-intensive regions at the grain boundaries under force, adversely affecting mechanical properties, especially elongation. If it is formed in γ matrix, it is called intragranular **κ'-carbide**, also intragranular κ'-carbide is desired for better mechanical properties [32]. The austenite matrix and κ-carbide have a cube-on-cube orientation relationship: $<100>_K//<100>_\gamma$ and $\{001\}_K//\{001\}_\gamma$ [25] .

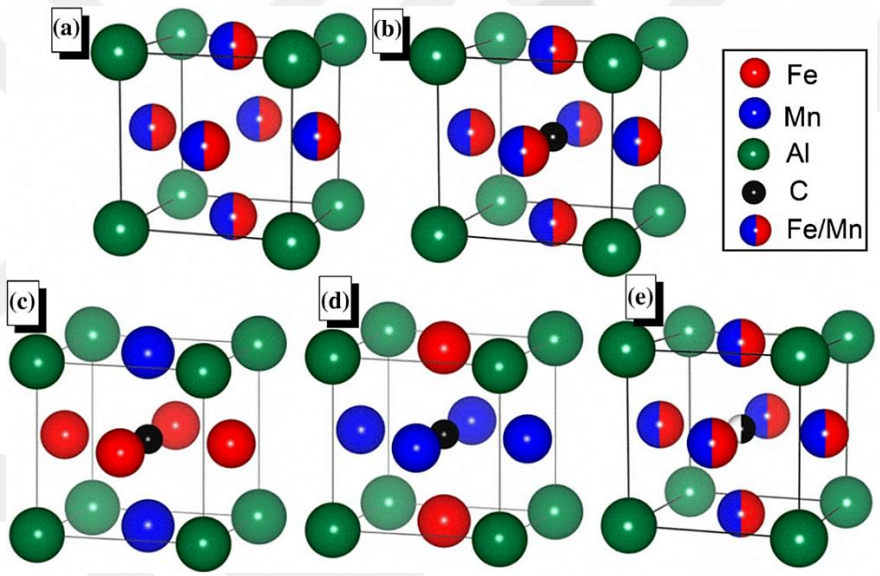

Figure 2.6 Cubic structures of κ-carbide (a) $L1_2$ (b) $L'1_2$ (c) Fe_2MnAlC (d) Mn_2FeAlC (e) $(Fe,Mn)_3AlC$ [22]

In the study conducted by *Bentley*, it was stated that after 1000°C solution heat treatment+quench and aging at 550°C for Fe-30Mn-9Al-1C-1Si, κ-carbide formation was not by nucleation grow mechanism but by spinodal decomposition and that κ-carbide was already formed in the matrix after quench, Fe-Al-C alloys can lead to rapid ordering during quenching [33]. *Chu et al.* performed oil quench after solution at 1050°C for Fe-29.5Mn-10.0Al-1.03C-0.86Si-0.010P-0.0195S (wt%) and studied the related mechanisms by aging between 550°C and 700°C temperatures for different

times. Like *Bentley*, it was observed that κ-carbide was present in the microstructure after quenching. In addition, as shown in *Figure 2.7*, the κ-carbide shows coarsening as the temperature increases in the aging process for similar times. This clearly shows that there is a positive correlation between the κ-carbide particle size and temperature. It also shows that the long-range diffusion of Mn and Al atoms does not play a role in the coarsening of κ-carbide, whereas the diffusion of carbon atoms is necessary. [34]

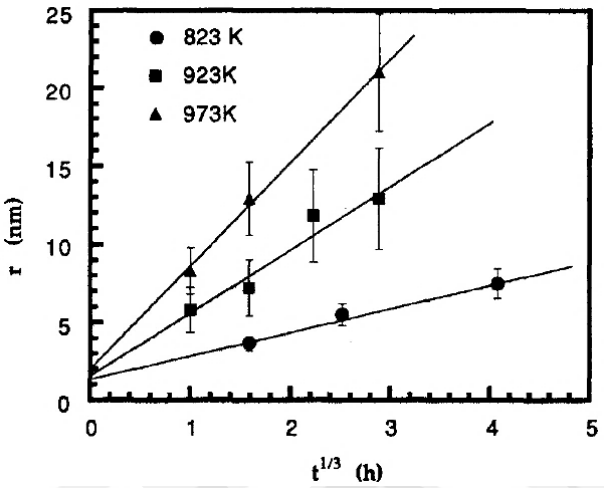

Figure 2.7 The κ-carbide particle coarsening kinetics

In their study on the chemical composition of Fe-7.8Al-29.5Mn-1.5Si-1.05C, *Chao and Liu* found that after heating at 1050°C for 2 hours, the as-quenched microstructure is an austenite phase containing fine κ'-carbides [15]. In the study conducted by *Cheng et al.*, it was found that the $L1_2$ phase formed by spinodal decomposition after a solution and quenching was transformed into κ-carbide through an ordering reaction during heat treatments carried out at 725°C:

$$\gamma \rightarrow \gamma' + \boldsymbol{\gamma''} \rightarrow \gamma' + \mathbf{L1_2} \rightarrow \gamma' + \boldsymbol{\kappa}\textbf{-carbide}$$ [35].

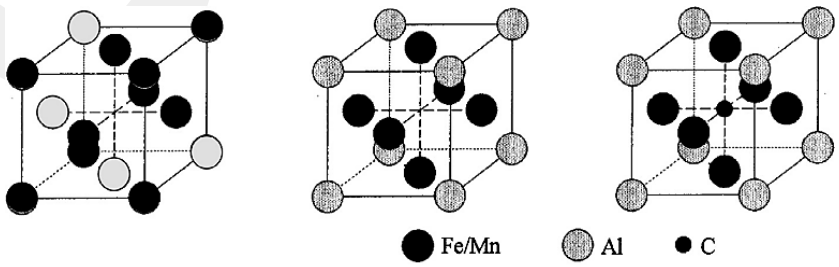

Figure 2.8 Cubic structure of (a) disordered γ, (b) ordered γ ($L1_2$) and (c) κ-carbide structure in FCC alloys [19]

In recent studies, Fe-30.5Mn-8Al-1.0C (wt.%) 1050°C solution heat treatment and air cooling followed by aging at 500°C, 550°C, 600°C, and 650°C and different times were tested and it was found that κ-carbide formation occurs with spinodal decomposition at certain temperatures (500-550°C) and with the increase in temperature (600-650°C) κ-carbide formation gradually passes from spinodal decomposition to nucleation-growth mechanism (*Figure 2.9*). The reason for this is that with increasing temperature, the rate of Al and C diffusion increases, causing the formation of Al-rich and C-rich regions at the grain boundary and the formation of κ-carbide precipitates. At the same time, this increasing temperature and increasing aging times also explain the mechanism of κ*-carbide precipitates formed at grain boundaries, these precipitates to form at grain boundaries adversely affect mechanical properties. [36]

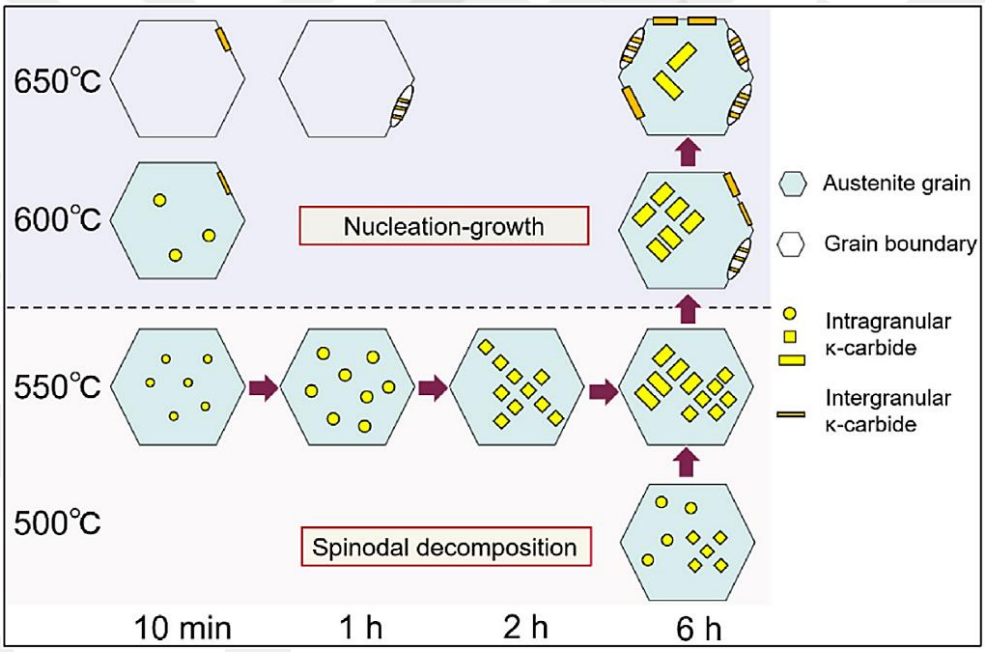

Figure 2.9 Illustration showing the evolution of κ-carbide particle precipitation over time [36]

In addition, the aging time and temperature directly affect the morphology of the κ-carbide particles that will form. As shown in *Figure 2.9*, κ-carbide particles can be spherical, cubical and rectangular. The κ-carbide morphology is related to the interfacial energy and elastic mismatch between the austenite and κ-carbide particles. The amount of elastic misfit is reduced at low aging temperatures or short aging times

because the κ-carbide percentage is low; in these conditions, the interfacial energy contribution is dominant, and the κ-carbide particle shape is spherical. The shape changed into a rectangular and cubical shape as the percentage of κ -carbide increased. The reason for this is that the constant aging decreased the austenite's lattice parameter, which increased the elastic misfit between the κ-carbide particles and the austenite matrix [36]. κ-carbide can also be found in as-cast microstructures as seen in *Figure 2.10*.

Figure 2.10 SEM microstructural image of as-cast 1.38C, 31.6Mn, 8.8Al, 0.5Si (wt%) [32]

In the study conducted by Jiménez and Frommeyer, Equation (2.1) was developed to calculate the κ-carbide lattice parameter depending on the carbon ratio. The κ-carbide lattice parameter increases with the increase in the carbon ratio [37] :

$$a_{K-Carbide} = 0.37605 + 0.00295\, at.\%C \quad (2.1)$$

As is known, Fe and Mn atoms can be found in the same place in the κ-carbide structure. This causes a change in the κ-carbide lattice parameter according to the ratio of Fe and Mn atoms in κ-carbide. While the Fe atomic radius is 126 pm, the Mn atomic radius is 132 pm, which means that there is a larger lattice parameter for κ-carbide with a high Mn ratio, also κ-carbide lattice parameters are given according to the Fe and Mn ratio in *Table 2.3*. [38]. In addition, the addition of silicon will shift the Mn in the matrix towards κ-carbide, causing larger lattice parameter and positively affecting the hardness and mechanical properties [28]

Table 2.3 Relevant references providing the κ-carbide lattice parameters [38]

κ-carbide	a (nm)
Fe_3AlC	0.378
	0.372 – 0.378
	0.3783 – 0.379
	0.376
Fe_2MnAlC	0.378
$FeMn_2AlC$	0.380
Mn_3AlC	0.381
	0.3875

- **B_2 and $D0_3$**

In addition to κ-carbide precipitates, α-precipitates may form depending on the heat treatment and chemical composition. The body-centered cubic (BCC) lattice has ordered forms for the AlFe (B_2) and $AlFe_3$ ($D0_3$) phases (*Figure 2.11*).

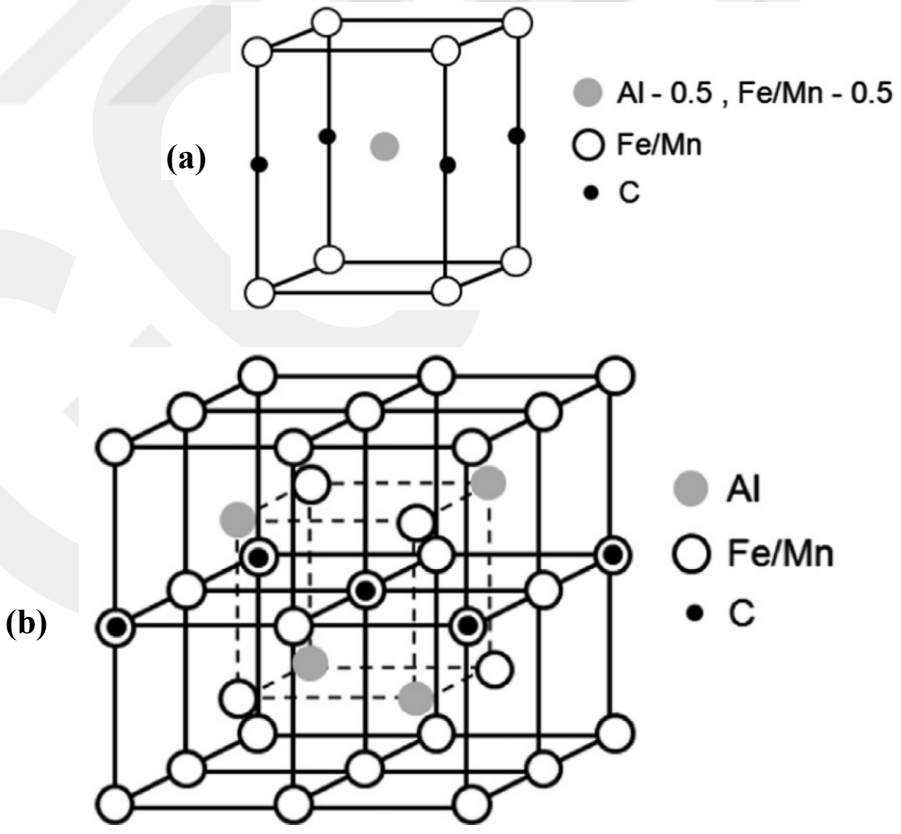

Figure 2.11 Cubic Structure of (a) B_2 and (b) $D0_3$ [39]

Lin, aged Fe-9%Al-30%Mn-XC-Si at 550°C for 48 hours to 313 days in the study and observed that κ-carbide transformed into B_2 + $D0_3$ structure as a result of long aging times. As seen in the XRD results in *Figure 2.12*, only the microstructure of the sample quenched after the solution was single-phase austenite in (a), while κ-carbide, as well as B_2 and $D0_3$ precipitates, were observed after 1 week of aging at 550°C in (b). [40]

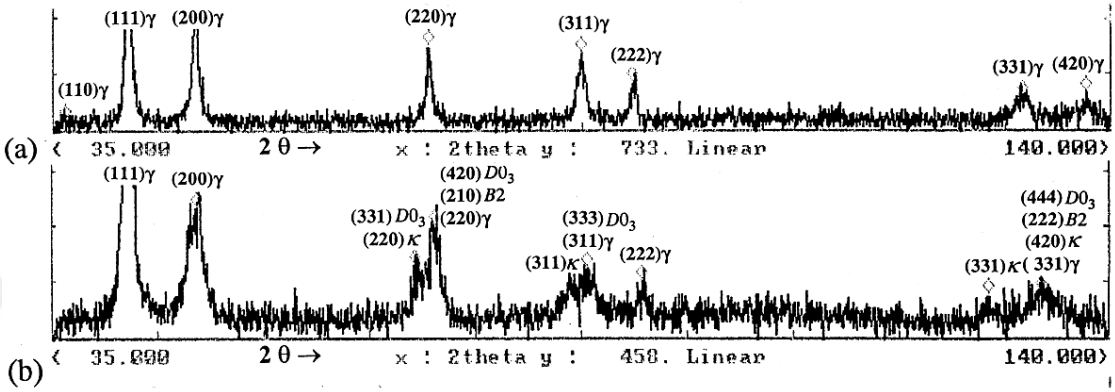

Figure 2.12 X-ray diffraction patterns at 550°C for different times after the alloy solid solution and after over-aging: (a) solution-treated at 1050°C for one hour and quenched in water (b) overaged for a week

Wu et al. observed that there were $D0_3$ particles inside the ferrite grains in an extremely fine structure after solution and quench for Fe-10.1A1-28.6Mn-0.46C (wt %) duplex steel (ferrite + austenite), and it was observed that these $D0_3$ precipitates became coarser as a result of long-term aging at 550°C [41]. In the study conducted by *Chao et al.*, aging was performed between 620°C and 900°C for Fe-9.8Al-28.6Mn-0.8Si-1.0C (wt%). On the austenite grain boundary, the γ → $D0_3$ + κ-carbide transition took place. Grain boundary precipitates were a combination of (B_2 + κ- carbide) or (γ + κ-carbide) phases when the aging temperature was raised to 800°C. Only B_2 (or α) precipitates were visible on the austenite grain boundary when the aging temperature was raised to 825°C [42]. In another study conducted for the chemical composition of Fe-7.8Al-29.5Mn-1.5Si-1.05C (wt%), it was observed that γ→ κ-carbide + $D0_3$ was formed as cellular precipitation on the γ/γ grain boundary and twin boundary as a result of long-term aging at 550°C to 850°C. In the study, the lattice parameter of the $D0_3$ precipitate was stated as a_{D03}: 0.586 nm, showing that the κ-carbide and $D0_3$ particle's orientation connection is $[111]_K//[011]_{D03}$ and $(1\bar{1}0)_K//(11\bar{1})_{D03}$ [15].

- **β-Mn**

Manganese, the main alloying element in the Fe-Mn-Al-C alloy system, must be present in high concentration, especially for austenitic lightweight steel. However, the presence of high manganese content may cause undesirable β-Mn formation depending on the heat treatment condition. β-Mn adversely affects mechanical properties and elongation.

In the study conducted by *Lee et al.* for Fe-31.62Mn-8.74Al-0.89C-1.1Si, (wt%) heat treatment was applied at 1200°C for two hours and then hot-rolling was applied. Then, the sample was taken into the solution at 1050°C for two hours and the sing-phase austenite microstructure was obtained, and aging was done at 550°C for different times. As a result of aging at 550°C for 10,000 minutes, ferrite formation was observed on the γ/γ grain boundary, and then β-Mn formation was observed on the γ/α grain boundary (*Figure 2.13*). While ferrite has a lower Mn content than the other phases, the ferrite grain has comparatively higher quantities of Fe, Al, and Si. The greater amount of Mn that has migrated from the ferrite area during the ferrite nucleation process may make the ferrite/austenite phase borders more conducive to formation β-Mn. [43]

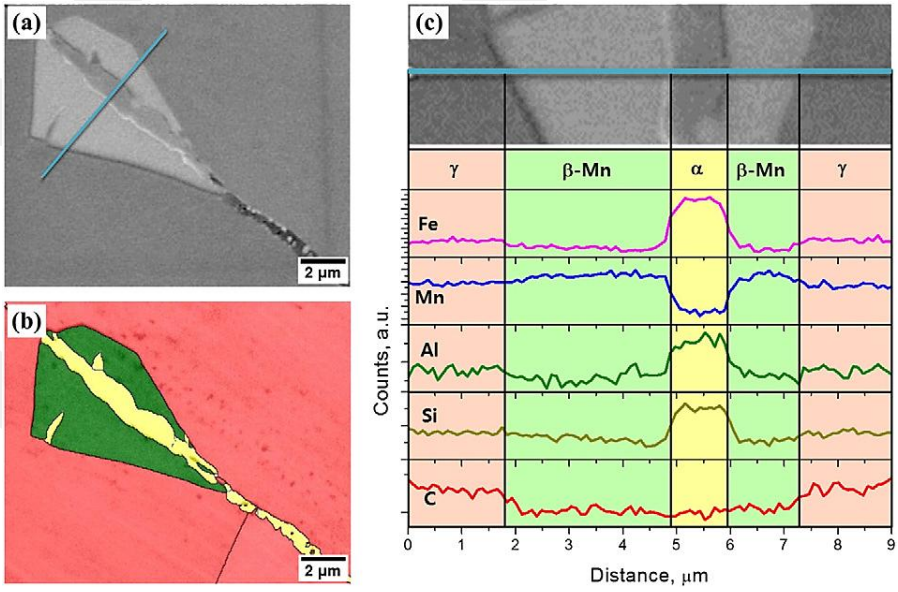

Figure 2.13 The 9Al-1Si aged for 10,000 minutes is shown in (a) the SEM micrograph and (b) the EBSD phase map (■ FCC; ■ BCC; ■ β-Mn). (c) The sky-blue line's EDS elemental profiles in (a)

In another study by *Lee et al.*, for the composition Fe-31.4Mn-11.4Al-0.89C (wt%), heat treatment was performed at 1200°C for 2 hours followed by hot rolling and solution at 1050°C for 2 hours then water quenching. In this study, unlike the previous page, there is no Si addition in the chemical composition. After solution, aging 300, 1000, and 10,000 minutes were performed at 550°C. As seen in the EBSD images in *Figure 2.14*, there is no β-Mn formation in the microstructure after ST, and β-Mn formation was observed after 300 minutes of aging at 550°C. In the previous page, β-Mn formation was observed at longer aging times, the reason for this is the Si addition, as explained in *"2.1.1 Effect of Alloying Element"*. In *Figure 2.14*, the β-Mn volume fraction (%) as a result of EDSB analysis increases with the increase of aging time. After 300 minutes of aging at 550°C, the β-Mn volume fraction was measured as 1.1%, after 1000 minutes it was measured as 43.3% and after 10,000 minutes it was measured as 56.2%. [44]

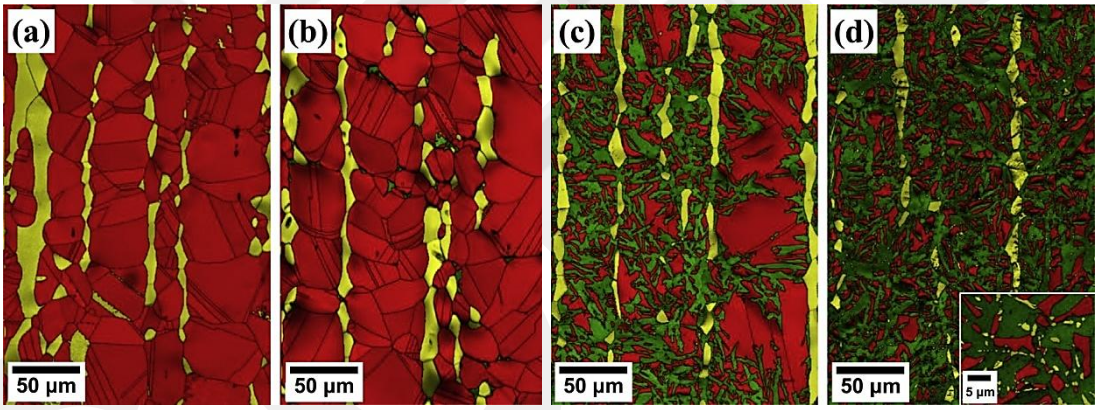

Figure 2.14 EBSD phase map of the following specimens: (a) ST; (b) A300; (c) A1000; and (d) A10000 (■ FCC; ■ BCC; ■ β-Mn)

2.2.1. Identification of the Phase Constitution

One of the fastest and most suitable analyses that can be used to determine the relevant phases and precipitates described above is X-Ray Diffraction (XRD). XRD analysis is performed to determine whether the targeted phase (austenite, ferrite) and the precipitates desired to be obtained by heat treatment have been formed.

XRD studies were carried out on samples with chemical composition of Fe-29.8Mn-7.65Al-1.11C-0.093Si-0.017S-0.0083N (wt%) by *Song et al.*[45]. The samples were first cold rolled, then subjected to homogenization heat treatment at 1200°C for 5 hours. Then, the samples were aging at 600°C for 15 minutes, 1, 3, 6, 9 hours. As shown in *Figure 2.15* a) only (200) austenite peak was observed after homogenization. In b), diffraction patterns taken after 15 and 60 minutes of aging at 600°C show that κ (200) peaks formed in short periods of time.

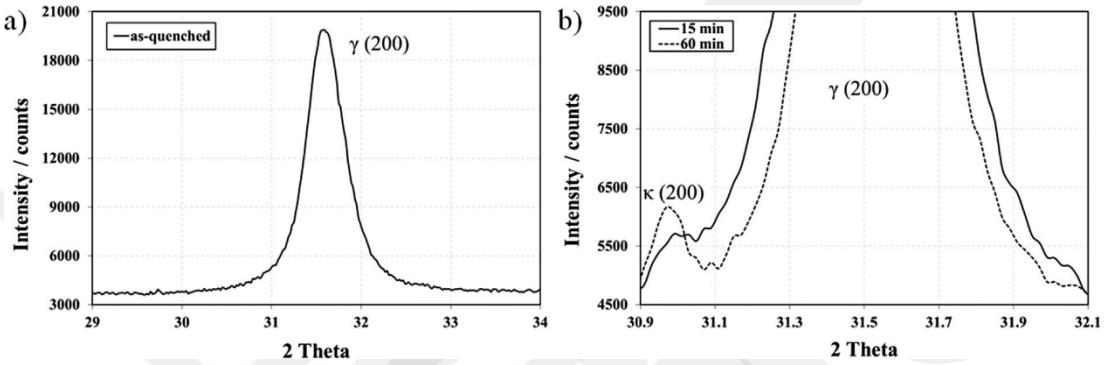

Figure 2.15 Fe-30Mn-8Al-1.2C alloy diffraction peaks of κ(200) and γ(200) in the as-quenched state a), and after being annealed at 600°C for 15 minutes and 1 hour b)

In *Figure 2.16*, diffraction images taken after aging at 600°C for different hours are given. As seen in the graph, the intensity of the (200) austenite peak decreases with an increase in aging time. At the same time, the austenite peaks shifted towards higher angles, which means that the austenite lattice parameter decreased.

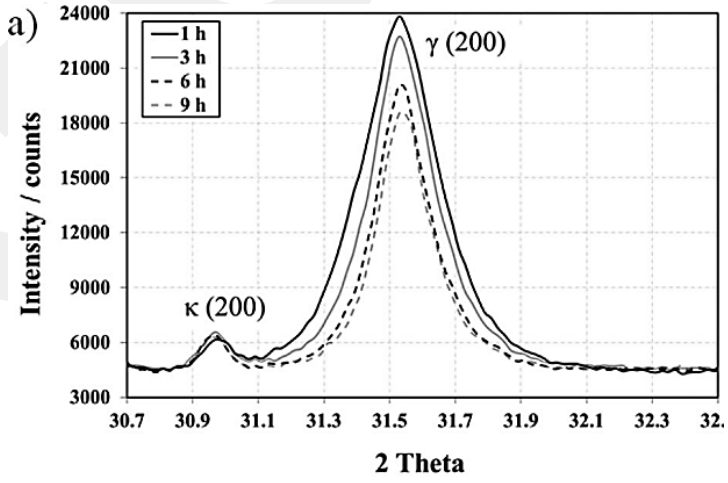

Figure 2.16 The Fe-30Mn-8Al-1.2C alloy κ(200) and γ(200) diffraction peaks at various times after annealing at 600°C

The study conducted by *Chen et al.* applied XRD (Cu-Kα) phase analysis to the samples subjected to aging process at different temperatures and times for 30.5Mn-8Al-1.0C (wt.%) composition by hot rolling and then 1 hour solution treatment at 1050°C and air cooling to room temperature. The results are as given in *Figure 2.17*. The study stated that XRD analysis is not suitable for aging processes carried out at very short and low temperatures because the precipitates formed at short and low temperatures will be very thin and will not create diffraction in XRD analysis. TEM analysis is more suitable for such samples. According to the analysis results given in *Figure 2.17*, no other structure was observed in the γ phase and κ-carbide precipitates in the samples. The broadening of the austenite peak depending on the increasing temperature in *Figure 2.17* (b) confirms the existence of κ-carbide precipitates. Nevertheless, the depletion of C in the surrounding austenite due to κ-carbide precipitation results in a reduced austenite lattice parameter and, thus, a shift of the broadening peak to a greater 2θ angle. [36]

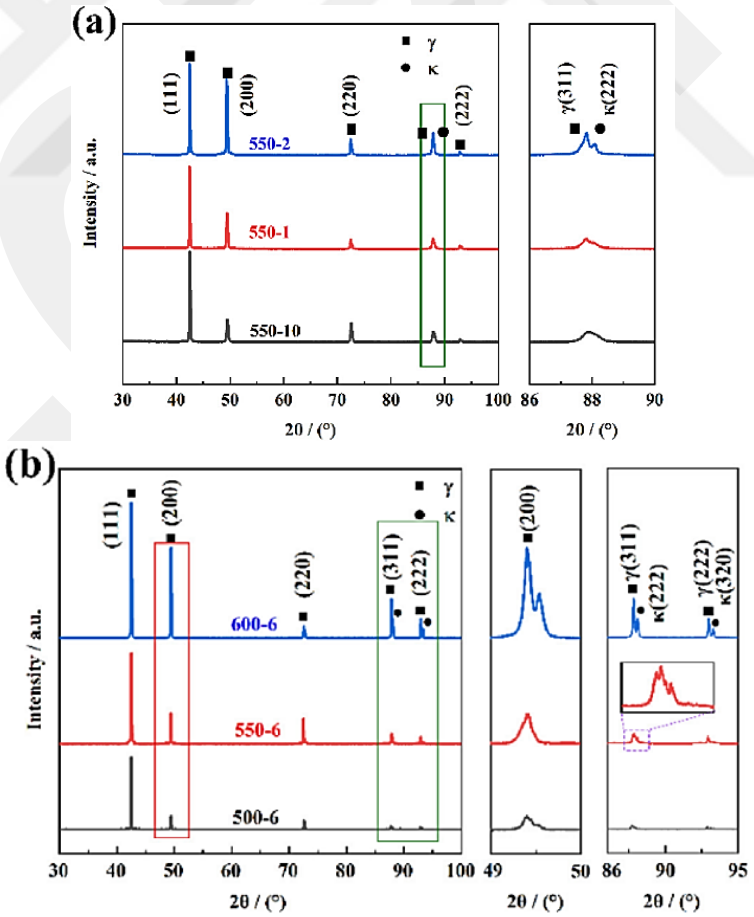

Figure 2.17 XRD of 30.5Mn-8Al-1.0C (wt.%) at different temperatures and times

Feng et al. carried out XRD (Cu-Kα) analysis of samples subjected to aging process at different temperatures and times after solution treatment at 1050°C for one and a half hours for the composition of 1.38C, 31.6Mn, 8.8Al, 0.5Si (wt%) and quenched in water and the results are as shown in *Figure 2.18*. Single-austenite phase was observed in the microstructure after solution heat treatment. *Figure 2.18* (a) illustrates the appearance of the κ-carbides and β-Mn diffraction peaks in A550 specimens. β-Mn formation and density increased with increasing aging time. In contrast to the A550 specimens, the A700-32 h specimen's XRD profile, which is shown in *Figure 2.18* (b), showed diffraction peaks of α. The A800 specimens' XRD profiles paralleled those of the A700 specimens, and *Figure 2.18* (c) shows that a large volume-fraction α also developed after 32 hours of aging. No identifiable β-Mn or α-ferrite peaks were seen in the XRD profile given in *Figure 2.18* (d) for A900 specimens, except the satellite peaks of κ-carbides. [32]

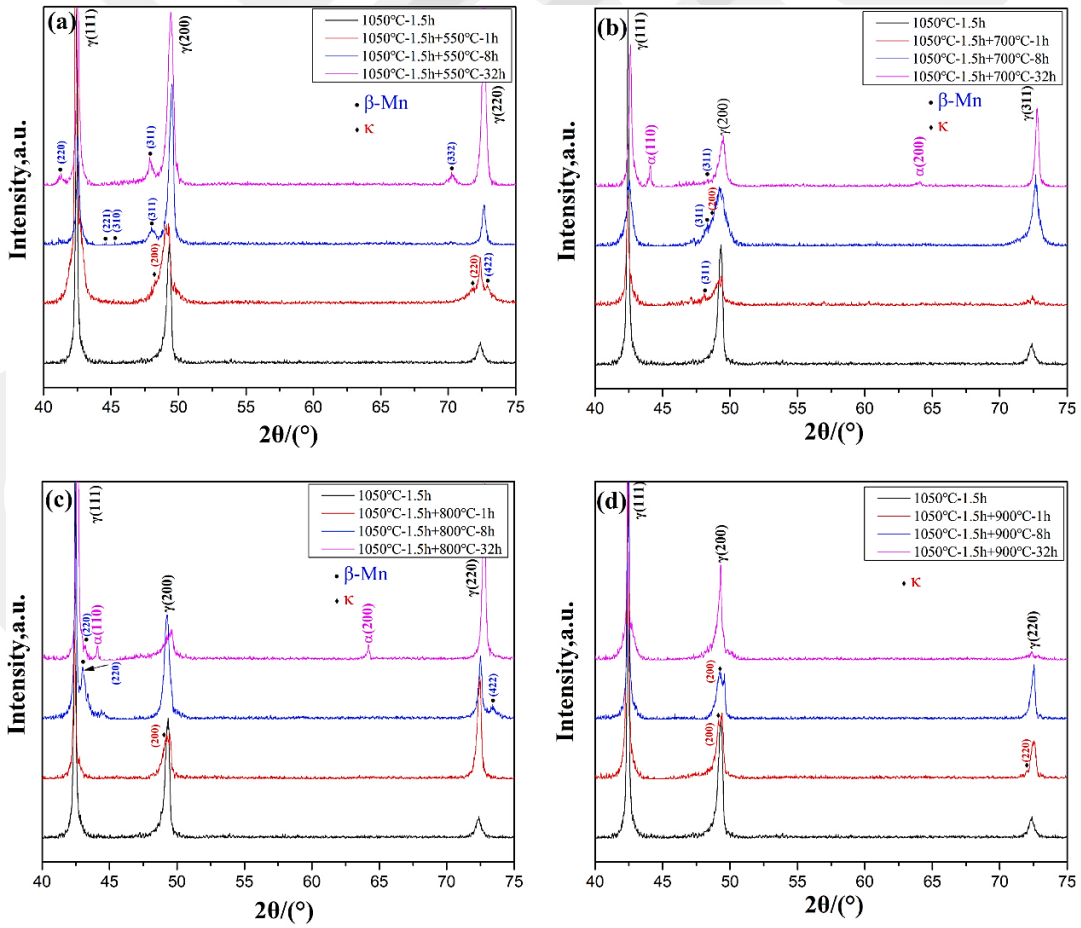

Figure 2.18 The XRD results of (a) A550, (b) A700 (c) A800 and (d) A900 for 1.38C, 31.6Mn, 8.8Al, 0.5Si (wt%)

2.3. Precipitation Hardening of Fe-Mn-Al-C Lightweight Steels

In steels with age hardenable properties in the Fe-Mn-Al-C system, first homogenization is performed at 1100-1250°C for 1-3 hours and then hot rolling or hot forging is performed up to 850-1000°C. Then, especially austenitic age hardenable lightweight steels are quenched by applying the solutionizing treatment for 1-4 hours between 900-1100°C, depending on their chemical composition, in the range where they are single-phase austenite. Also, the heat treatment process is shown schematically in *Figure 2.19*. Quenching is usually done with water, but different media (oil, etc.) can also be used. The purpose of quenching after the solution is to obtain single-phase austenite in the microstructure. In addition, it is critical for the alloying elements to be distributed homogeneously in the matrix after solutionizing and to form fine and matrix-distributed precipitates during aging. After solutionizing +quenching, aging between 450-650°C for 5-20 hours usually gives the best results in terms of mechanical properties. [4]

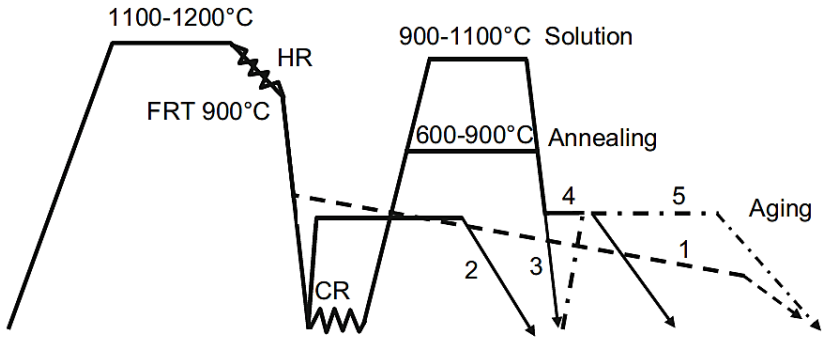

Figure 2.19 Process variants for making solution, aging, hot-rolled, and cold-rolled austenitic Fe–Mn–Al–C steel [4]

Generally, the temperature and time accepted in the literature for solutionizing in lightweight steels is 2 hours at 1050°C [15][28][42][43][44]. However, this temperature range varies depending on the chemical composition, so it is not always correct to choose the generally accepted time and temperature for the chemical composition to be worked on. In the study conducted by *Field and Limmer*, the effects of solution heat treatment were investigated [46]. For the chemical composition of Fe–30Mn–9Al–1C–1Si–0.5Mo (wt%) rolling was first performed, then solution treatment was performed between 900°C and 1075°C for 2 hours and water quench. The samples

taken into solution at different temperatures were subjected to aging treatment at different times at 500°C and the results were examined. In this study, for the selection of temperatures for the solutionizing treatment, the phase diagram of Fe–30Mn–1C–1Si depending on the aluminum percentage which was obtained by using *Thermo-Calc* software was used (*Figure 2.20*). In the relevant composition in the article, the single-phase austenite range for 9% Al is 870-1050°C. When higher temperatures are used for 9% Al, the delta-ferrite phase appears.

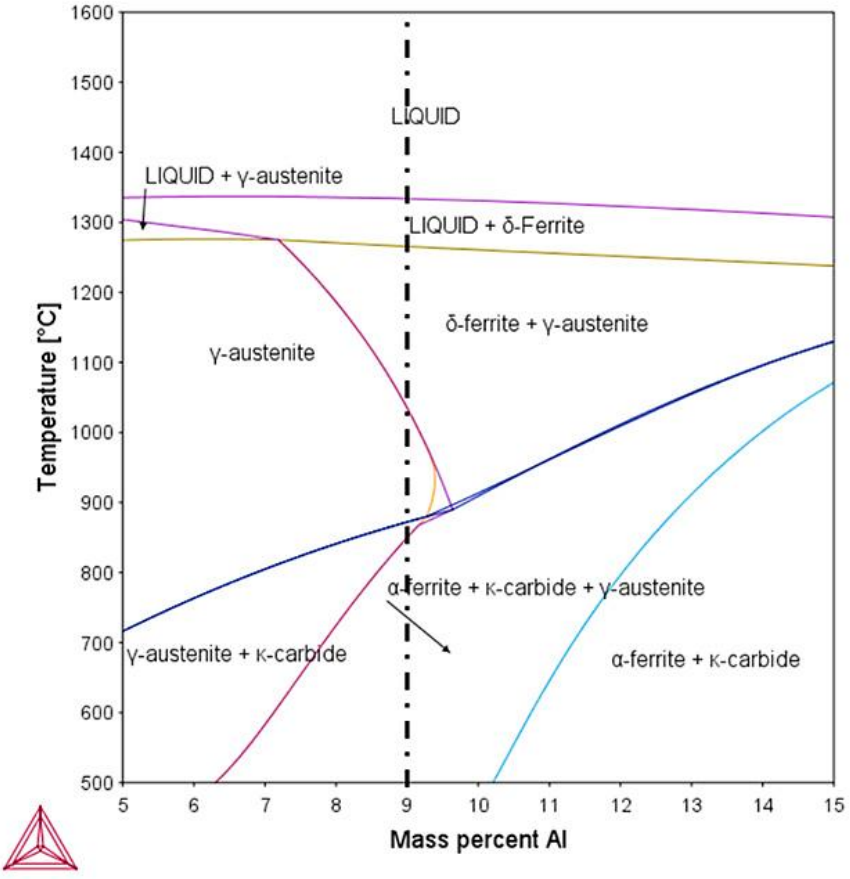

Figure 2.20 Phase diagram of the Fe-Al system with a specified silicon and carbon content of 1.0 wt.% and a fixed manganese concentration of 30 wt.%.

In the data in *Table 2.4*, with the increase in the solution temperature, the grain size increased while the hardness decreased. Later, in the aging of the samples taken into the solution at 950-1000-1050°C, the hardness values obtained after aging increased as the solutionizing temperature was decreased.

Table 2.4 Grain size and hardness values for different solutionizing and aging parameters

SOLUTION TREATMENT (2 h)			AGING (550°C)			
Temperature (°C)	Grain Size (μm)	Hardness (BHN)	5 hr.	20 hr.	66 hr.	120 hr.
			BHN	BHN	BHN	BHN
900	30 ±9	251 ±4	-	-	-	-
950	43 ±1	236 ±8	265 ±9	327 ±7	363 ±7	392 ±5
975	82 ±2	225 ±4	-	-	-	-
1000	156 ±2	218 ±8	222 ±11	280 ±22	345 ±6	364 ±19
1050	201 ±1	203 ±5	201 ±11	210 ±22	296 ±15	312 ±14
1075	327 ±1	201 ±7	-	-	-	-

In another study by *Field et al.*, lightweight steel with the chemical composition of Fe-30.8Mn-9.2Al-0.7Si-1.0C-0.5Mo (in wt.%) was solution heat treated for 30 minutes to 15 hours at temperatures similar to the previous study (900°C to 1075°C) and then water quenched [47]. The study shows that while the grain growth after 30 minutes and 4 hours of solution at 900°C is negligible, the difference in grain size between 30 minutes and 4 hours of solution at 1075°C is much greater (*Figure 2.21*).

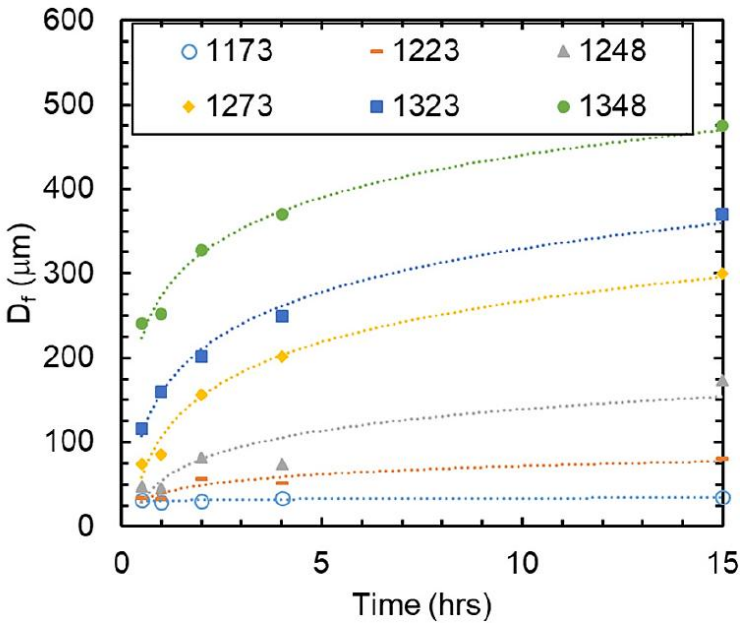

Figure 2.21 Grain size of austenite showing a parabolic response as a function of temperature (K) and annealing time (hour) [47]

The mechanical properties after solution heat treatment at different temperatures for two hours for the relevant chemical composition are as shown in *Table 2.5*. With the increase in solution temperature, hardness, yield and UTS decreased, while grain size and elongation increased.

Table 2.5 Mechanical properties of the solution treated for two hours Samples of Fe-30.8Mn-9.2Al-0.7Si-1.0C-0.5Mo (wt %)

TEMPERATURE (°C)	HARDNESS (HBW)	GRAIN SIZE (µm)	YIELD STRENGTH (MPa)	UTS (MPa)	EL (%)
900	245 ±7	30 ±2	555 ±7	957 ±7	63 ±1
950	236 ±9	57 ±8	505 ±1	919 ±4	72 ±2
1000	224 ±3	156 ±6	440 ±2	851 ±13	83 ±4
1050	201 ±2	201 ±8	410 ±6	811 ±4	86 ±7

Although the generally accepted solution heat treatment in the literature is seen as 1050°C and 2 hours, some studies show that it should be selected specifically for the chemical composition and targeted mechanical properties. ST temperature and time are very critical as it directly affects the aging process to be performed after solution heat treatment.

Aging heat treatment is generally found to be between 425°C and 675°C for austenitic Fe-Mn-Al-C steels [48]. The ageing range may vary depending on the chemical composition, and as the temperature increases, precipitates that will form and coarsening at the grain boundaries adversely affect the mechanical properties. The first detailed aging study was conducted by *Kayak* in 1969 [10]. More than 100 samples with chemical compositions of 5-45% Mn, 2-14% Al, and 0.05-1.5% C were prepared in the study. In addition to aging, another important result of the study is that high manganese (~30%) and high carbon (~1%) are required to obtain an austenitic structure. The formation of ferrite due to the decrease in manganese and carbon and the high aluminum content was observed in the study, and this was confirmed by later studies. Aging experiments started with samples with the relevant chemical composition being put into solution at 1150°C for 1.5 hours and quenched, and then aging at 400°C, 500°C, 550°C, 600°C and 700°C for 30 minutes and 100 hours was completed. After aging, it was observed that the precipitates formed between 400-

500°C were minimal and negligible, and that the mechanical properties were adversely affected as the temperature increased (600-700°C) as a result of the coarsening of the precipitates. Among the different chemical compositions tested in the study, the optimum range was 8-10% A1, 25-30% Mn, and ~1% C, and for the relevant composition range, UTS= 882–931 MPa and %EL= 10-20 were observed after aging at 550°C and 16 hours. This study provided the basis for understanding the aging mechanism and showed that optimum aging conditions were formed in terms of mechanical properties between 500-600°C.

Another study that is more recent and useful for understanding the aging mechanism was published by *Acselrad et al.* in 2006 [49]. Samples with the chemical composition Fe–28Mn–8.5Al–1C–1.25Si were rolled after homogenized at 1150°C for 6 h and water was quenched after solution treatment at 1050°C. Then, the samples were subjected to an aging process between 400-950°C, and different times. The obtained data and the phase distribution graph with time are as shown in *Figure 2.22*.

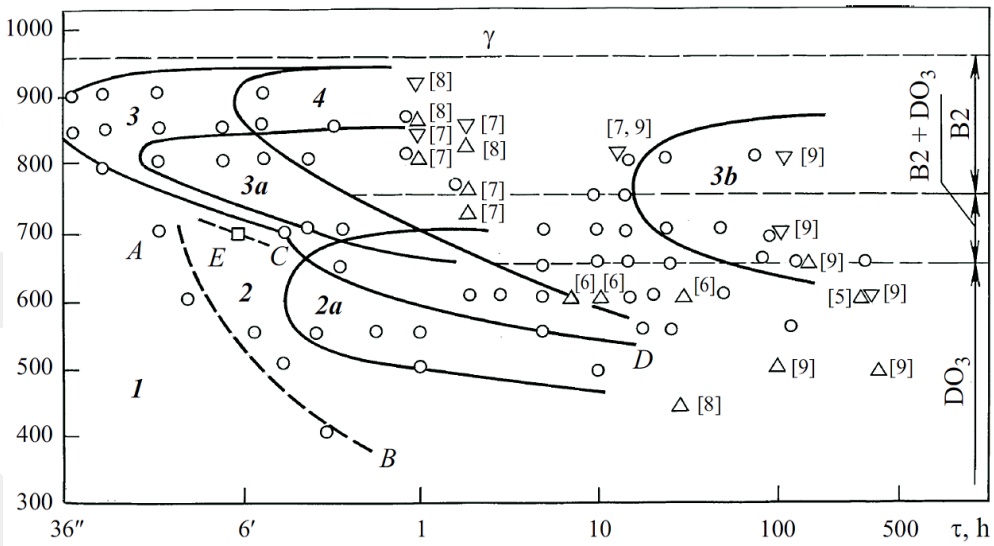

Figure 2.22 Diagram showing the austenite-solid solution's decomposition in a hardened alloy Fe–28Mn–8.5Al–1C–1.25Si ages in the 400–950°C temperature range during isothermal holding

The phase transformation diagram for the Fe–28Mn–8.5Al–1C–1.25Si alloy during isothermal aging is divided into four key regions based on decomposition mechanisms according to *Figure 2.22*: Region 1 involves spinodal decomposition at low

temperatures, where fine modulations form without distinct nucleation; Region 2 shows homogeneous segregation of κ-phase particles, with 2a marking the development of quasiperiodic structures; Region 3 includes heterogeneous segregation of κ phases both within grains and at boundaries, with 3a representing periodic particle arrangements and 3b indicating the equilibrium structure; Region 4 is characterized by discontinuous (cellular) decomposition, mainly along grain boundaries, forming κ and Fe–Al intermetallic phases. The AB curve separates the spinodal decomposition zone from the carbide segregation region, while the CD curve defines the lower-temperature boundary of heterogeneous decomposition. The B_2 phase (FeAl) exists between ~940–750°C, the $D0_3$ phase (Fe_3Al) below 650°C, and both coexist between 750–650°C.

In the study conducted by *Prodhan and Chakrabarti*, for the chemical compositions of ~30Mn, 1.5Si, 5-10Al and 0.3-0.9C, homogenization was performed at 1100°C for 1 hour and then aging was performed at 500°C, 600°C and 800°C for 10 to 10,000 minutes [50]. After the aging processes, it was observed that 5% aluminum content had very little effect on precipitation formation and the aging mechanism improved with increasing aluminum content, and likewise, increasing the amount of carbon had a positive effect on aging. It was observed that the hardness increase was the highest between 500°C and 600°C. Fe-30Mn-(7.5-10)Al-1.5Si-C: Alloys that contain 0.3%C and 0.9%C are particularly susceptible to age hardening between 500°C and 800°C.

Another study by *Acselrad et al.* showed that after aging for 10 hours at 700°C for the composition 28Mn-8.5Al-1C-1.25Si, κ-carbide colonies were observed to have a cellular structure in the SEM image as seen in *Figure 2.23*. These structures were not reported in the literature in previous studies. [27]

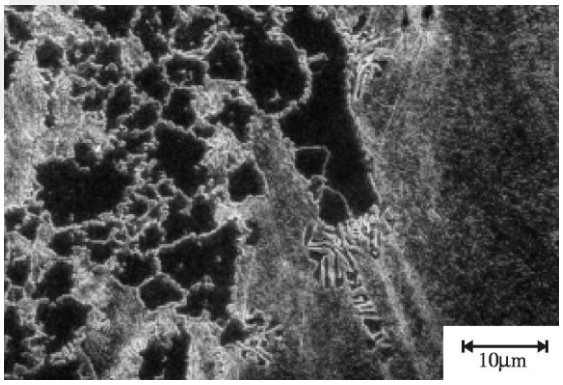

Figure 2.23 Cellular structure after 10 hours at 700°C for the 28Mn-8.5Al-1C-1.25Si

2.4. Hot Working Fe-Mn-Al-C Steels

Fe-Mn-Al-C steels, hot rolling and forging is generally done by deforming the steels at 1100-1250°C for 1 to 3 hours and up to critical temperatures. In some cases, intermediate heating may be required to prevent crack formation during rolling/forging. As-cast microstructure is too heterogeneous to be eliminated by homogenization or solution heat treatments alone, therefore the main reason for rolling/forging in lightweight steels is to ensure recrystallization by driving force can be supplied by a significant thickness reduction via rolling/forging. As a result of this process, a more homogeneous equiaxed austenitic grain structure containing annealing twins is observed. [51]

For example, in the study conducted by *Lee et al.*, after heat treatment at 1200°C for 2 h for Fe–0.8C–31.52Mn–8.73Al (wt%), samples were hot rolled up to 900°C and a total thickness reduction of 90% was reported [52]. In the study conducted by *Kang et al.*, ingots for the Fe-26Mn-5.84Al-1.0C (mass %) sample were hot-rolled to a thickness of 3 mm with an overall reduction of 85% after being homogenized for two hours at 1200°C. The samples were then solution heat treated at 1100°C for 1 hour and water quenched. After rolling and solution heat treatment, a homogeneous microstructure was obtained as shown in *Figure 2.24* [53].

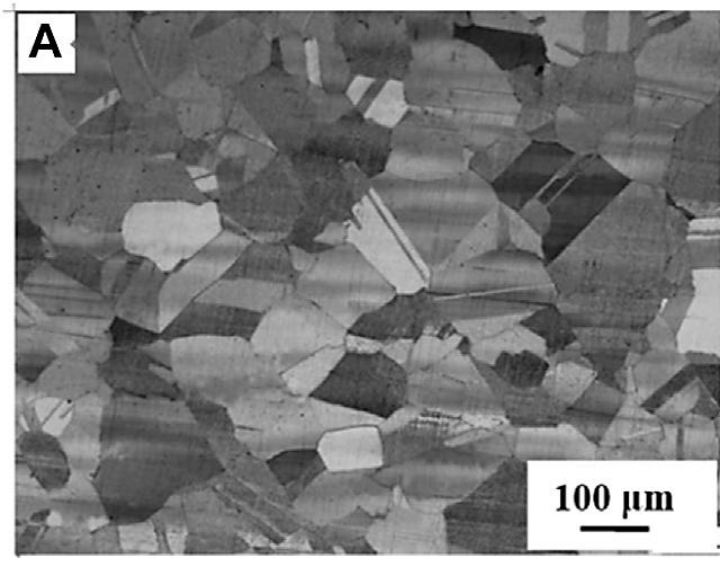

Figure 2.24 Fe-26Mn-5.84Al-1.0C optical micrographs after a 1-hour solution treatment at 1100°C

2.5. Mechanical Properties

In Fe-Mn-Al-C alloy systems, mechanical properties such as hardness, yield strength, tensile strength, and % elongation depend on many different factors. The chemical composition of the alloy system and the heat treatment parameters to be applied (solutionizing and aging temperatures and times) are the most important factors that directly affect the mechanical properties.

In the graph given in *Figure 2.25*, yield strength, UTS and %EL values are given after aging at different temperatures for 16 hours fixed time for Fe-30.9Mn-8Al-1C. In the 500-550°C range, %EL is higher than yield strength and UTS. When the temperature increases from 550°C to 600°C, yield strength and UTS increase, while %EL decreases as a result of the precipitation that will occur due to the temperature increase. According to this graph, the optimum aging range is seen in the around 550°C.

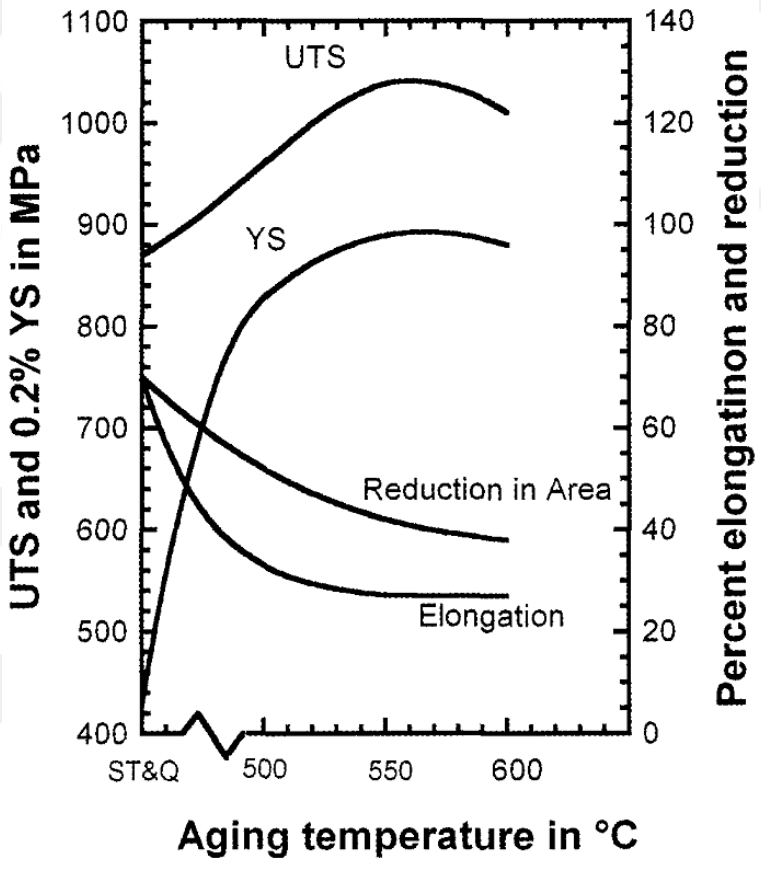

Figure 2.25 Mechanical property changes for Fe-30.9Mn-8Al-1C after 16 hours of aging at different temperatures [17]

According to the temperature and time dependent hardness results given for the Fe-30.4Mn-8Al-lC-0.35Si composition in *Figure 2.26*, higher hardnesses are obtained at high temperatures in the aging process carried out in short periods, while the hardness increase at high temperatures progresses negatively with the increase in aging time, while low temperatures give better results in long aging times.

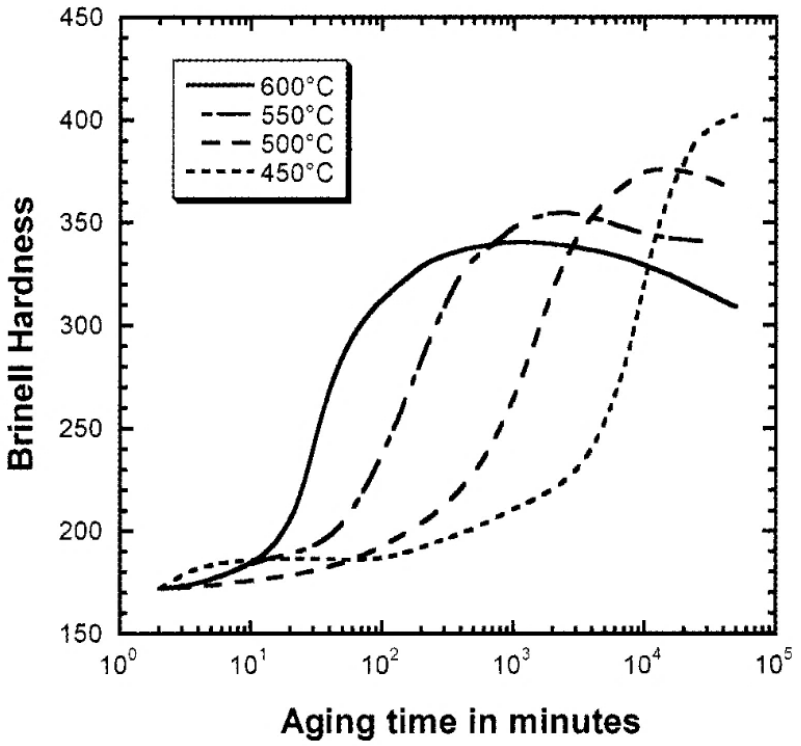

Figure 2.26 Fe-30.4Mn-8Al-lC-0.35Si aging curves at 450, 500, 550, and 600°C [17]

In the study conducted by *Howell et al.*, solution heat treatment was applied at 1050°C for 2 hours for Fe-28.8Mn-8.3Al-0.9C-1.0Si-0.5Mo and Fe-28.8Mn-7.9Al-0.9C-1.4Si-0.5Mo compositions and then aging was done at 530°C for 1, 3, 6, 10, 30, and 60 hours [21]. The most important alloy difference between the two compositions is silicon. According to the hardness results given in *Figure 2.27* for the compositions, the hardness results after solution heat treatment were measured as 224 HB for the sample containing 1.0% Si and 219 HB for the sample containing 1.4% Si. After aging, the hardness of the sample containing 1.4% Si was always measured higher than that of 1% Si. The hardness increase was high in the first 10 hours for both compositions, and the hardness continued to increase until 30 hours, while the rate entered a

decreasing trend. Again, the highest hardness values for both compositions were measured as 372 HB for 1.0%Si and 384 HB for 1.4%Si after 30 hours of aging. After 60 hours, the hardnesses started to decrease.

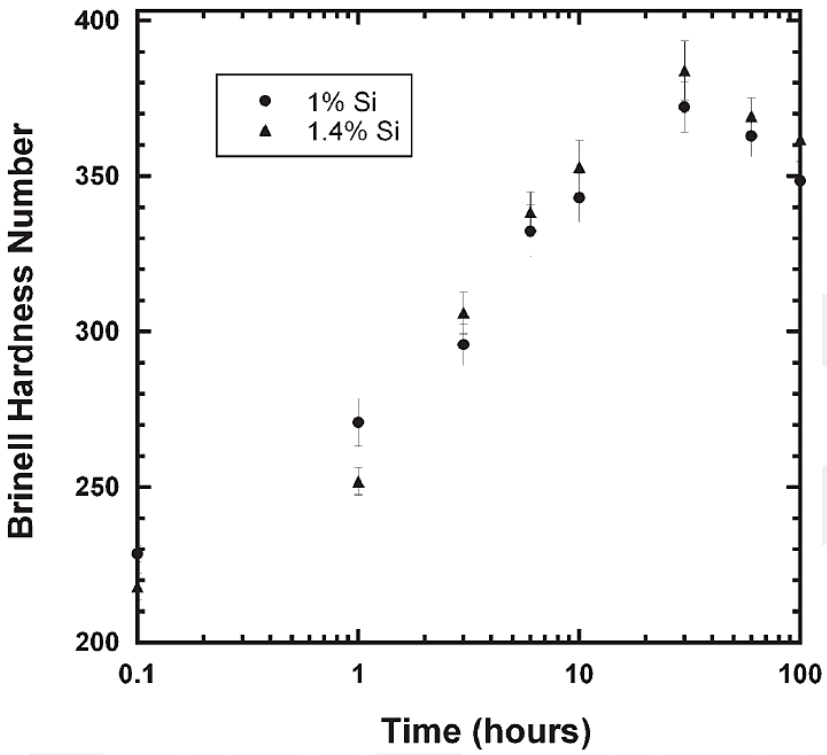

Figure 2.27 The hardness results of the compositions Fe-28.8Mn-8.3Al-0.9C-1.0Si-0.5Mo and Fe-28.8Mn-7.9Al-0.9C-1.4Si-0.5Mo were aged at 530°C for 1, 3, 6, 10, 30, and 60 hours

In the same study, 3 different conditions were tested for tensile tests for compositions containing 1.0% Si and 1.4% Si. These conditions were solution heat treatment, 10 and 30 hours of aging at 530°C. According to the results given in *Table 2.6*, the yield and tensile strength results of the sample containing 1.4% Si were higher than the sample containing 1% Si, while the % elongation and work hardening rate of the sample containing 1% Si were higher. There was no dramatic increase in mechanical properties after 10 and 30 hours of aging for either composition. The 20-hour aging period spent between 10 and 30 hours did not increase yield and tensile properties much but decreased % elongation at higher rates.

Table 2.6 The mechanical properties of the compositions Fe-28.8Mn-8.3Al-0.9C-1.0Si-0.5Mo and Fe-28.8Mn-7.9Al-0.9C-1.4Si-0.5Mo were solution-treated and aged at 530°C for 10 and 30 hours

Alloy	Heat Treat Condition	BHN	Yield Strength (MPa)	Tensile Strength (MPa)	% Elongation	Work Hardening Exponent
1% Si	Sol'n Treat	224	458	687	44	0.32
	10hr 530°C	343	891	940	18	0.08
	30hr 530°C	372	1005	1065	8	0.06
1.4%Si	Sol'n Treat	219	549	766	36	0.23
	10hr 530°C	353	922	995	14	0.07
	30hr 530°C	384	1016	1085	5	0.05

Another study was carried out by *Bartlett et al.* for the chemical compositions given in *Table 2.7*, after 2 hours of solution heat treatment at 1050°C, aging was carried out at different temperatures and times. [54]

Table 2.7 Chemical compositions used in the study (wt%) [54]

Si	C	Mn	P	S	Mo	Al	Cu	Fe
0.59	0.95	30.35	0.002	0.006	0.54	8.74	0.010	Bal.
1.07	0.90	30.42	0.001	0.006	0.53	8.83	0.006	Bal.
1.56	0.89	29.97	0.002	0.007	0.53	8.81	0.006	Bal.

The hardness values obtained after aging at 530°C for the chemical compositions in *Table 2.7* are given in *Figure 2.28*. The increase in silicon content led to higher hardness at similar aging times.

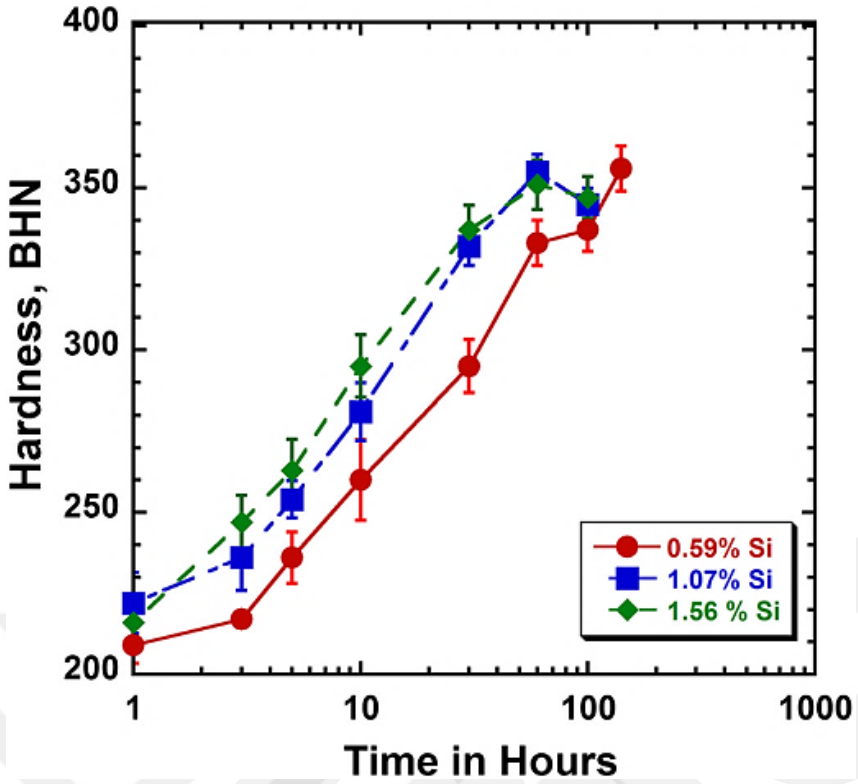

Figure 2.28 Hardness results for 0.59%Si, 1.07%Si and 1.56%Si after aging at 530°C for different times [54]

In the study conducted by *Feng et al.*, solution heat treatment was performed at 1050°C for 1.5 hours for Fe-31.6Mn-8.8Al-1.38C-0.5Si and then water quenched. The samples were subjected to the aging process at different times at 550°C, 700°C, 800°C and 900°C. According to the results in *Figure 2.29*, the hardness at all temperatures first increased and then tended to be constant. The graph shows that higher temperatures give higher hardness at short times, which can be attributed to the faster precipitate formation and coarsening of the precipitates due to high temperatures. Due to the balance between high temperature softening and age hardening, the hardness value remained stable during a lengthy period of aging. The hardness of the A700 and A800 specimens approached a consistent value with 320 HB after more than five hours of aging. Additionally, after aging for more than three hours, the hardness of the A900 achieved a constant value of 300 HB. However, after aging for more than 15 hours, the hardness of A550 approached and stabilized at a value of roughly 480 HB. [32]

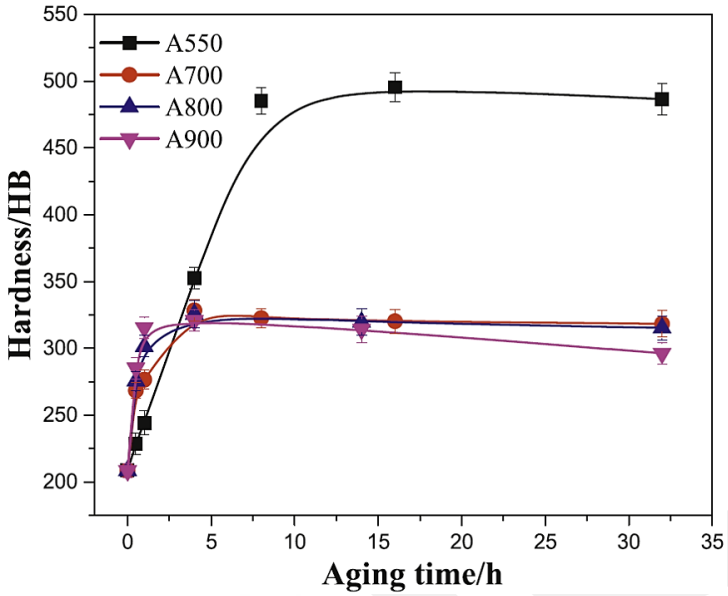

Figure 2.29 Hardness curves about aging time for specimens A550, A700, A800, and A900 [32]

In the study conducted by *Acselrad et al.*, three different heat treatment conditions were tested for 29.4Mn-8.8Al-1.33Si-1C alloy [55]. According to the results given in *Table 2.8*, after solution heat treatment at 1050°C, the sample was quenched in water and the mechanical properties; elongation, tensile strength, and yield strength were 77%, 871 MPa, and 620 MPa, respectively. After aging at 550°C for 16 hours, the mechanical properties; elongation, tensile strength, and yield strength were 15%, 1210 MPa, and 884 MPa, respectively. In the last tested condition, the sample was quenched in a salt bath at 700°C, held for 4 seconds, then cooled to room temperature at a rate of 0.05°C/s.

Table 2.8 Mechanical properties of three different heat treatment conditions for Fe-29.4Mn-8.8Al-1.33Si-1C [55]

Processing Condition	$\sigma_{0.2}$ (MPa)	UTS (MPa)	Elongation (%)	*Brinell Hardness	Charpy Energy (J/cm^2)	Fracture Toughness K_A (MPa$\sqrt{m}$)
Solutionized	620	871	77	272	51	330
Aged 16hr @ 550°C	884	1210	15	434	1.4	84
Controlled Quench	705	1100	32	392	1.2	104
*Converted from HRc						

CHAPTER 3

EXPERIMENTAL

3.1. Casting and Preparation of the Samples

Keel blocks of target composition were sand cast using an induction melting furnace by *Akdaş Döküm* (Ankara, Türkiye). Keel Block tooth dimensions are 288 mm in length, tooth base width is 45 mm, tooth top width is 30 mm, tooth thickness is 40 mm (*Figure 3.1*).

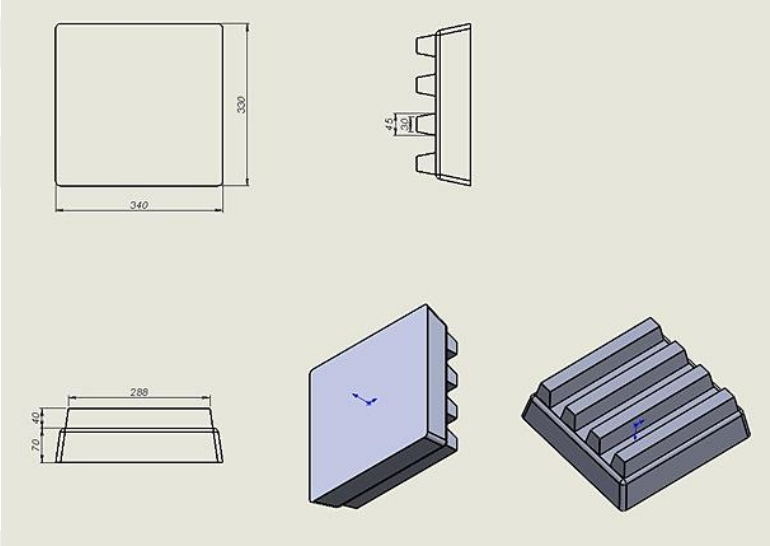

Figure 3.1 Dimensions of the Keel block

The chemical composition of the cast blocks is given in *Table 3.1* Chemical composition analyses were conducted using the *Thermo Scientific™ Element GD Plus™ GD-MS* and *LECO CS 744 Series*.

Table 3.1 Chemical Composition of the Fe-Mn-Al-C-Si Samples

Mn	Al	C	Si	Fe	*wt%*
30.92	9.36	1.10	1.01	Bal.	

The disk samples were cut from the block using Electro Discharge Machining (EDM) for related tests and analysis. The disk samples were cut with a diameter of 25 mm and a thickness of 11 mm (*Figure 3.2*). Testing of these disk-shaped samples aims to explore and analyze various heat treatment conditions. As a part of this plan, solution heat treatment and aging were evaluated at different temperatures and times on the disk samples. Subsequently, a series of relevant tests were conducted. The tests applied to the disk samples included Density Calculations, Microstructure Examination, Hardness Testing, Nanohardness Testing, X-Ray Diffraction (XRD), Scanning Electron Microscopy (SEM) with Energy Dispersive Spectroscopy (EDS)/Electron Backscatter Diffraction (EBSD), and Wear Testing.

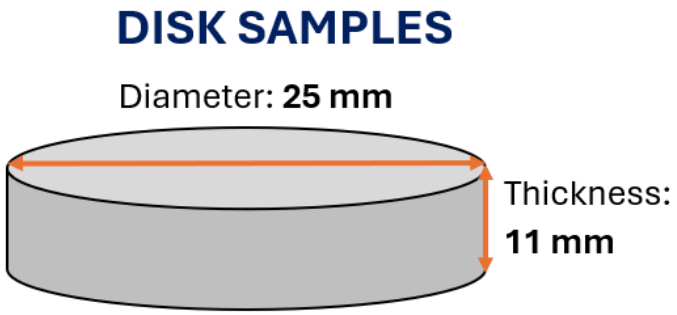

Figure 3.2 Illustration of the location where disk samples were cut on the Keel Block and the dimensions of the disk sample

3.2. Density Calculations

Density calculations were made by weighing disk samples with a precision balance and measuring sample dimensions with calipers. *Denver Instrument TP-214* (S/N: 21760049) of the precision balance shown in *Figure 3.3* was used.

Figure 3.3 Denver Instrument precision balance device

Density calculations were made in two different methods. First, calculations were made in g/cm^3 using the obtained data and Equation (3.1). In the second method, the density was found based on theoretical calculations found in the literature, indicated Equation (3.2) in unit g/cm^3 [20]. Aluminum and carbon have a significant effect on reducing density.

$$\rho = \frac{m}{V} \tag{3.1}$$

$\boldsymbol{\rho}$: density , $\boldsymbol{m}$: mass , $\boldsymbol{V}$: volume

$$\rho = 8.10 - 0.101(\%Al) - 0.41(\&C) - 0.0085\ (\%Mn) \tag{3.2}$$

3.3. Thermodynamic Analysis

Thermodynamic calculations were carried out with *Thermo-Calc* software for the chemical composition given in *Table 3.1*.

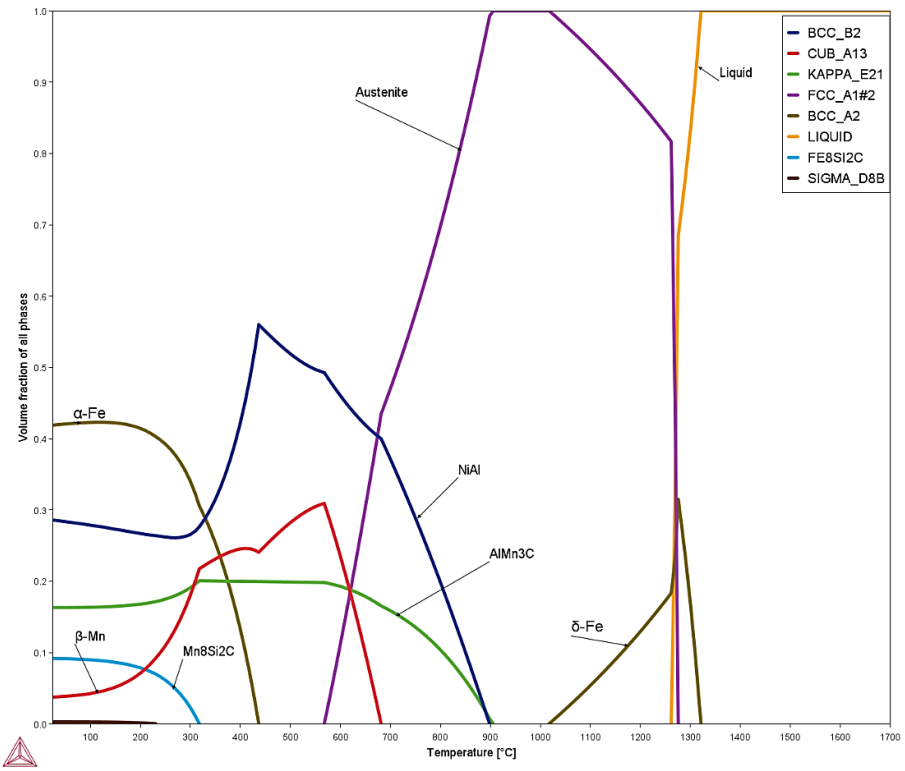

Figure 3.4 Variation of equilibrium phase fractions in the experimental steel with respect to temperature

According to *Figure 3.4*, steel is in liquid state at 1350°C. Solidification begins with the formation of delta-ferrite at 1320°C. At 1276°C, the austenite phase emerges, and solidification is completed at 1262°C. Delta-ferrite is entirely dissolved at 1017°C. A fully austenite microstructure is present between 1017°C and 915°C. At 900°C, B_2 (FeAl) and κ-carbide ($(Fe,Mn)_3AlC$) precipitates appear in the microstructure, remaining at varying concentrations up to room temperature. β-Mn is formed at 680°C. According to the calculation, the austenite phase in the microstructure is completely dissolved at 568°C. The alpha-ferrite phase begins to form around 435°C, with its fraction increasing until reaching room temperature. Especially the calculations made with *Thermo-Calc* were used for solutionizing. According to literature and graphics, 1000°C was selected as the solutionizing temperature in the range of single-phase austenite.

3.4. Heat Treatments

Shown in *Figure 3.5, Protherm MoS-B 170/8* furnace was used for heat treatments (Solutionizing + Aging). To verify the temperature indicator of the furnace, a verification test was conducted using an *ORDEL* brand *OM02 N-Type* thermocouple, a *UDL100* data collector, and *DaLi08* software. After setting the oven to 1150°C and allowing it to reach equilibrium, observed a difference of 5-8°C between the oven's temperature indicator and the thermocouple readings.

Figure 3.5 Protherm MoS-B 170/8 furnace

Heat treatments were first conducted by placing the sample in a solution, followed by water quenching at 25°C. After that, it undergoes aging for a specified time and temperature. The schematic representation of the heat treatment process is given in *Figure 3.6*.

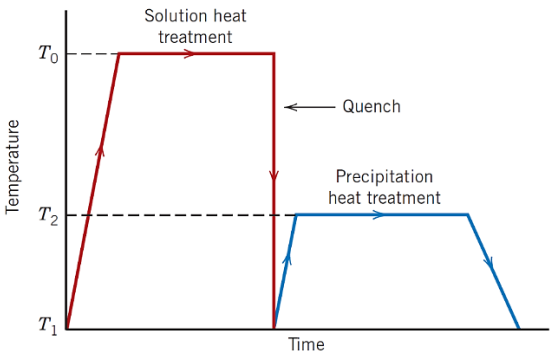

Figure 3.6 Schematic representation of solution and aging heat treatment [56]

Heat treatment temperatures and times were tested on disk samples. For this purpose, two different Test Levels were planned. These are **Test Level S** and **Test Level A** (*Figure 3.7*). The first tests started with Test Level S and the optimum solution heat treatment temperature and time were selected. Then, the solution heat treatment selected in Test Level A was kept constant and the tests continued with different aging temperatures and times. Further details are provided below, and all data are given in detail in *Table 3.2*.

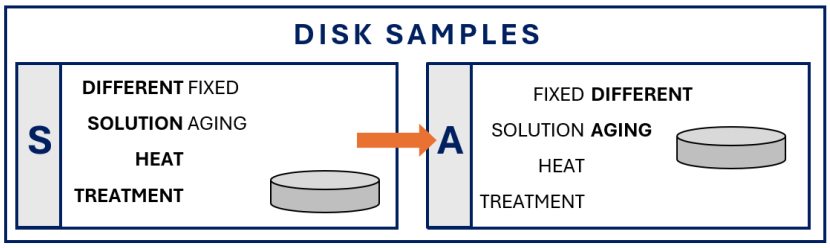

Figure 3.7 Disk sample heat treatment plan

- **TEST LEVEL S:** To select the optimal solution heat treatment, the aging parameter that yields the best results in the literature is chosen and kept constant. The selected aging condition is 550°C for 16 hours [32][55]. With the aging parameter held constant, the solution heat treatment parameters are varied at different temperatures and times based on literature and *Thermo-Calc* data. The goal is to determine which solution heat treatment conditions give the best results under the same aging conditions. Solution heat treatment is applied at temperatures of 950°C, 1000°C, 1050°C, and 1150°C for times ranging from 2 to 4 hours. Additionally, solution heat treatment was applied at 950°C for 16 hours to see the effect of long-term solution heat treatment.

- **TEST LEVEL A:** In Test Level A, we evaluate different aging temperatures and times while keeping the optimal solution heat treatment parameter, determined in Test Level S, constant. The selected solution heat treatment parameter—1000°C for 4 hours from Test Level S—remains fixed. The aging conditions are tested at temperatures of 500°C, 550°C, and 600°C for a time of 4, 16, and 64 hours. Additionally, 16 hours of aging at 400-450-650-700°C was applied to the samples. To see the effect of low temperature for a long time, aging was done at 400°C for one week.

Table 3.2 Heat treatment and testing plan

SOLUTION HEAT TREATMENT				AGING				TEST LEVEL
Temperature (°C)	Time (h)	Cooling	Test	Temperature (°C)	Time (h)	Cooling	Test	
950	2	+Water Quench at 25°C	Microstructure Examination Hardness	550	16	+Air	Microstructure Examination Hardness XRD SEM Wear Test	S
950	4			550	16			
950	16			550	16			
1000	4			550	16			
1050	2			550	16			
1050	4			550	16			
1150	2			550	16			
1150	4			550	16			
↓ SELECTED BEST ST, CONTINUE WITH AGING ↓								
1000	4	++Water Quench at 25°C	-	400	16	+Air	Microstructure Examination Hardness XRD SEM Wear Test	A
1000	4			400	1 Week			
1000	4			450	16			
1000	4			500	4			
1000	4			500	16			
1000	4			500	64			
1000	4			550	4			
1000	4			550	16			
1000	4			550	64			
1000	4			600	4			
1000	4			600	16			
1000	4			600	64			
1000	4			650	16			
1000	4			700	16			

KEPT CONSTANT

KEPT CONSTANT

3.5. Characterization of the Samples

3.5.1. Microstructural Examination

Microstructural examinations were done on disk samples. The process began with grinding at 180-320-600-1200-2500 SiC papers, followed by polishing at 6 µm, 3 µm, and 1 µm with diamond paste. The mounting and grinding/polishing were performed using the *Metkon ECOPRESS 102* and *FORCIPOL 202* (*Figure 3.8*).

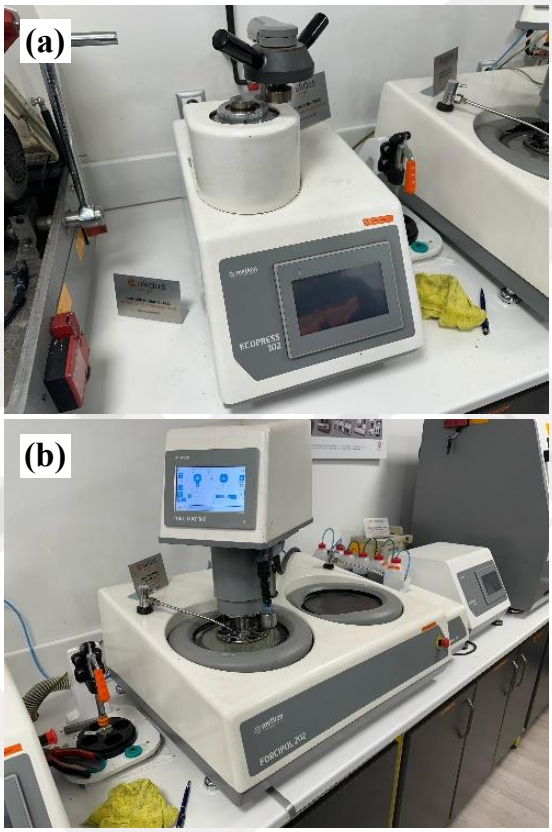

Figure 3.8 Metkon (a) ECOPRESS 102 and (b) FORCIPOL 202

Then, the samples were etched with different etchants, and the most efficient one was selected and used for all samples. Different amounts of Nital (3%, 5% and 10%) and *Vilella's* (ASTM E407 - Etchant No: 80) were tried for sample etching, See *Appendix A* for details. As a final selection, the samples were etched with Vilella's for 50 seconds [57]. Vilella's content is 5 mL HCl, 1 g picric acid and 100 mL ethanol (95%) or methanol (95%). Microstructure images were taken with *Nikon MA100* optical microscope at 100X, 200X and 500X (*Figure 3.9*).

Figure 3.9 NikonMA100 optical microscope

For electron microscopical investigations the *ZEISS MERLIN* Scanning Electron Microscope (SEM) equipped with EDAX Energy Dispersive X-Ray Spectroscopy (EDS) and Electron Backscatter Diffraction (EBSD) analysis was used (*Figure 3.10*). For advanced analysis methods, in addition to the grinding + polishing + etching sequence mentioned above, final polishing was done with Colloidal Silica. For SEM images, the accelerating voltage was set to 15 kV, and the probe current was adjusted to 1 nA.

Figure 3.10 ZEISS MERLIN Scanning Electron Microscope (SEM) equipped with EDS and EBSD

3.5.2. X-Ray Diffraction (XRD)

Rigaku SmartLab device was used for X-Ray Diffraction tests (*Figure 3.11*). X-Ray source was Cu-Kα at 40 kV and 40 mA. Diffraction was taken between 20°-100° at a scan rate of 1.5° per minute with a step size of 0.01°. *OriginPro 2025 Learning Edition* software was used to graph and analyze XRD results [58].

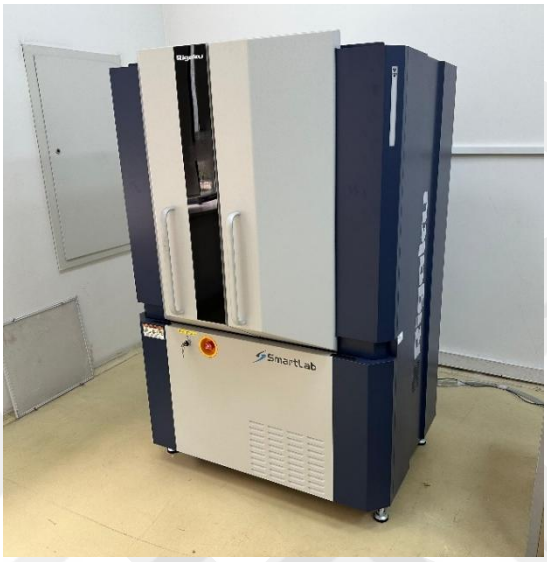

Figure 3.11 Rigaku SmartLab XRD

3.5.3. Hardness Measurements

Microhardness measurements (Brinell, HB) were performed using the *EMCOTEST DuraVision 30 G5* hardness tester (*Figure 3.12*) according to the ASTM E10 [59]. Five measurements were made for each sample using a 10 mm diameter ball indenter under the load of 3000 kgf.

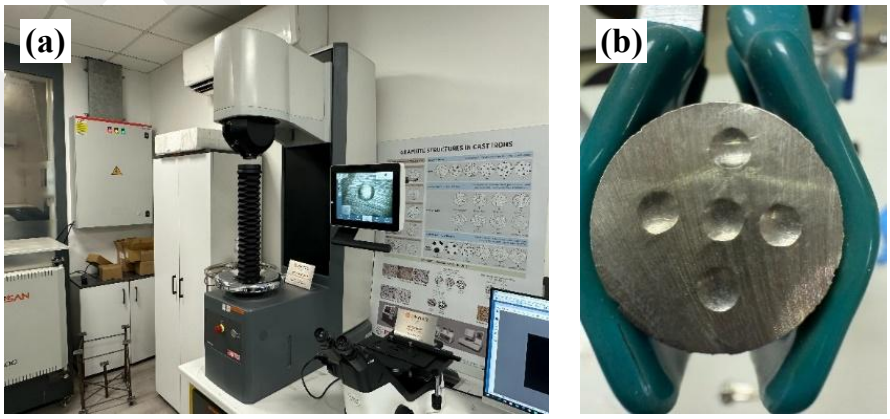

Figure 3.12 (a) EMCOTEST DuraVision 30 G5 (b) Hardness location

Nanohardness measurements were performed using a *CSM Instruments* with a Berkovich (Serial Number: BO56, Diamond) in *Figure 3.13*. The indents were made under a load of 25 mN.

Figure 3.13 CSM Instruments nanohardness device

3.5.4. Tensile Tests

Tensile tests were performed using the *MTS C45.305* tensile test machine (*Figure 3.14*). Tensile testing was performed according to ASTM E8 standard for as-cast condition only [60]. The samples were prepared according to the "*Pin-Loaded Tension Test Specimen with 50-mm*" dimensions of the relevant standard.

Figure 3.14 (a) MTS C45.305 tensile test machine (b) sample

3.5.5. Wear Tests

The wear tests were performed using the custom design wear test machine at *Atılım University* (*Figure 3.15*). The tests were carried out under a constant load of 84.34 N. Zirconia ball of 6 mm was used as a counter face material. The average diameter of the wear tracks was 14 mm. Rotational speed during the wear tests was 150 rpm. Time of the wear tests was 2 hours which correspond to 18,000 cycles and 791.3 m of total sliding distance.

During the wear tests, the ambient temperature was 25°C, and the recorded relative humidity was about 40%. The wear rates were calculated using the formula provided in Equation (3.3). Denver Instrument TP-214 (S/N: 21760049) precision balance was used to weigh the samples before and after the wear tests.

$$Wear\ Rate = \frac{\Delta m}{S*N}\left(\frac{g}{N*m}\right) \tag{3.3}$$

Δm: $Mass\ change\ of\ the\ sample\ (in\ grams)$

S: Total Sliding Distance (m)

N: $Total\ load\ applied\ during\ the\ test\ (in\ Newtons)$

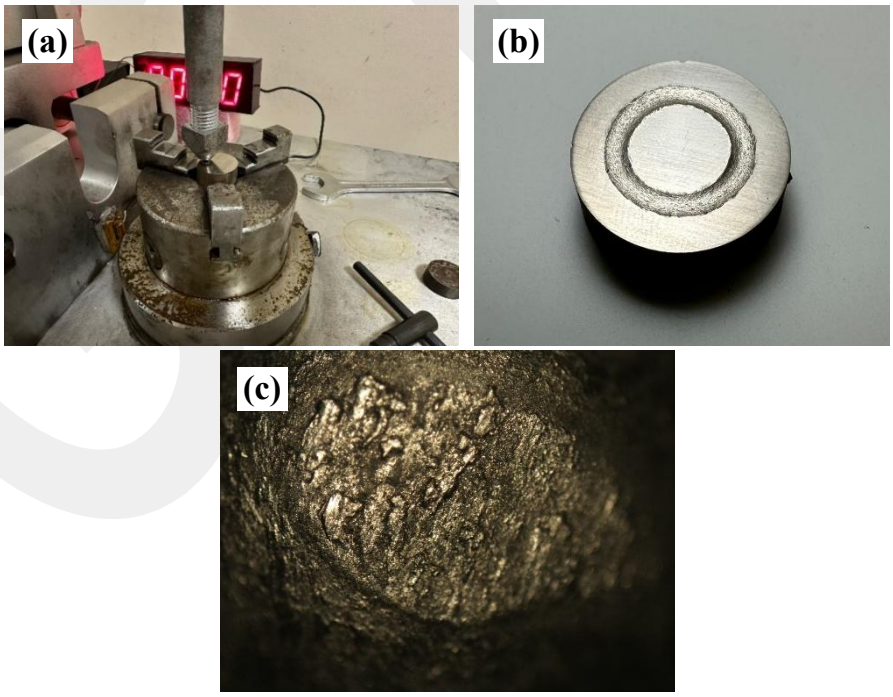

Figure 3.15 (a) Pin-on-Disk type wear test device (b) sample after wear test (c) worn ball surface 50X

CHAPTER 4

RESULTS

4.1. Density Calculations

The density of the samples was calculated by measuring the volume and mass of the disk samples. The density was calculated using Equation (3.1). As shown in *Table 4.1*, density calculations were made on 3 different samples, and the average density was calculated as 6.60 g/cm^3.

Table 4.1 Calculated densities of the samples

Sample	Mass (g)	Volume (cm^3)	**Density (g/cm^3)**
1	32.96	5.01	6.585
2	32.95	5.00	6.590
3	35.62	5.39	6.613
Average Density			**6.60**
Standard Deviation			*0.015*

In the literature, the calculation for density is made using the formula given in Equation (3.2), which is based on the chemical composition. As a result of the calculation made with the relevant formula, the density was calculated as 6.78 g/cm^3.

$$\rho = 8.10 - 0.101(\%Al) - 0.41(\%C) - 0.0085\ (\%Mn)\ [20] \qquad (3.2)$$

$$\rho = 8.10 - 0.101(9{,}36) - 0.41(1{,}1) - 0.0085\ (30{,}92)$$

$$\boldsymbol{\rho = 6.78\ g/cm^3}$$

4.2. Hardness and Tensile Properties

Hardness measurements were conducted on disk samples, with five measurements taken from each disk. The as-cast average hardness is 347.8 HB (Standard Deviation: 10.99). The nanohardness measurements were additionally performed on as-cast samples. The average nanohardness values were measured as 7.5 GPa (Standard Deviation: 0.5) as a result of the test. As shown in *Figure 4.1*, 19 hardness measurements were taken along a straight line. As a result of the mechanical test performed in the as-cast condition, the average tensile strength was measured as 692 MPa.

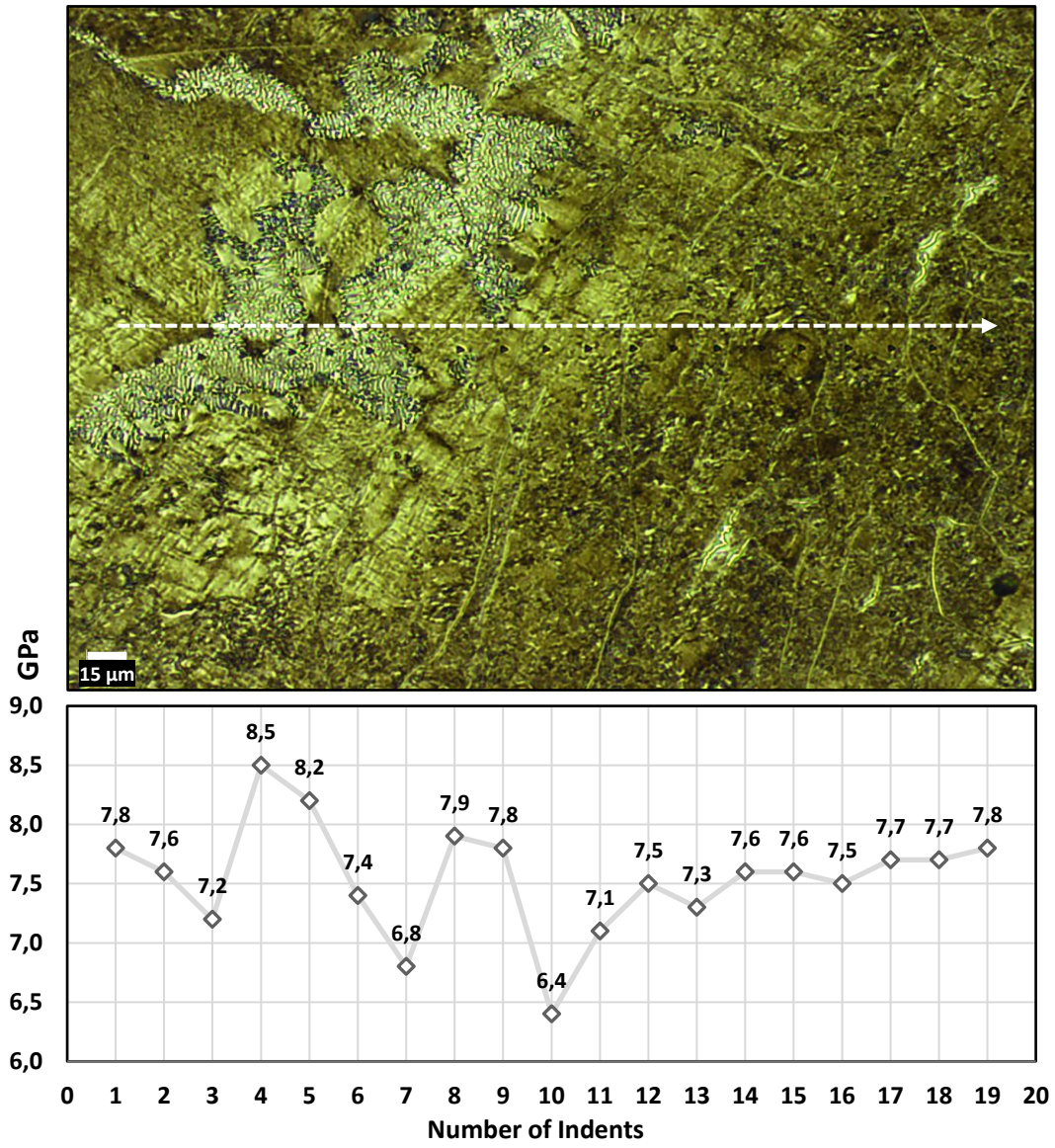

Figure 4.1 Locations of the indents (top) and measured nanohardness values (bottom)

Hardnes values of the solution heat treated samples are as given in *Table 4.2*. For solution heat treatment at 950°C, the average hardnesses were measured as 217.6 HB for 2 h, 213.6 HB for 4 h, and 204.6 HB for 16 h. The average hardness for solution heat treatment at 1000°C was measured as 212.6 HB for 4 hours. For the solution heat treatment at 1050°C, the average hardness was measured as 214.8 HB for 2 hours and 205.4 HB for 4 hours. At 1150°C, the average hardness for the solution heat treatment was measured as 202.6 HB for 2 hours and 189.4 HB for 4 hours.

Table 4.2 Brinell hardness values of the as-cast and solution heat treated samples

Temperature	**950**°C			**1000**°C	**1050**°C		**1150**°C		**As-cast**
Time (h)	**2**	**4**	**16**	**4**	**2**	**4**	**2**	**4**	
1	223	213	212	221	213	192	205	204	357
2	221	203	209	191	211	213	201	196	359
3	212	217	191	216	212	199	201	191	335
4	223	220	205	217	218	212	201	177	343
5	209	215	206	218	220	211	205	176	359
Average	**217.6**	**213.6**	**204.6**	**212.6**	**214.8**	**205.4**	**202.6**	**189.4**	**347.8**
Standard Deviation	*6.62*	*6.47*	*8.08*	*12.22*	*3.96*	*9.40*	*2.19*	*11.41*	*10.99*

As described in the test planning, the aging temperature and time (550°C-16 hours) were kept constant to select the optimum solution heat treatment temperature and time. *Table 4.3* shows the hardness values of the solution heat treatment samples to which a fixed aging temperature and time. When samples taken into solution heat treatment at 950°C for 2-4-16 hours are then aged at 550°C and 16 hours, the hardness values are 396.4 HB for 2 hours, 411.8 HB for 4 hours, and 376 for 16 hours. After 1000°C and 4 hours of solution heat treatment and aging at 550°C for 16 hours, the hardness reached 368 HB. When the samples were taken into solution heat treatment at 1050°C for 2-4 hours and then aged at 550°C and 16 hours, the hardness values were 370.8 HB for 2 hours and 381.2 HB for 4 hours. After solution heat treatment at 1150°C for 2 and 4 hours, the samples were aged at 550°C and 16 hours, then the hardnesses were measured as 356.6 HB for 2 hours and 361.8 HB for 4 hours.

Table 4.3 Brinell hardness of the samples solutionized at different conditions and then aged at 550°C for 16 hours

ST	Temperature	950°C			1000°C	1050°C		1150°C		As-cast
	Time (h)	2	4	16	4	2	4	2	4	
AGING	Temperature	550°C								
	Time (h)	16								
1		401	393	383	373	381	386	369	365	357
2		108	407	375	364	368	372	358	377	359
3		102	392	397	365	368	369	356	370	335
4		379	432	361	366	370	386	334	346	343
5		392	435	364	372	367	393	366	351	359
Average		**396.4**	**411.8**	**376**	**368**	**370.8**	**381.2**	**356.6**	**361.8**	**347.8**
Standard Deviation		*11.28*	*20.71*	*14.66*	*4.18*	*5.81*	*10.23*	*13.74*	*12.99*	*10.99*

The optimum solution heat treatment temperature and time were selected as 1000°C and 4 hours with Test Level S. The solution heat treatment temperature and time were fixed and continued with Test Level A, while the 1000°C 4-hour solution heat treatment remained fixed, the aging parameters are tried at different temperatures and times. The aging parameters of 4-16-64 hours for 500-550-600°C and 16 hours for 400-450-650-700°C were selected for this level. The hardness values of 4-16-64 hours for 500-550-600°C are given in *Table 4.4*.

Based on the values presented in *Table 4.4*, the hardness measurements after aging at 500°C were recorded as follows: 378.2 HB after 4 hours, 378.8 HB after 16 hours, and 365.8 HB after 64 hours. For aging at 550°C, the hardness values were measured at 359.2 HB after 4 hours, 368.0 HB after 16 hours, and 351.2 HB after 64 hours. Lastly, for aging at 600°C, the hardness measurements were 328.2 HB after 4 hours, 328.2 HB after 16 hours, and 331.2 HB after 64 hours.

Table 4.4 Brinell hardness values of the samples aged at 500, 550 and 600°C for 4-16-64 hours after 4 hours of solutionizing at 1000°C

ST	**Temperature**	**1000°C**								
	Time (h)	**4**								
	Hardness (HB)	**212.6**								
AGING	**Temperature**	**500°C**			**550°C**			**600°C**		
	Time (h)	**4**	**16**	**64**	**4**	**16**	**64**	**4**	**16**	**64**
1		377	383	359	362	373	350	333	320	330
2		379	385	374	362	364	347	329	339	339
3		381	375	370	354	365	358	329	326	330
4		377	369	357	358	366	345	324	328	327
5		377	382	369	360	372	356	326	328	330
Average		**378.2**	**378.8**	**365.8**	**359.2**	**368**	**351.2**	**328.2**	**328.2**	**331.2**
Standard Deviation		*1.79*	*6.65*	*7.40*	*3.35*	*4.18*	*5.63*	*3.42*	*7.93*	*4.55*

The hardness values after aging at 400-450-500-550-600-650-700°C for a fixed time of 16 hours are given in *Table 4.5*. The hardness results were measured as 214.6 HB for 400°C, 314.8 HB for 450°C, 378.8 HB for 500°C, 368 HB for 550°C, 328.2 HB for 600°C, 308.6 HB for 650°C, and 266.8 HB for 700°C. After aging heat treatments with a temperature increase of 50°C between 400-700°C, the highest hardness was observed at 500°C. In addition to these results, the hardness average of aging at 400°C for one week to see the effect of low-temperature long aging was measured as 245.2 HB (Standard Deviation: 5.22).

Table 4.5 Brinell hardness values of the samples after 4 hours of solutionizing at 1000°C followed by aging at 400, 450, 500, 550, 600, 650 and 700°C for 16 hours

ST	**Temperature**	**1000°C**						
	Time (h)	**4**						
	Hardness (HB)	**212.6**						
AGING	**Temperature**	**400**	**450**	**500**	**550**	**600**	**650**	**700**
	Time (h)	**16**	**16**	**16**	**16**	**16**	**16**	**16**
1		206	315	383	373	320	310	273
2		220	313	385	364	339	300	264
3		222	319	375	365	326	312	270
4		214	317	369	366	328	311	264
5		211	310	382	372	328	310	263
Average		**214.6**	**314.8**	**378.8**	**368**	**328.2**	**308.6**	**266.8**
Standard Deviation		*6.54*	*3.49*	*6.65*	*4.18*	*7.93*	*4.88*	*4.44*

4.3. Microstructural Examinations

4.3.1. As Cast Sample

A representative optical image showing the microstructure of the as cast samples is given in *Figure 4.2*. The as-cast microstructure image shows austenite grains and α + κ-carbide colonies at grain boundaries.

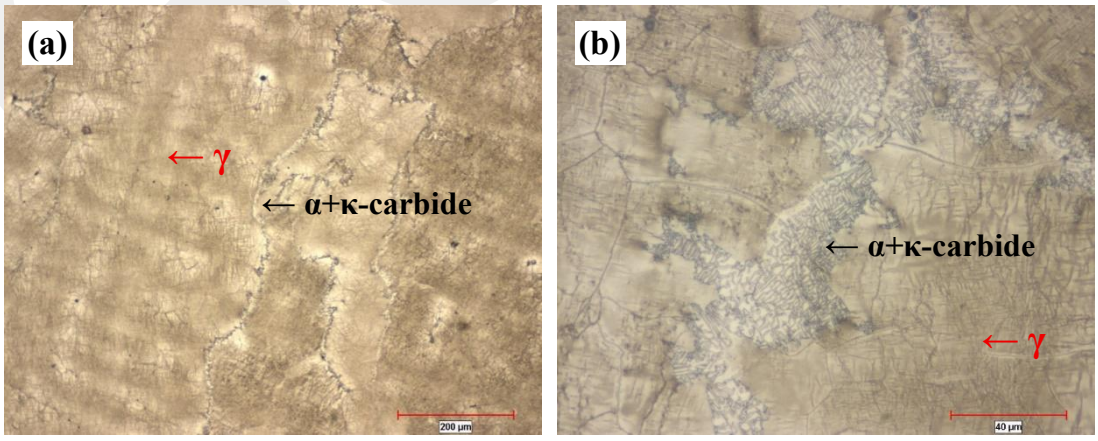

Figure 4.2 The as-cast microstructure (a) 100X (b) 500X, etched with %10 Nital

4.3.2. Solutionized Samples

Figure 4.3 shows the microstructures of sample solution heat treated at 950°C for (a) 2 hours, (b) 4 hours, and (c) 16 hours. Austenite grains and grain boundaries are clearly seen in all microstructures after solution heat treatment at different times. Again, for all different times, the microstructures are heterogeneous, and grain sizes vary between 200-400 µm.

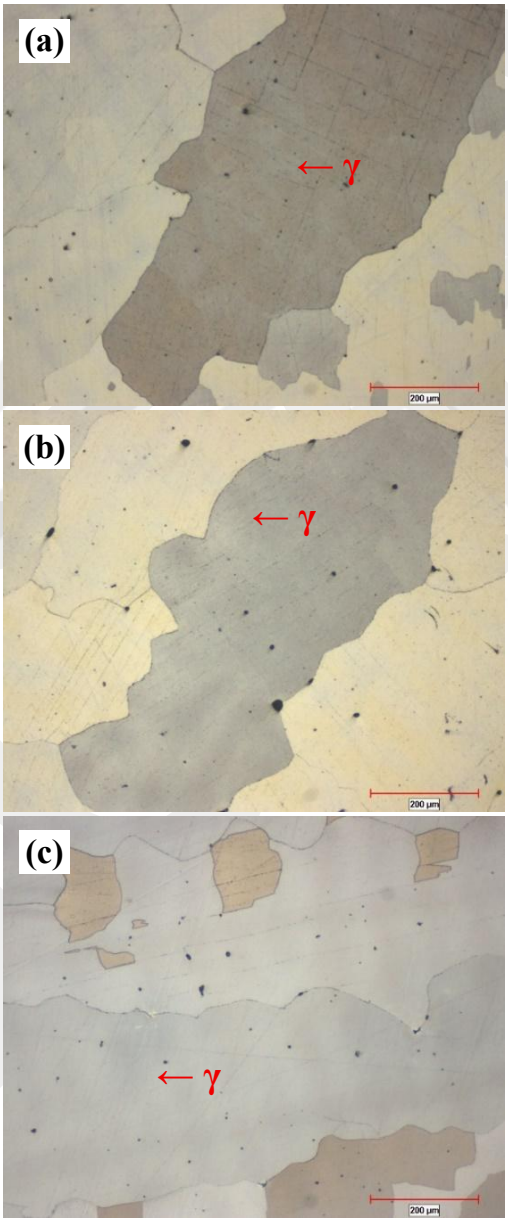

Figure 4.3 Optical microstructural images of the samples solutionized at 950°C for (a) 2h, (b) 4h and (c) 16h. Samples were quenched into water 25°C after solutionizing (100X, Viella etched)

Figure 4.4 shows the microstructure of the sample subject to solution heat treatment at 1000°C for 4 hours. In the image, austenite grains and grain boundaries are visible. For the relevant temperature and time, the microstructures are heterogeneous, and grain sizes vary between 200 and 400 µm.

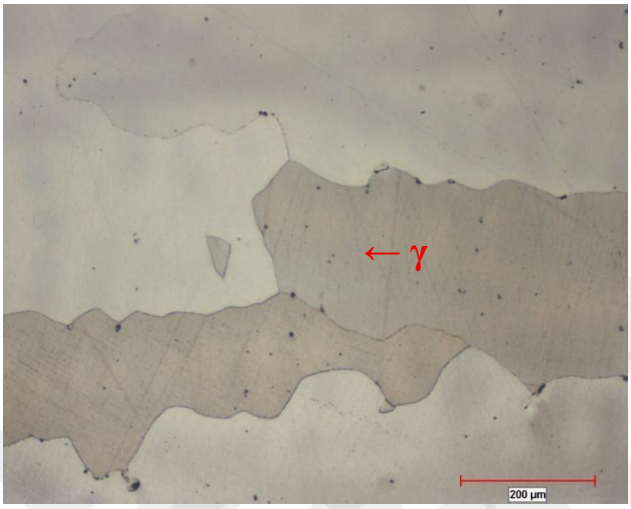

Figure 4.4 Optical microstructural image of the sample that was solutionized at 1000°C for 4 hours followed by quenching in water at 25°C (100X, Viella etched)

Solution heat treatments at 1050°C are shown in *Figure 4.5*. Two different times were tested (a) after 2 hours and (b) after 4 hours, showing the microstructures. While a heterogeneous grain distribution is seen in both microstructures, austenite grains and grain boundaries are clearly seen. Grain sizes vary between 200-400 µm.

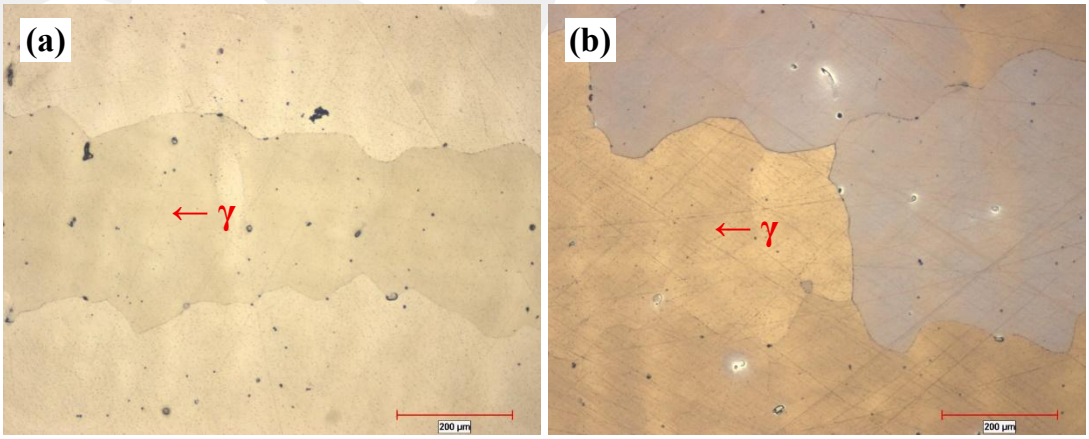

Figure 4.5 Optical microstructural images of the samples that were solutionized at 1050°C for (a) 2h and (b) 4h. Samples were quenched into water 25°C after solutionizing (100X, Viella etched)

The last tested solution heat treatment was carried out at 1150°C for two different times. *Figure 4.6* shows the microstructures after the solution treatment at the relevant temperature (a) 2 hours and (b) 4 hours. Austenite grains, grain boundaries, and annealing twins were observed in both microstructures. Ferrite was observed in the microstructure only after 4 hours of solution treatment.

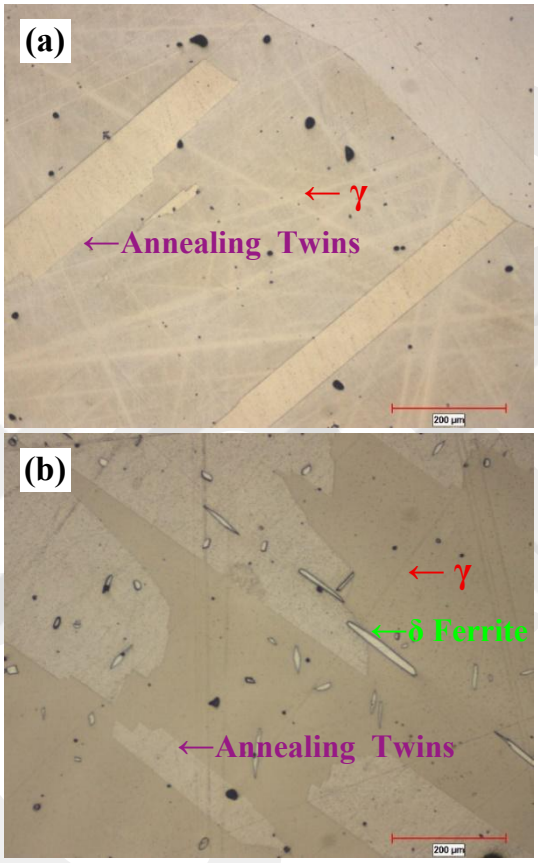

Figure 4.6 Optical microstructural images of the samples were solutionized at 1150°C for (a) 2h and (b) 4h. Samples were quenched into water at 25°C after solutionizing (100X, Viella etched)

4.3.3. Aged Samples

To make the microstructural images after aging more understandable, they are given in the order specified in the heading *"3.4. Heat Treatments"*. First, the microstructure images of the Test Level S, and then the Test Level A samples are given.

- *Test Level S* = **Different Solution Heat Treatment** + Fixed Aging
- *Test Level A* = Fixed Solution Heat Treatment + **Different Aging**

Figure 4.7 shows the microstructure images after solution heat treatment at 950°C for 2, 4, and 16 hours and aging at 550°C for 16 hours (Test Level S). Austenite grains, grain boundaries, and κ-carbides precipitates formed on grain boundaries were observed in all microstructures.

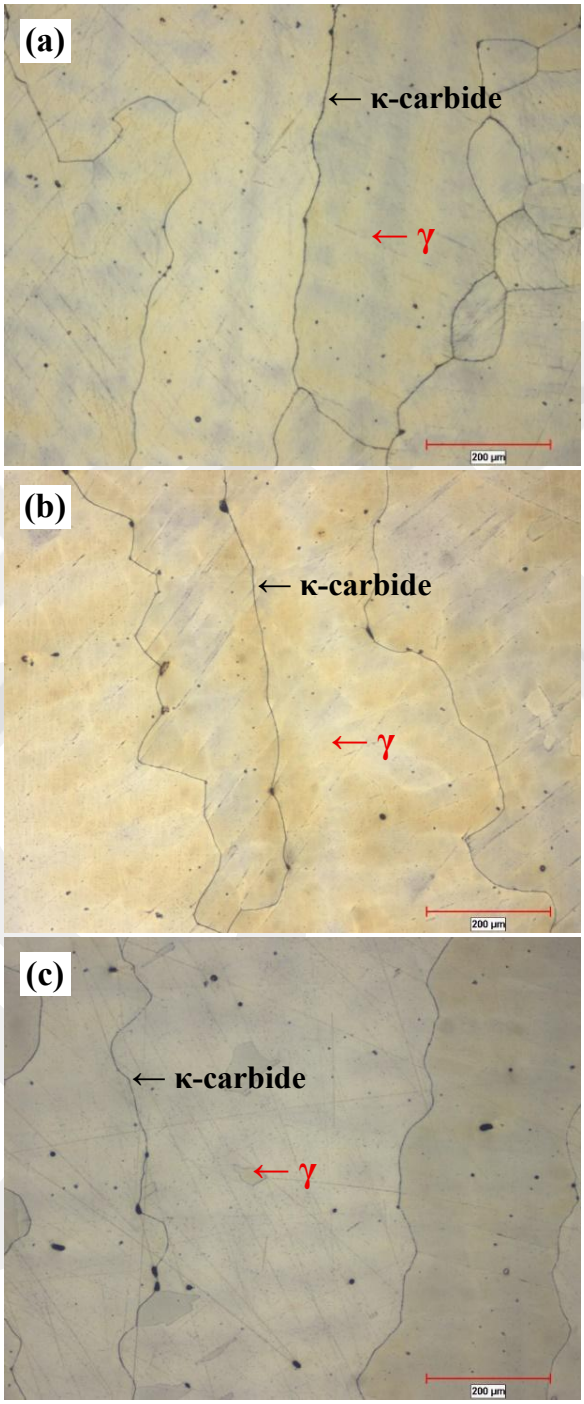

Figure 4.7 Optical microstructural images of the samples that were solutionized at 950°C for (a) 2h, (b) 4h and (c) 16h followed by aging at 550°C for 16 hours, etched with Vilella (100X)

Figure 4.8 shows the microstructure images after solution heat treatment at 1050°C for 2 and 4 hours and aging at 550°C for 16 hours (Test Level S). Austenite grains, grain boundaries, and κ-carbides precipitates formed on grain boundaries were observed in all microstructures.

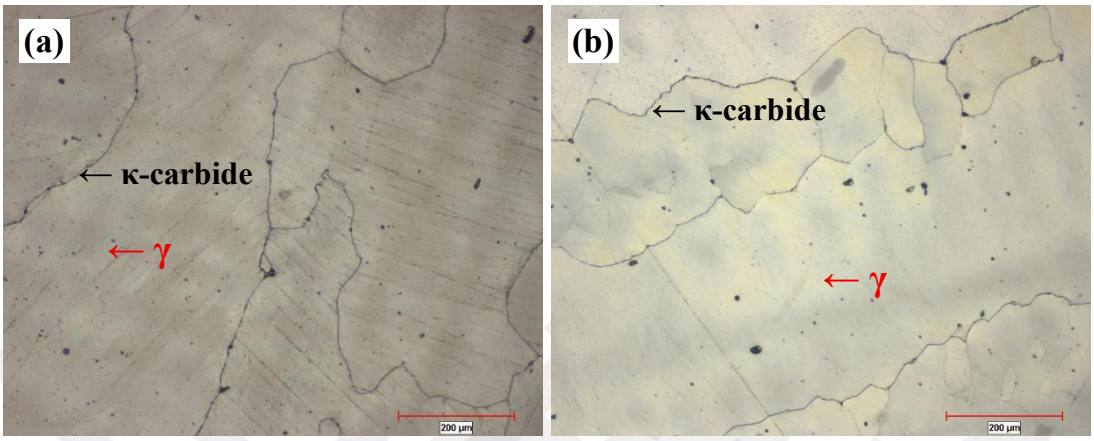

Figure 4.8 Optical microstructural images of the samples that were solutionized at 1050°C for (a) 2h and (b) 4h followed by aging at 550°C for 16 hours, etched with Vilella (100X)

Figure 4.9 shows the microstructure images after solution heat treatment at 1150°C for 2 and 4 hours and aging at 550°C for 16 hours (Test Level S). Austenite grains, grain boundaries, and κ-carbides precipitates formed on grain boundaries were observed in all microstructures.

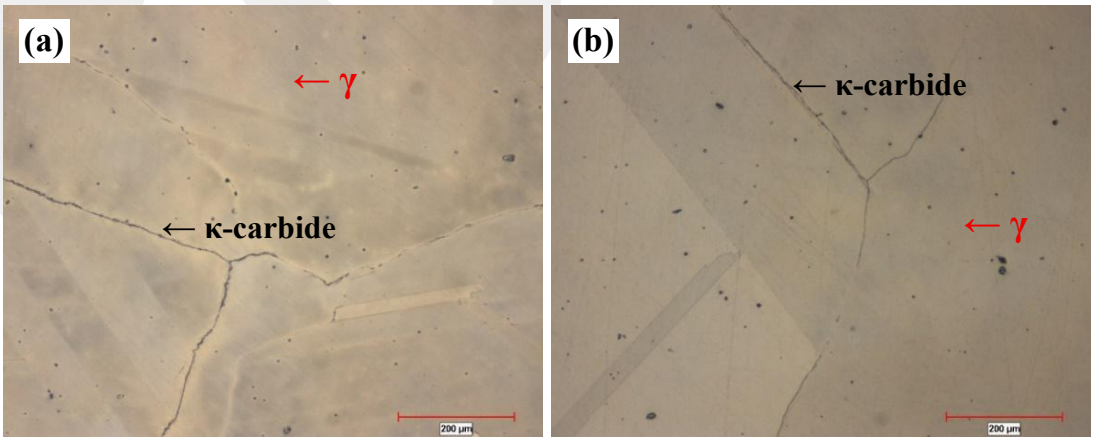

Figure 4.9 Optical microstructural images of the samples that were solutionized at 1150°C for (a) 2h and (b) 4h followed by aging at 550°C for 16 hours, etched with Vilella (100X)

Figure 4.10 (a) shows the microstructure of the sample aged at 400°C for 16 hours, and (b) shows the microstructure of the sample aged at 400°C for 1 week (Test Level A). Austenite grains and grain boundaries, as well as κ-carbides precipitates formed at the grain boundaries, are visible in both samples.

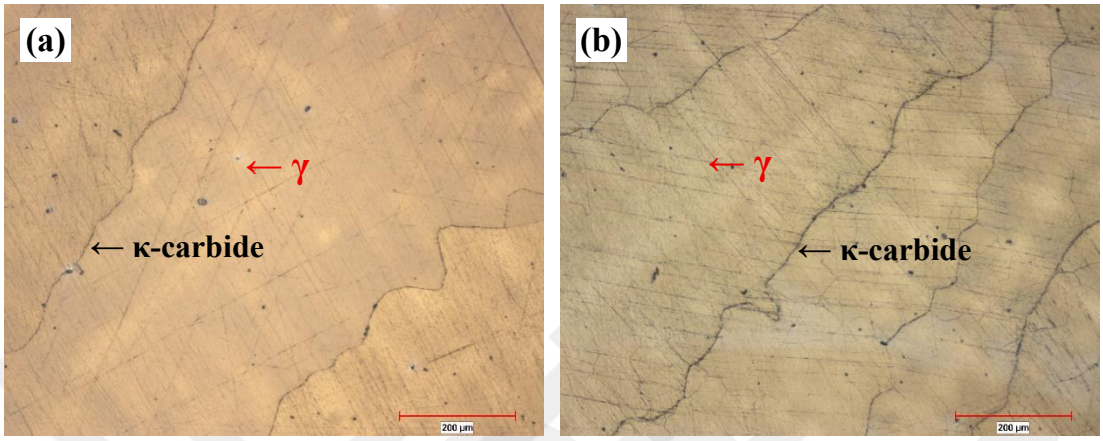

Figure 4.10 Optical microstructural images of the samples that were solutionized at 1000°C for 4 hours followed by aging at 400°C for (a)16h and (b) 1 week, etched with Vilella (100X)

Figure 4.11 shows the microstructural image after aging for 16 hours at 450°C. Austenite grains, grain boundaries and κ-carbides formed on the boundaries are visible in the microstructure.

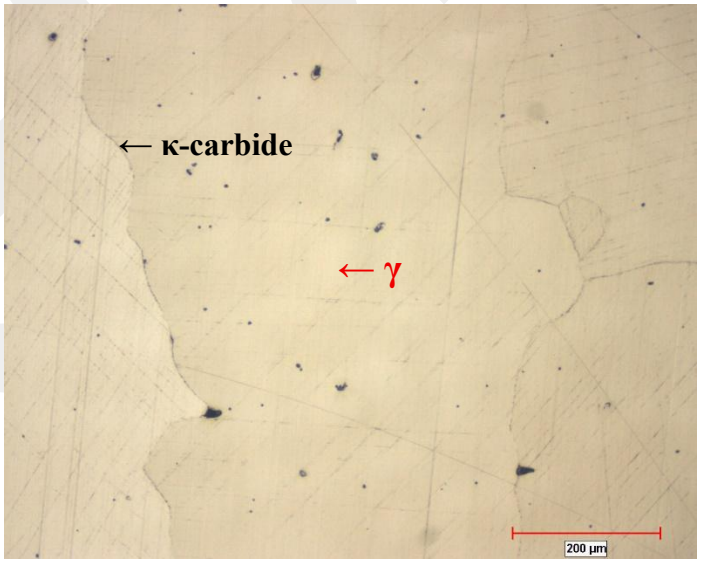

Figure 4.11 Optical microstructure images of the samples that were solutionized at 1000°C for 4 hours followed by aging at 450°C for 16h, etched with Vilella (100X)

Figure 4.12 shows the microstructures of the samples aged at 500°C for (a) 4 hours, (b) 16 hours, and (c) 64 hours after solution heat treatment at 1000°C for 4 hours (Test Level A). κ-carbides formation was observed at the austenite grain boundary in all microstructures. α + κ-carbide formation was observed only in the 64-hour sample.

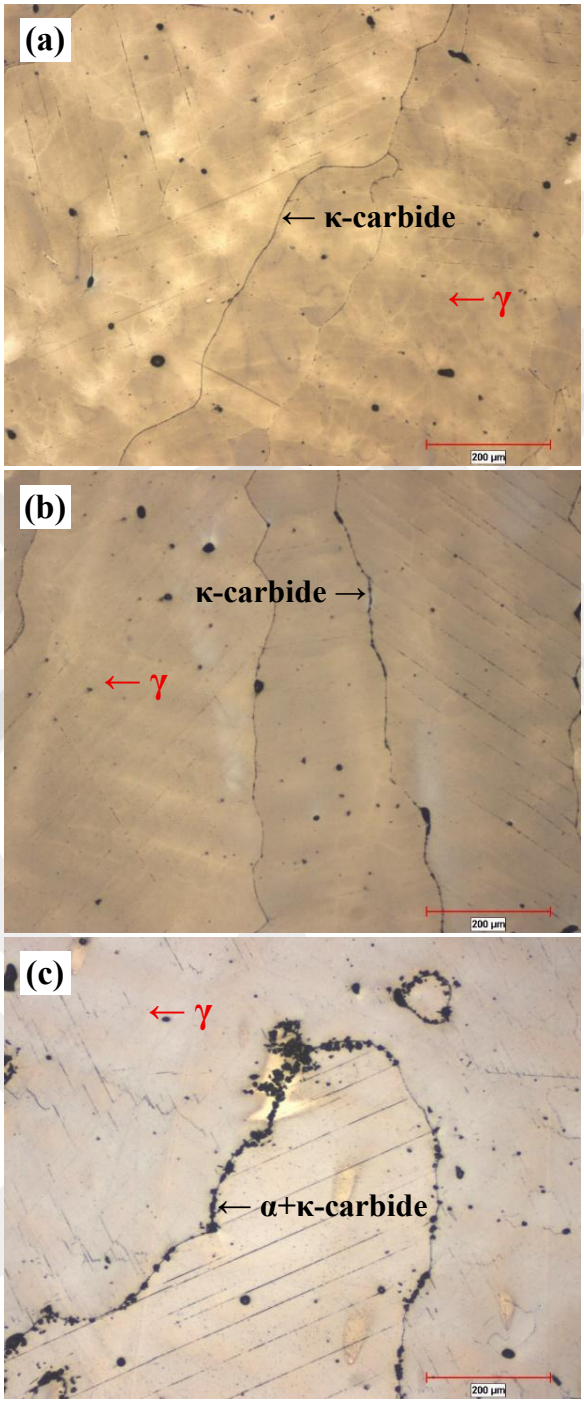

Figure 4.12 Optical microstructural images of the samples that were solutionized at 1000°C for 4 hours followed by aging at 500°C for (a) 4h, (b) 16h and (c) 64h, etched with Vilella (100X)

Figure 4.13 shows the microstructures of the samples aged at 550°C for (a) 4 hours, (b) 16 hours, and (c) 64 hours after solution heat treatment at 1000°C for 4 hours (Test Level A). κ-carbides formation was observed at the austenite grain boundary in all microstructures. α + κ-carbide formation was observed only in the 64-hour sample.

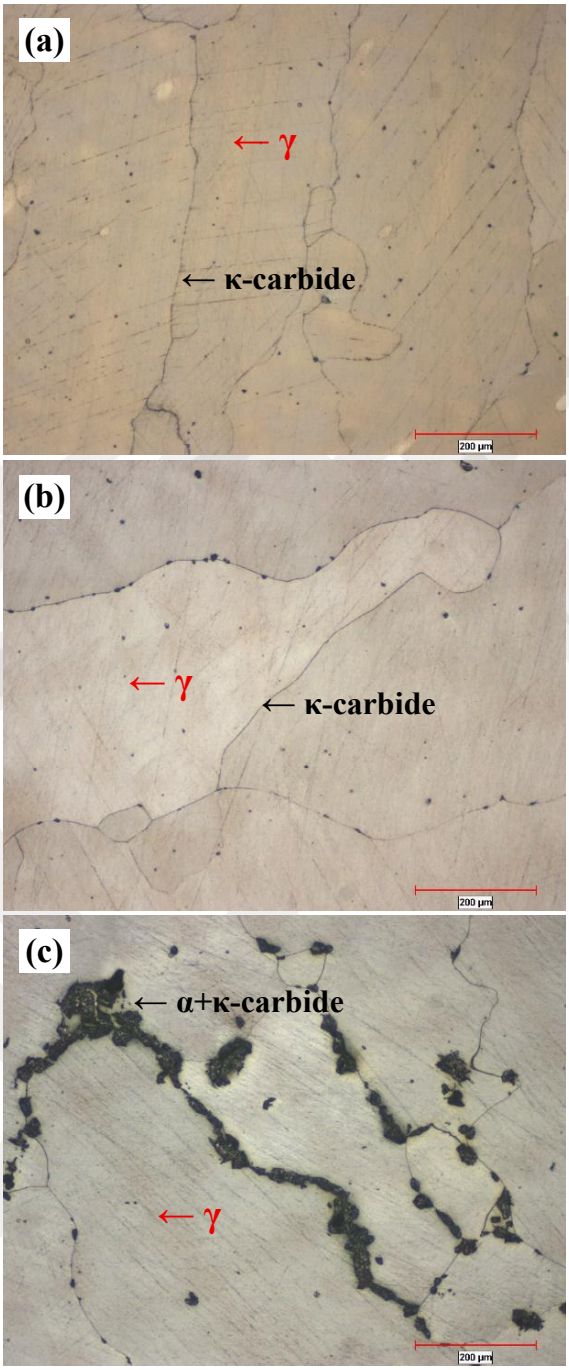

Figure 4.13 Optical microstructural images of the samples that were solutionized at 1000°C for 4 hours followed by aging at 550°C for (a) 4h, (b) 16h and (c) 64h, etched with Vilella (100X)

Figure 4.14 shows the microstructures of the samples aged at 600°C for (a) 4 hours, (b) 16 hours, and (c) 64 hours after solution heat treatment at 1000°C for 4 hours (Test Level A). κ-carbides formation was observed at the austenite grain boundary in all microstructures. α + κ-carbide formation was observed only in the 64-hour sample.

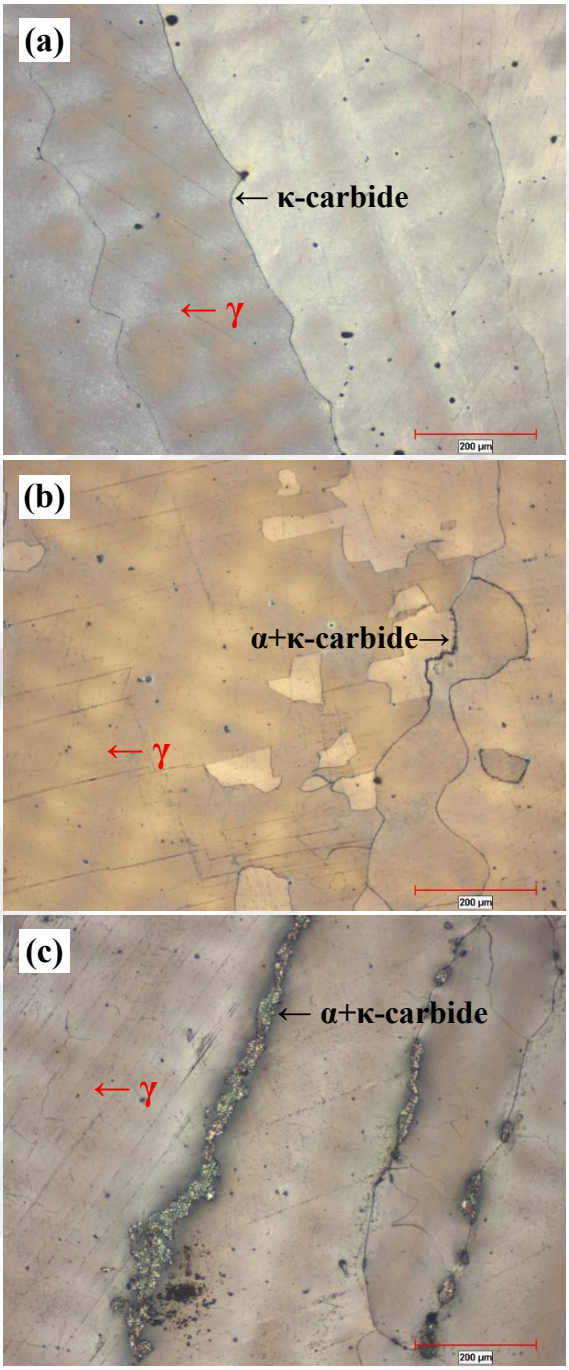

Figure 4.14 Optical microstructural images of the samples that were solutionized at 1000°C for 4 hours followed by aging at 600°C for (a) 4h, (b) 16h and (c) 64h, etched with Vilella (100X)

Figure 4.15 shows the microstructure image after aging at 650°C for 16 hours. Austenite grains and grain boundaries are visible. In addition, κ-carbide precipitates formed at grain boundaries are clearly visible.

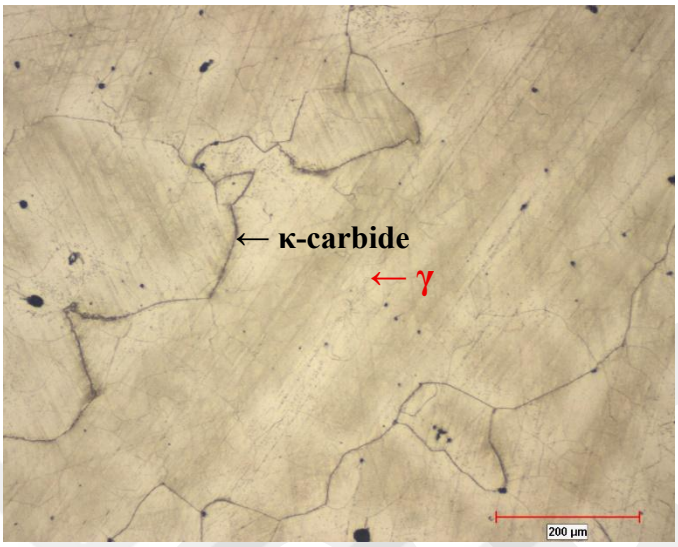

Figure 4.15 Optical microstructural images of the samples that were solutionized at 1000°C for 4 hours followed by aging at 650°C for 16h, etched with Vilella (100X)

Finally, the microstructure of the sample subjected to 700°C 16 hours of aging treatment is shown in *Figure 4.16*. Austenite grains and grain boundaries are clear, and α + κ-carbide structures are observed on the grain boundaries.

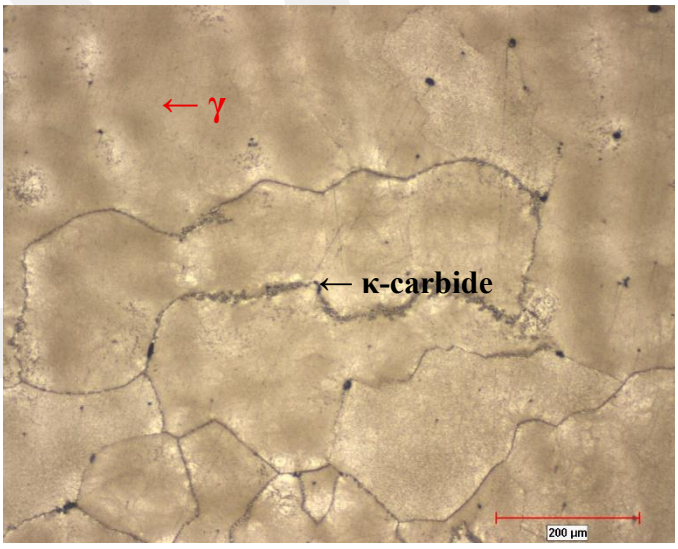

Figure 4.16 Optical microstructural images of the samples that were solutionized at 1000°C for 4 hours followed by aging at 700°C for 16h, etched with Vilella (100X)

4.3.4. SEM Examinations

Figure 4.17 shows the as-cast microstructure image taken with SEM. In the high magnification image taken at the grain boundary, austenite grains and α + κ-carbide structures on the grain boundaries are clearly seen.

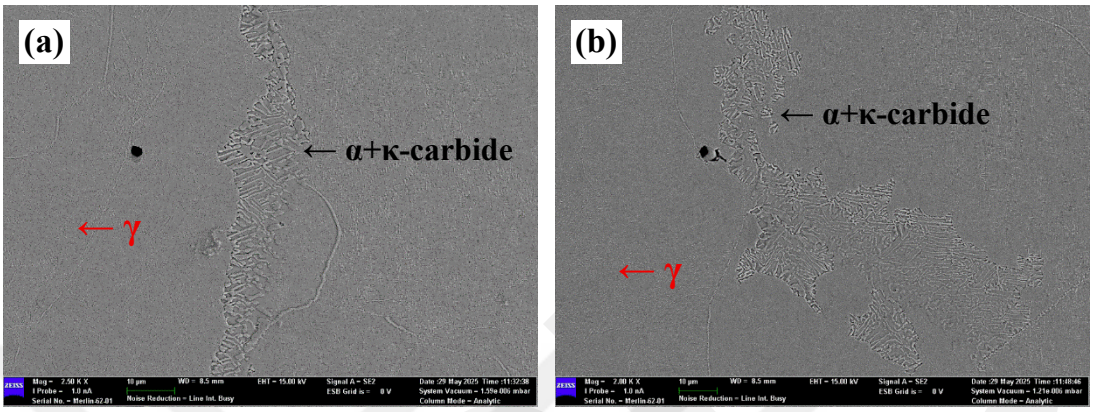

Figure 4.17 As-cast SEM image taken from two different grain boundaries

Figure 4.18 shows the result of the point EDS analysis performed on the α + κ-carbide region on the grain boundary and inside the austenite grain. The composition as a result of the EDS analysis from Spot 1 (α + κ-carbide) is 54.59%Fe, 33.92%Mn, 10.92%Al, and 0.57%Si. The composition of the EDS analysis from Spot 2 (austenite grain) is 58.46%Fe, 31.63%Mn, 8.93%Al, and 0.98%Si.

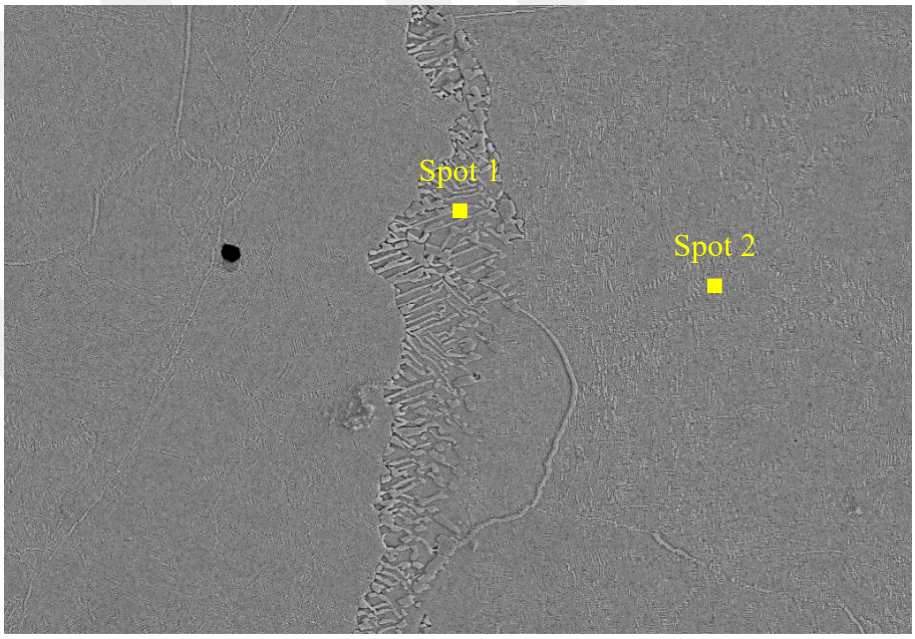

Figure 4.18 EDS spot analysis of grains and grain boundaries in as-cast microstructure

EDS spot analysis points from another region are shown in *Figure 4.19*. According to the EDS analysis from Spot 1 (α + κ-carbide), the composition is 54.68%Fe, 33.32%Mn, 10.43%Al, and 1.57%Si. The analysis results from Spot 2 (austenite grain) are measured as 59.12%Fe, 30.65%Mn, 9.3%Al, and 0.94%Si.

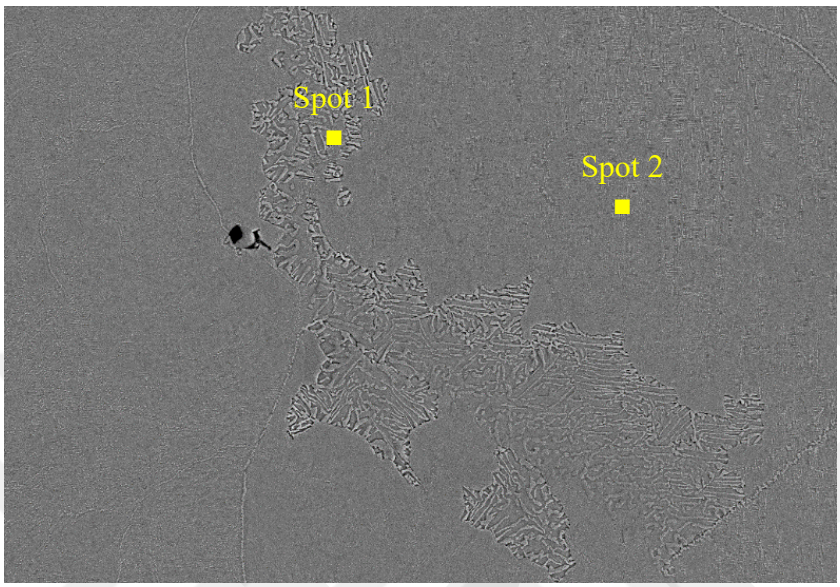

Figure 4.19 EDS spot analysis of grains and grain boundaries in as-cast microstructure

Figure 4.20 shows the EDS analysis regions made at high magnification from the α + κ-carbide region. The analysis in *Figure 4.20 (a)* was made on κ-carbide and the EDS elemental analysis results were 59.42% Fe, 31.04% Mn, 8.3% Al, and 1.24% Si. *Figure 4.20 (b)* shows the EDS analysis region made on the α, and the results were 53.57% Fe, 34.2% Mn, 11.3% Al, and 0.93% Si.

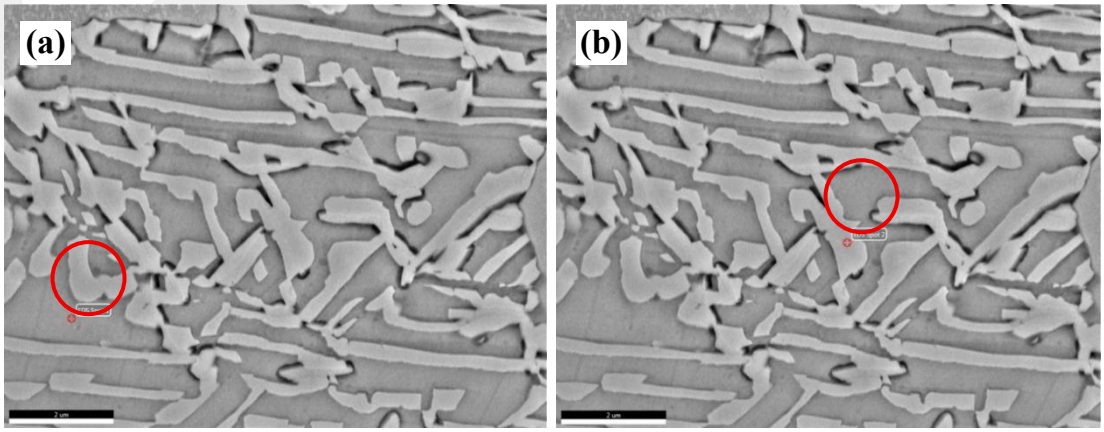

Figure 4.20 EDS point analysis of (a) κ-carbide, (b) α at the as-cast grain boundary

Figure 4.21 shows the EDS line analysis region and results. The analysis was carried out at a length of approximately ~90 µm, including both austenite grains and α + κ-carbide regions. The elemental values as a result of the EDS line analysis performed in the relevant region are 58% Fe, 31.82% Mn, 9.19% Al, and 0.99% Si.

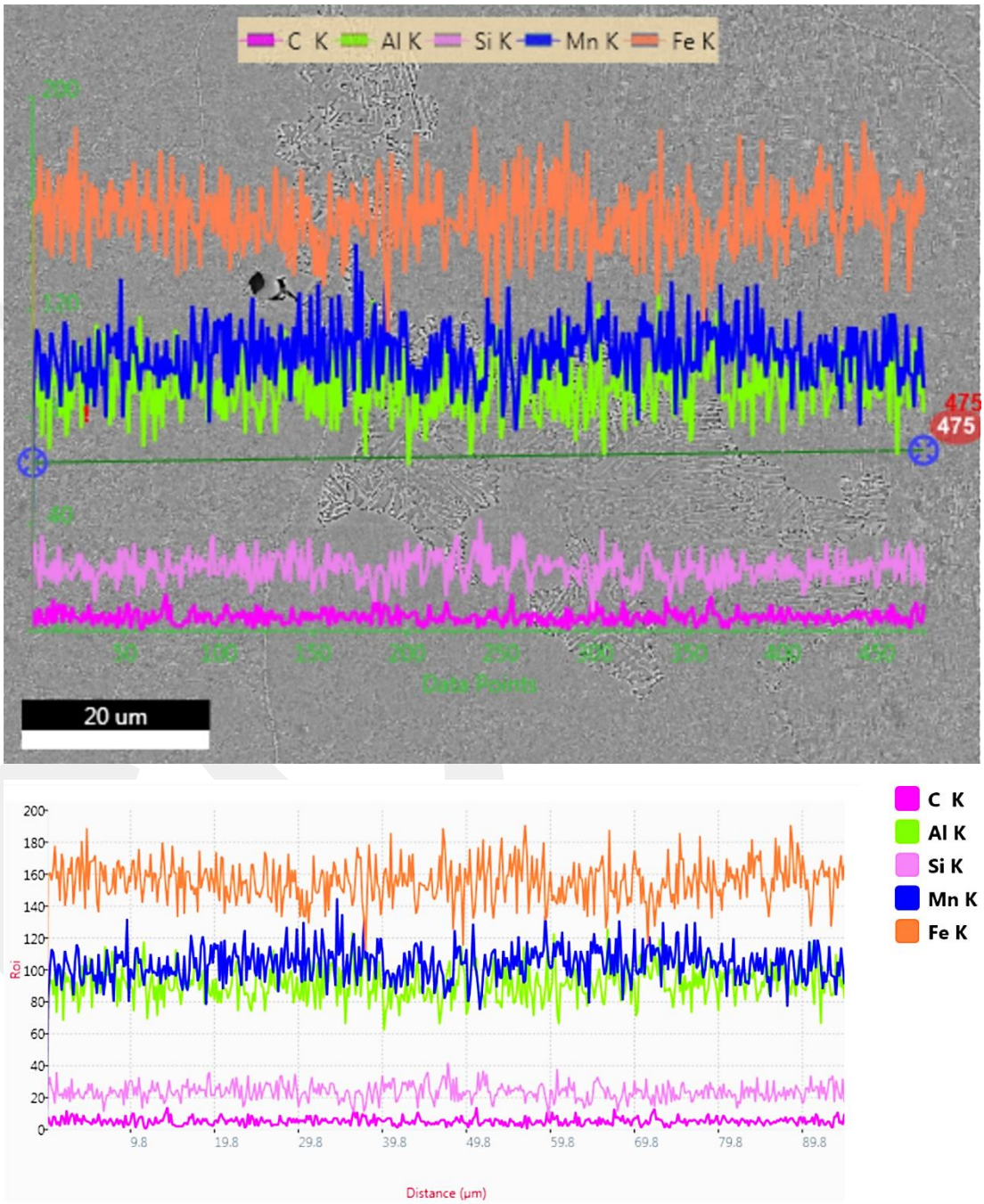

Figure 4.21 Results of the EDS line analysis for austenite grains and α + κ-carbide

The other EDS line analysis was performed to include the α + κ-carbide region, show in *Figure 4.22*. The analysis was performed on the grain boundary with a length of ~50 µm. The values of the EDS line analysis results are 58.3Fe, 31.26Mn, 9.71Al, and 0.73Si (wt%).

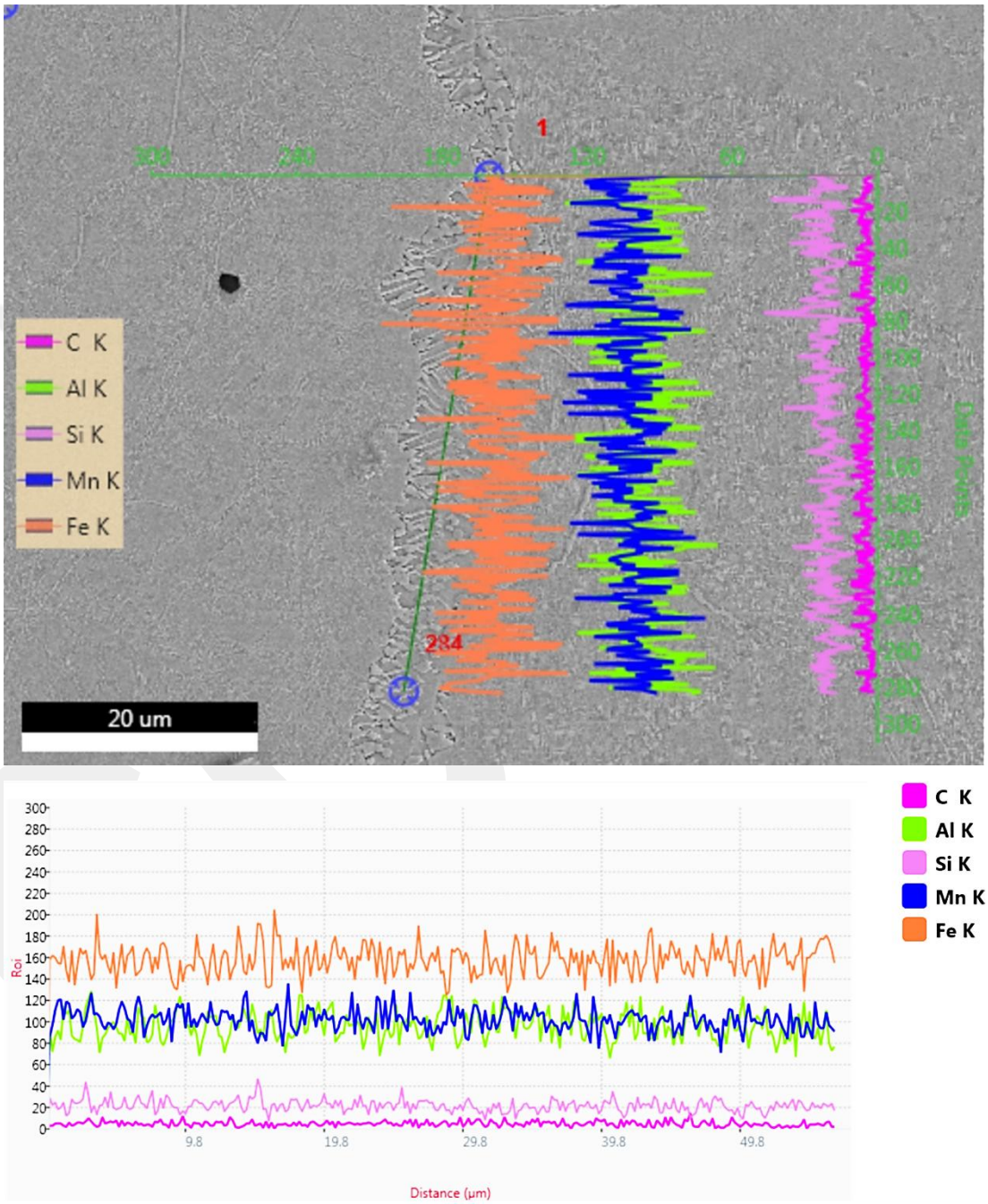

Figure 4.22 Results of the EDS line analysis for α + κ-carbide

4.3.5. EBSD Analysis

As-cast EBSD analyses were performed for two different regions. The phase map resulting from the analysis in the first region is seen in *Figure 4.23 (a)*. While 99% of grains are austenite in the analyzed area, the ferrite ratio is approximately just 1%. In addition, the average grain area was measured as 137.1 μm^2 in the grain area calculation. The second analysis result shown in *Figure 4.23 (b)* shows that 98% of the analysis area is the austenite phase while approximately 2% is the ferrite phase. The average grain area is 169.6 μm^2.

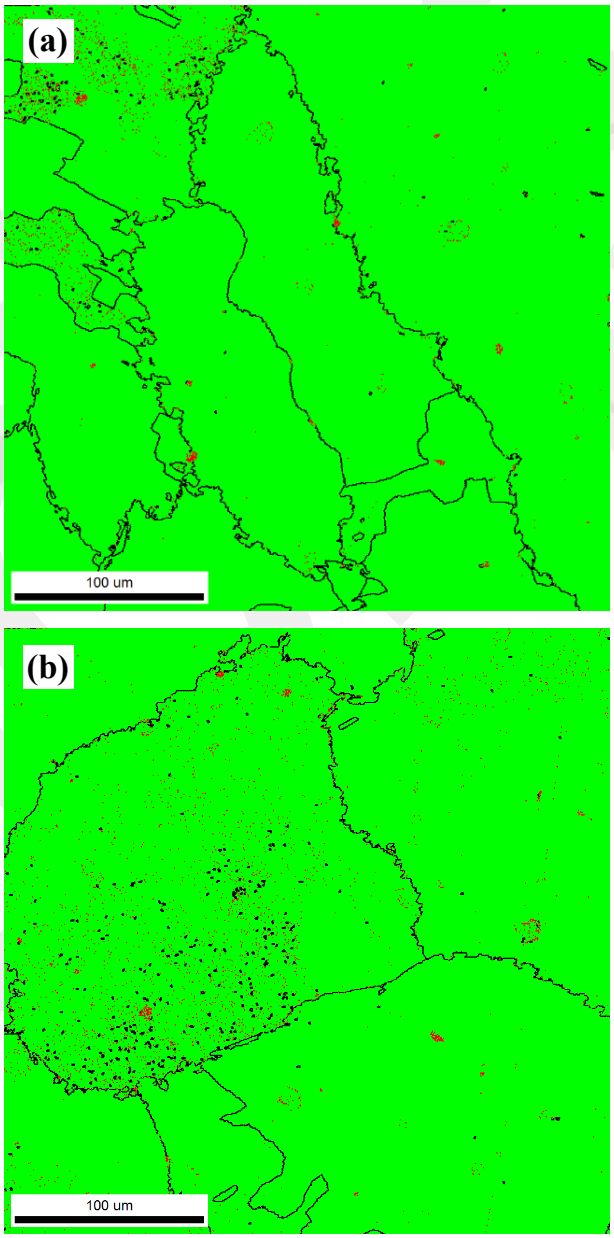

Figure 4.23 As-cast EBSD analysis from two different region; ■ Austenite, ■ Ferrite

4.3.6. ImageJ Microstructure Analysis

In *Figure 4.24* below, the phase distribution of the sample that was solution heat-treated at 1000°C for 4 hours is shown using ImageJ software [61]. The white areas represent the austenite phase, with a ratio of ~ 99.3%. The remaining black areas represent phases such as precipitates, inclusions, etc.

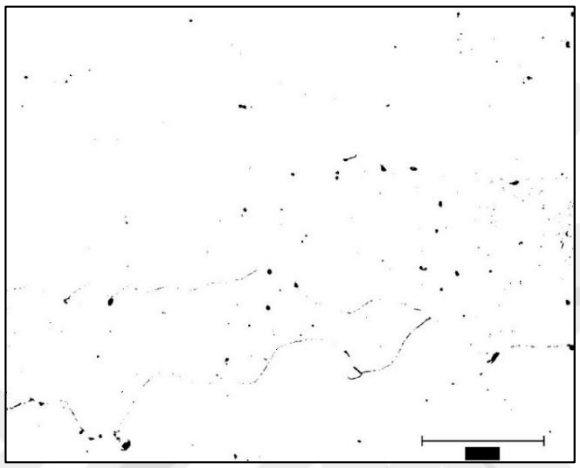

Figure 4.24 ImageJ phase analysis of sample after solution heat treatment at 1000°C for 4 hours

In *Figure 4.25* below, the phase distribution of the sample that was aged at 500°C for 4 hours after solution heat-treated at 1000°C for 4 hours is shown using ImageJ software. The white areas represent the austenite phase, with a ratio of ~ 99.1%. The remaining black areas represent phases such as precipitates, inclusions, etc.

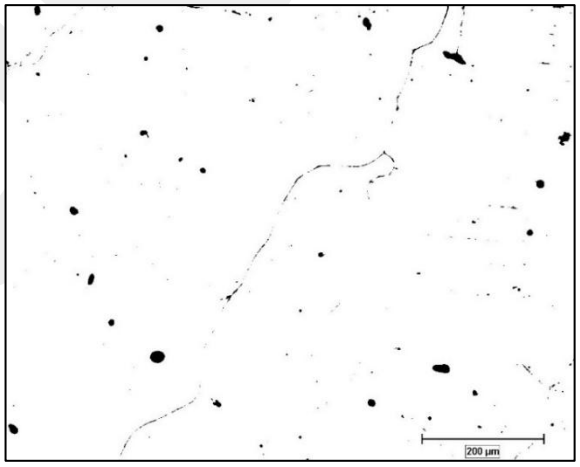

Figure 4.25 ImageJ phase analysis of the sample aged at 500°C for 4 hours after solution heat treatment at 1000°C for 4 hours

In *Figure 4.26* below, the phase distribution of the sample that was aged at 500°C for 16 hours after solution heat-treated at 1000°C for 4 hours is shown using ImageJ software. The white areas represent the austenite phase, with a ratio of ~ 98.2%. The remaining black areas represent phases such as precipitates, inclusions, etc.

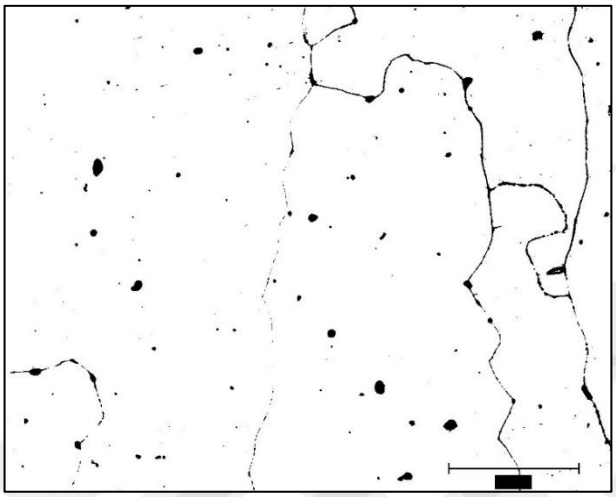

Figure 4.26 ImageJ phase analysis of the sample aged at 500°C for 16 hours after solution heat treatment at 1000°C for 4 hours

In *Figure 4.27* below, the phase distribution of the sample that was aged at 500°C for 64 hours after solution heat-treated at 1000°C for 4 hours is shown using ImageJ software. The white areas represent the austenite phase, with a ratio of ~ 96.2%. The remaining black areas represent phases such as precipitates, inclusions, etc.

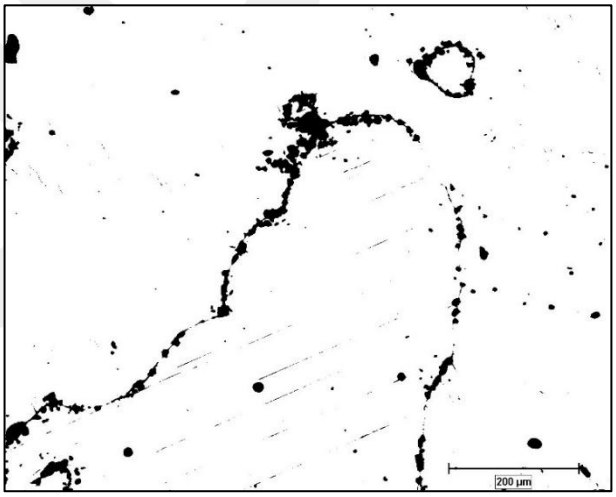

Figure 4.27 ImageJ phase analysis of the sample aged at 500°C for 64 hours after solution heat treatment at 1000°C for 4 hours

4.4. XRD Analyses

XRD pattern of the as-cast sample is given in *Figure 4.28*. Several austenite peaks of (111), (200), (220) and (311) and κ-carbide peaks of (111), (200), (220) and (311) were detected.

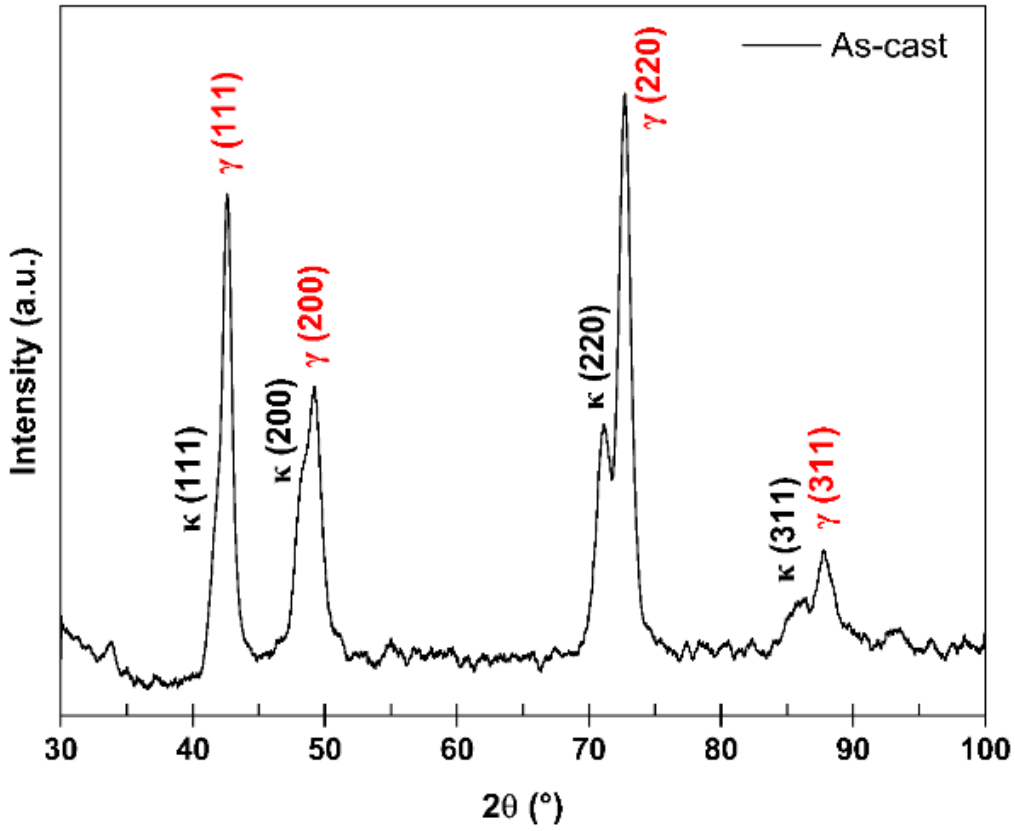

Figure 4.28 XRD pattern of the as cast sample (Cu Kα)

Figure 4.29 shows the XRD pattern after aging at 550°C for 16 hours following 2 and 4 hours of solution heat treatment at 950°C. Austenite peaks of (111), (200), and (311) and κ-carbide peak of (311) were observed in the sample that was placed in solution for 4 hours. Austenite peaks of (111), (200), (220), (311) and (222), and κ-carbide peaks of (220) and (311) were observed in the sample taken into solution for 2 hours. While (220) austenite and κ-carbides peaks were observed in the sample taken into solution for 2 hours, these peaks were not observed in the sample taken into solution for 4 hours. In addition, (222) austenite peak was observed only in the sample taken into solution for 2 hours. The intensity of the (111) austenite peak was higher in the 2-hour sample, while the intensity of the (200) peak was higher in the 4-hour sample.

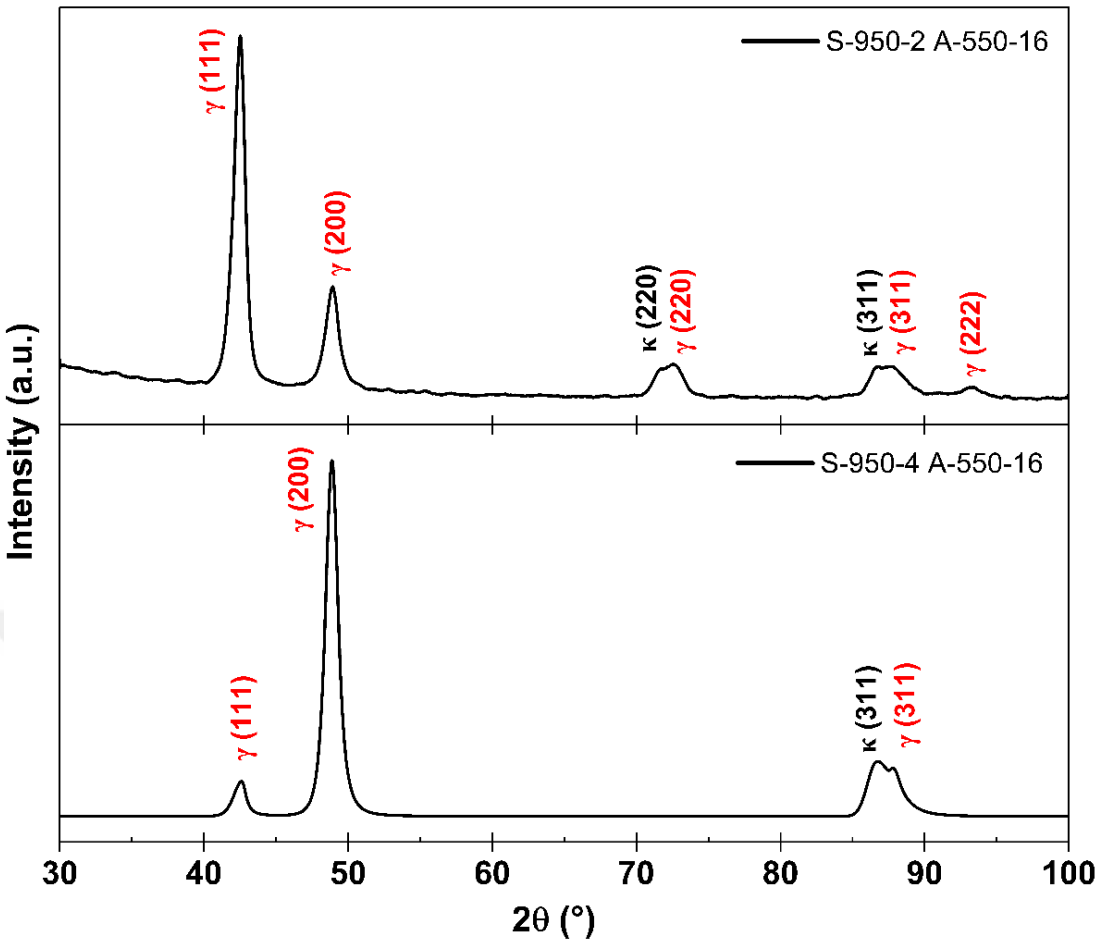

Figure 4.29 XRD pattern after solution heat treatment at 950°C for 2 and 4 hours, followed by aging at 550°C for 16 hours

Figure 4.30 shows the XRD patterns of samples that applied solution heat treatment at 1050°C for 2 and 4 hours and then aged at 550°C for 16 hours. Austenite peaks from planes (111), (200), (220) and (311) were observed in both samples and in addition, austenite peak (222) was observed in the sample applied to solution for 4 hours. κ-carbides peaks were observed as (220) and (311) for the sample taken into solution for 2 hours, while (220) and (320) were observed for the sample taken into solution for 4 hours. Among the two samples, the XRD peaks of the sample taken into solution for 4 hours are lower than those taken into solution for 2 hours.

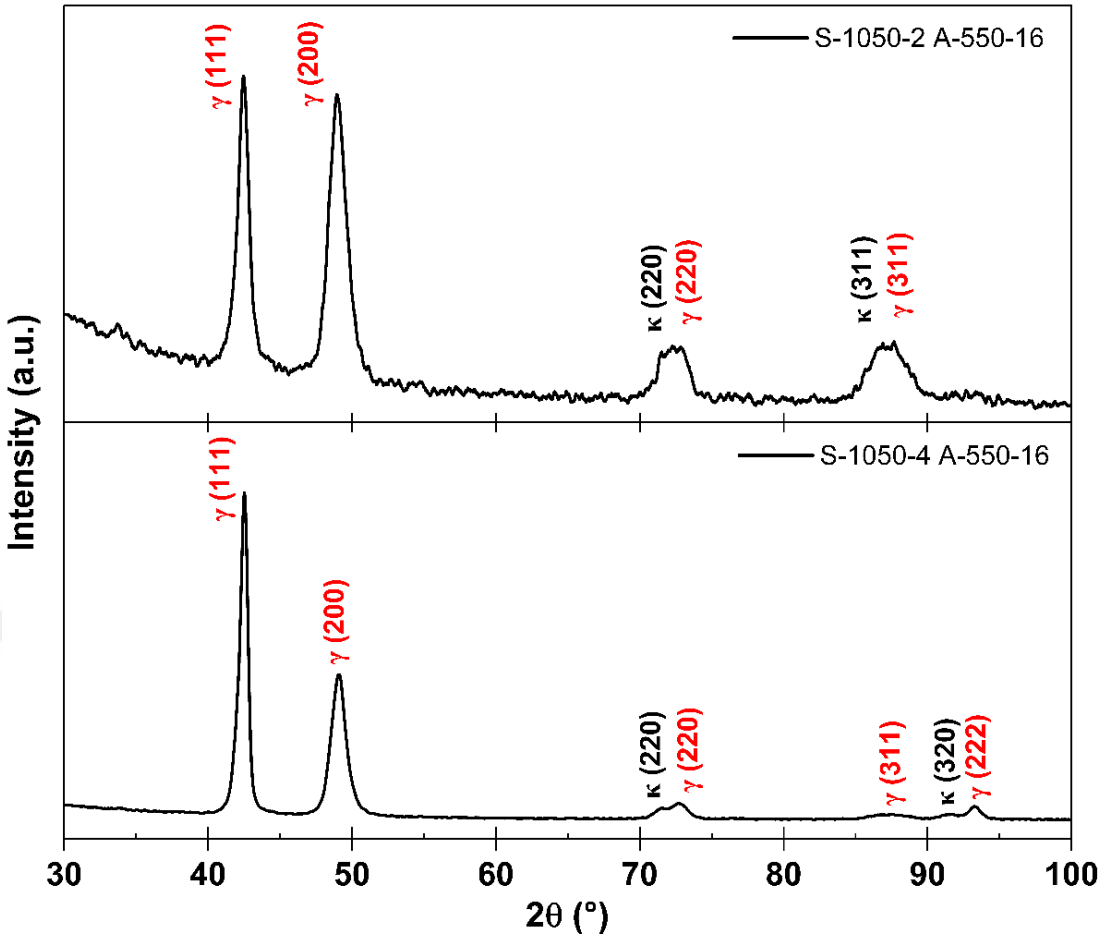

Figure 4.30 XRD pattern after solution heat treatment at 1050°C for 2 and 4 hours, followed by aging at 550°C for 16 hours

The XRD patterns of the samples that were solution heat treated at 1150°C for 2 and 4 hours and then aged at 550°C for 16 hours are shown in *Figure 4.31*. While (111), (200), and (311) austenite peaks were observed in both samples, (220) austenite peaks were observed only in the sample which was solution heat treated for 4 hours. For κ-carbide, (311) peaks were observed in the 2-hour sample, while (220) and (311) peaks were observed in the 4-hour sample. In addition, as shown in *Figure 4.32*, (110) α peak was observed in the sample which was solution treated for 4 hours. In *Figure 4.28*, 2θ in which the (110) α peak is observed, is shown in more detail.

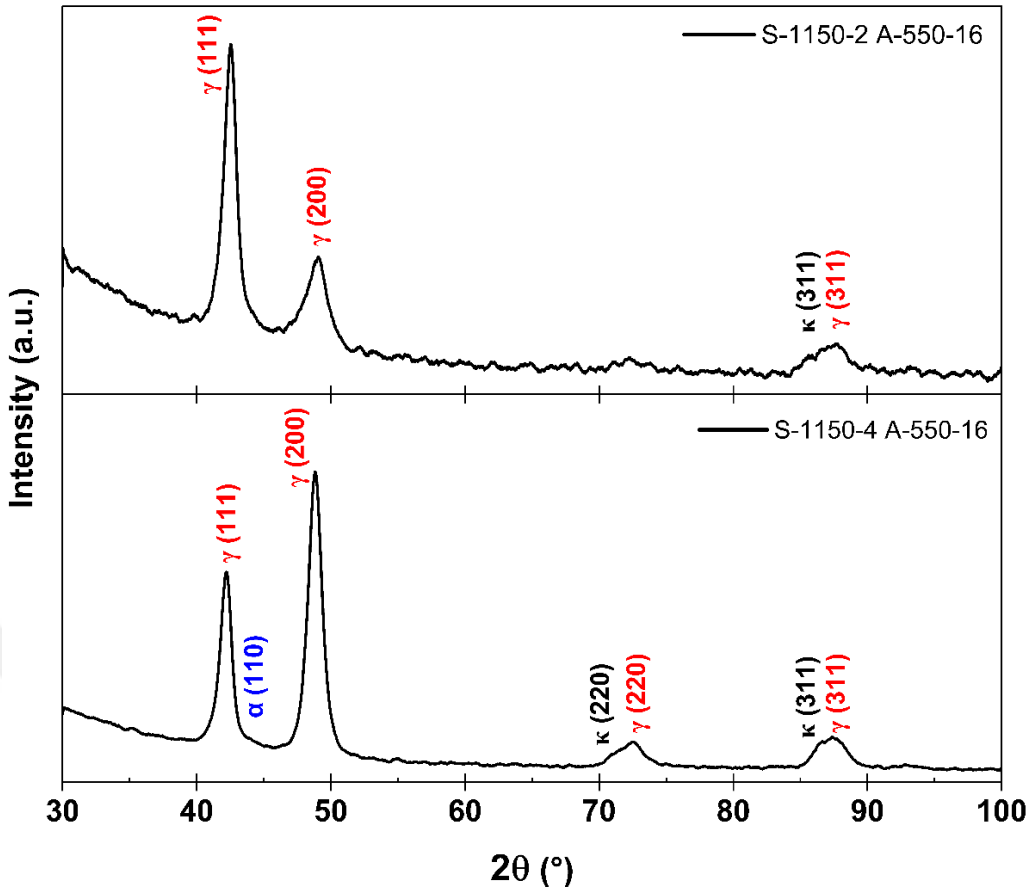

Figure 4.31 XRD pattern after solution heat treatment at 1150°C for 2 and 4 hours, followed by aging at 550°C for 16 hours

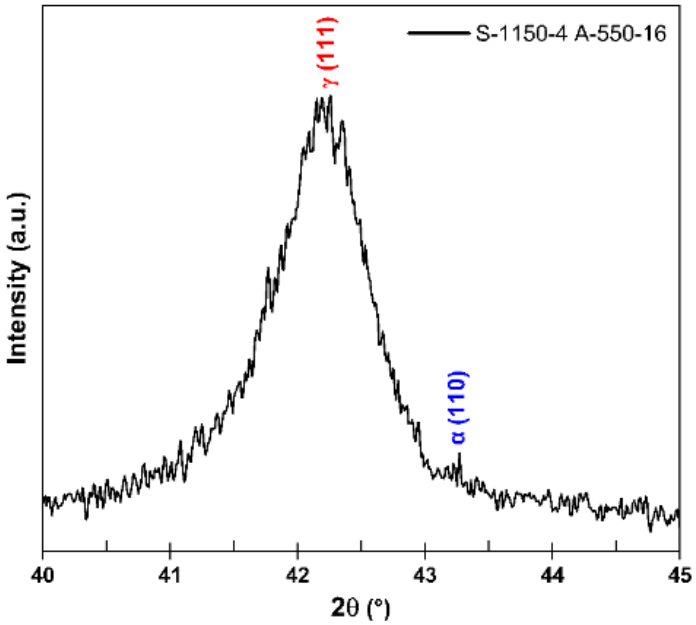

Figure 4.32 A section of the XRD pattern of the sample solutionized at 1150°C for 4 hours, followed by aging at 550°C for 16 hours

The temperature and time of the solution heat treatment selected as a result of Test Level S and used for the subsequent tests (Test Level A) are as given in the XRD result of 1000°C for 4 hours in *Figure 4.33*. After XRD analysis, austenite peaks (111), (200), (220), (311), and (222) were observed.

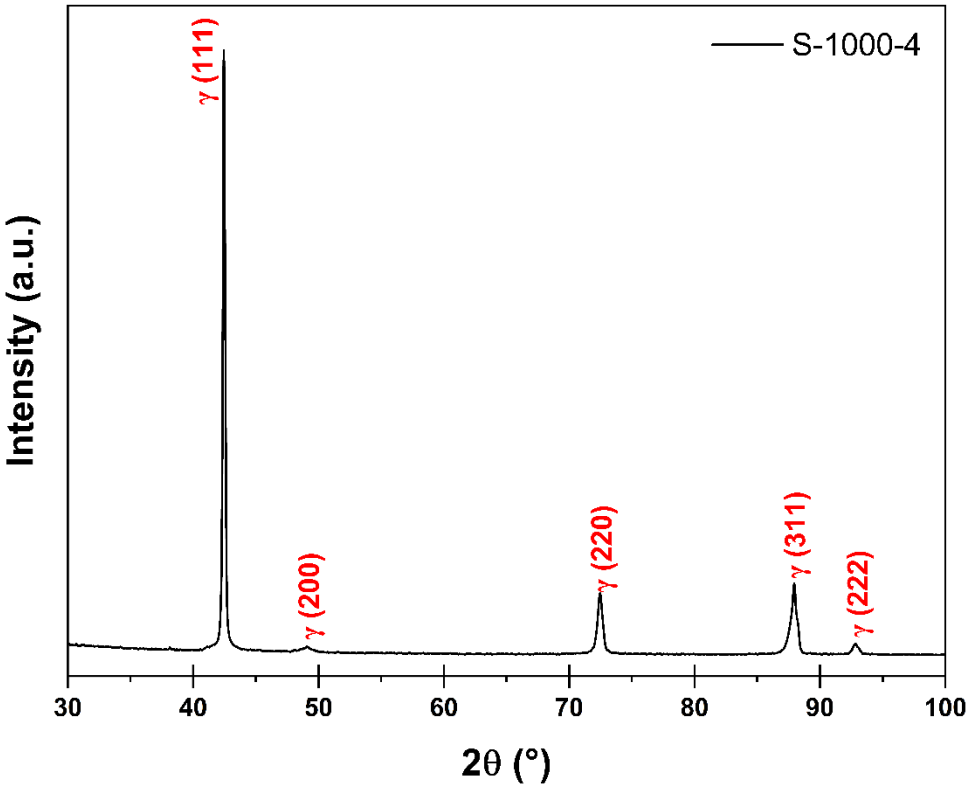

Figure 4.33 XRD pattern of the sample solution heat treated at 1050°C for 4

The first XRD result of the aging tests at different temperatures and times with the solution heat treatment (1000°C-4h) fixed for Test Level A is as shown in *Figure 4.34* for 500°C 4-16-64h. Only austenite peaks were observed in 4 and 16-hour samples. While (111),(200), and (220) austenite peaks were observed in both samples, an extra (311) peak was also observed in the 16-hour sample. No κ-carbide or α peak was observed for 4 and 16 hour samples. In the 64-hour sample, (111), (200), (220), (311), and (222) austenite peaks, (311) and (320) κ-carbide peaks were observed, but no α peak. In the aging at 500°C, κ-carbides were observed only in the 64-hour sample.

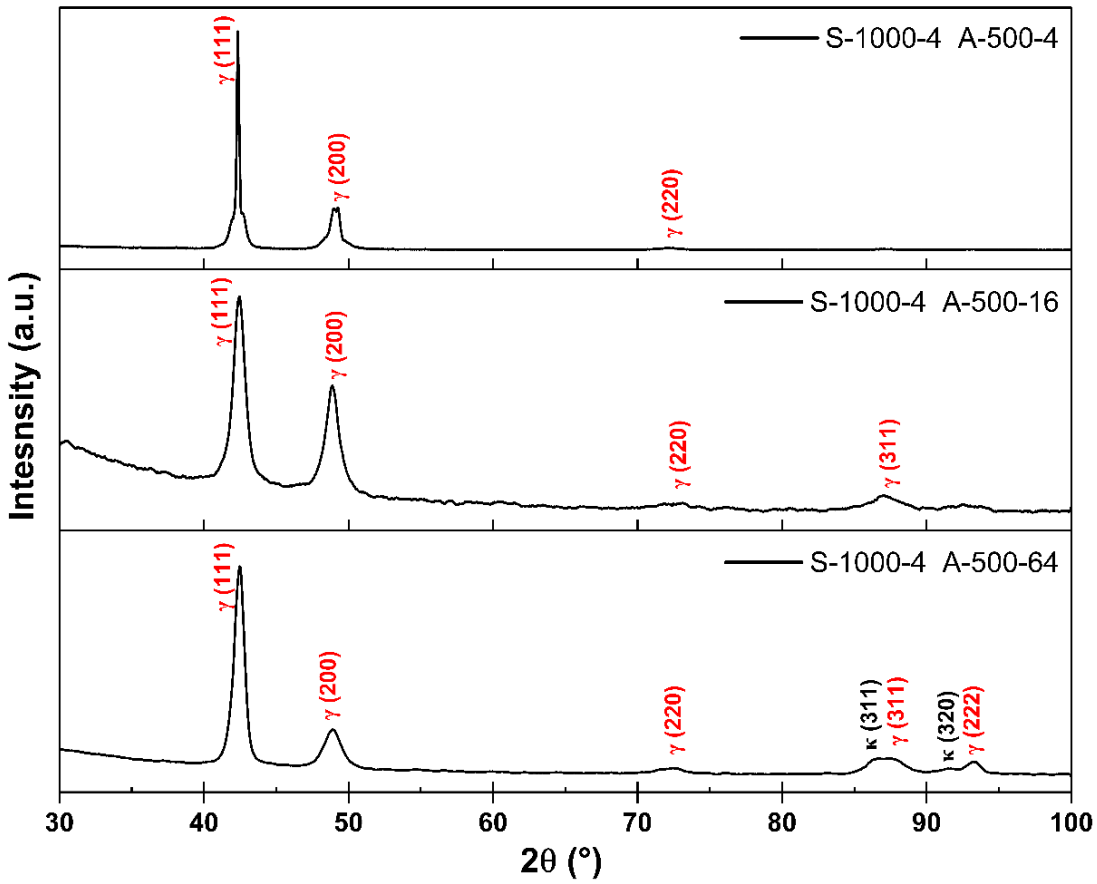

Figure 4.34 XRD pattern after solution heat treatment at 1000°C for 4 hours, followed by aging at 500°C for 4-16-64 hours

Figure 4.35 shows the XRD pattern results after 1000°C-4h solution heat treatment and aging at 550°C for 4-16-64 hours. For all aging at different times at 550°C, (111), (200), (220) and (311) austenite peaks were observed. Again, no κ-carbide peak was observed in all samples, while (110) α peak was observed only in the 64-hour sample.

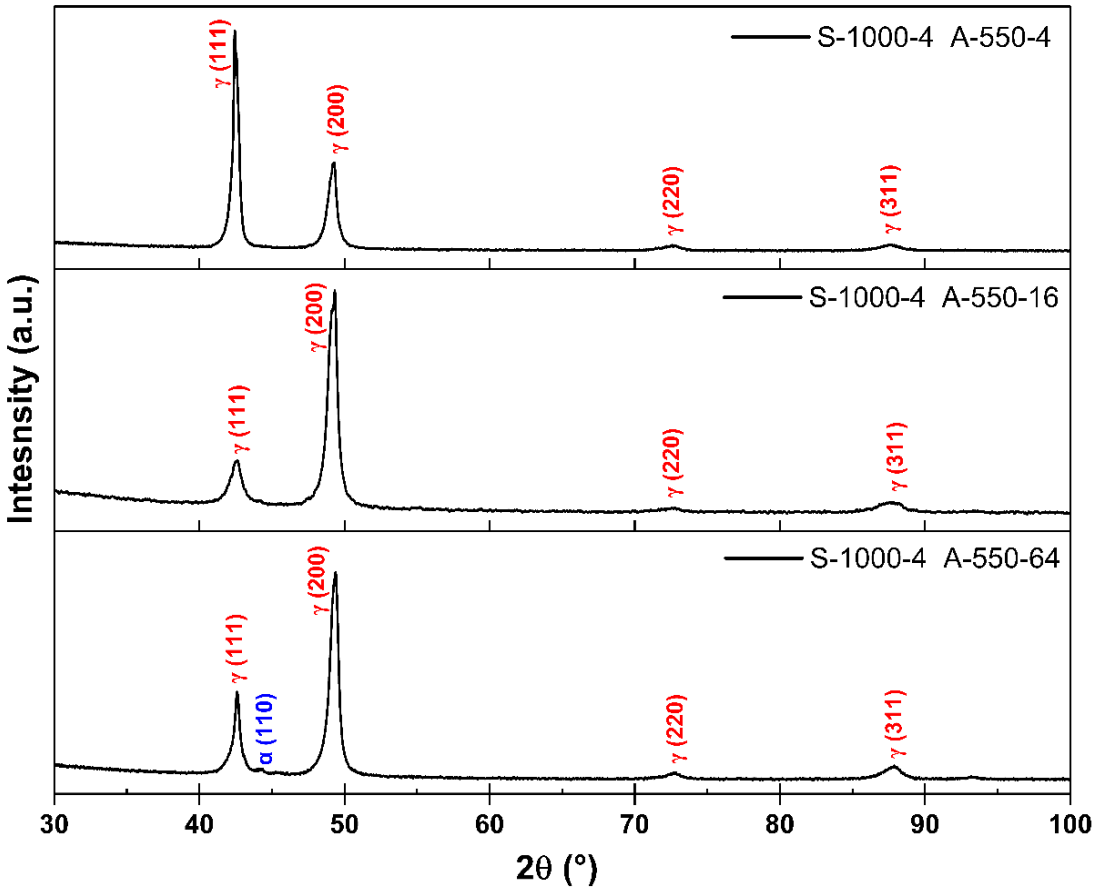

Figure 4.35 XRD pattern after solution heat treatment at 1000°C for 4 hours, followed by aging at 550°C for 4-16-64 hours

Figure 4.36 shows the XRD analysis results of aging at 600°C for 4-16-64 hours after 1000°C-4h solution heat treatment. The (111), (200), and (311) austenite peaks are seen in all samples. The (220) austenite peak was observed in the 4 and 16 hour samples, while the (222) austenite peak was observed only in the 4 hour sample. κ-carbides peaks were observed as (220) in the 4 hour sample, (111) and (220) in the 16-hour sample, and finally (111) and (311) in the 64-hour sample. While no α peak was observed in the 4 and 16-hour samples, the (110) α peak was observed in the 64-hour sample. In all different solution heat treatment and aging temperature times, only the (100) B_2 (Ordered BCC, FeAl) phase was observed in the sample aged at 600°C for 64 hours.

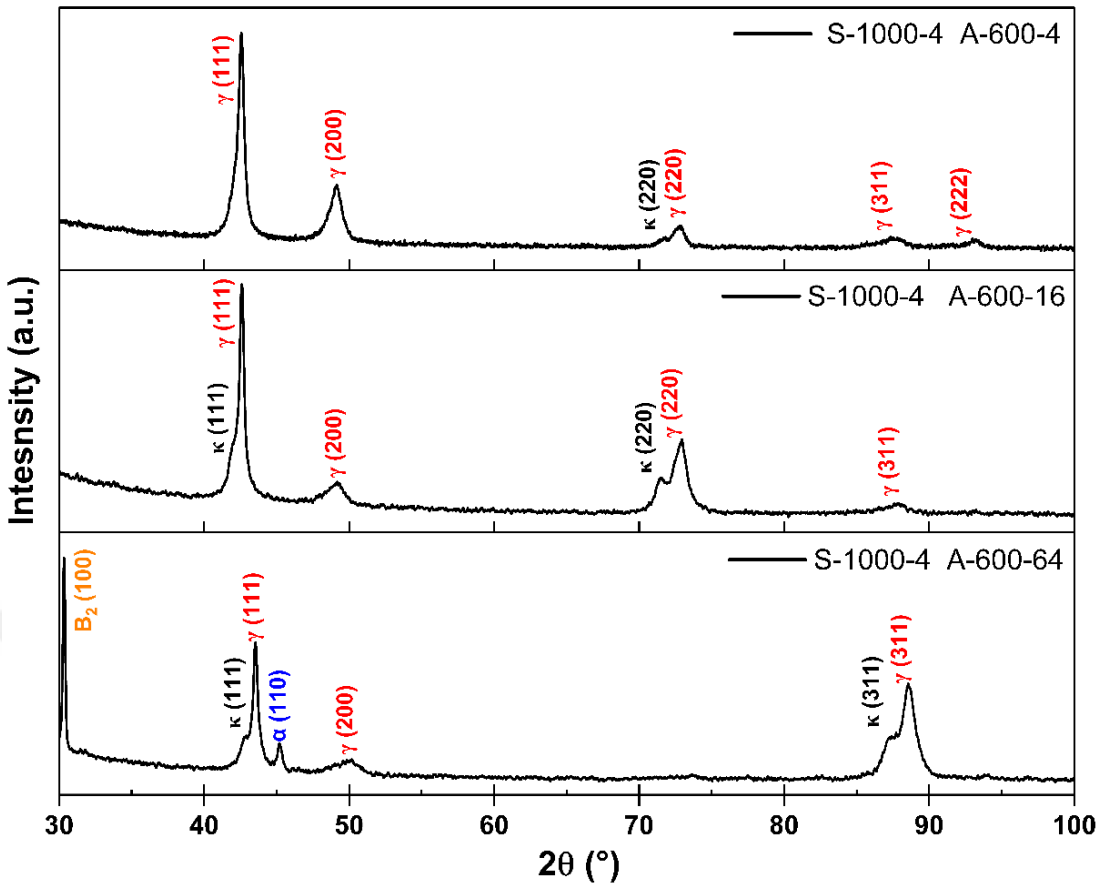

Figure 4.36 XRD pattern of the sample after solution heat treatment at 1000°C for 4 h, followed by aging at 600°C for 4-16-64 h

4.5. Results of the Wear Tests and Examination of the Worn Samples

Wear test calculations were made using Equation (3.3). The wear results of different solution conditions at constant aging temperature and time (550°C - 16 hours) are shown in *Figure 4.37*. The wear results of the samples with as-cast and solution heat treatment applied for 2 and 4 hours at 950-1050-1150°C after aging are given in the relevant graph, and these tests are Test Level S. The wear rate of the as-cast sample was calculated as 9.00×10^{-7} g/N.m. The results for the samples aged at 550°C for 16 hours after solution heat treatment at 950°C for 2 and 4 hours were calculated as 8.70×10^{-7} and 8.40×10^{-7} g/N.m, respectively. The results for the samples aged at 550°C for 16 hours after solution heat treatment at 1050°C for 2 and 4 hours were calculated as 7.80×10^{-7} and 9.30×10^{-7} g/N.m, respectively. Finally, the results for the samples aged at 550°C for 16 hours after solution heat treatment at 1150°C for 2 and 4 hours were calculated as 8.20×10^{-7} and 8.30×10^{-7} g/N.m, respectively.

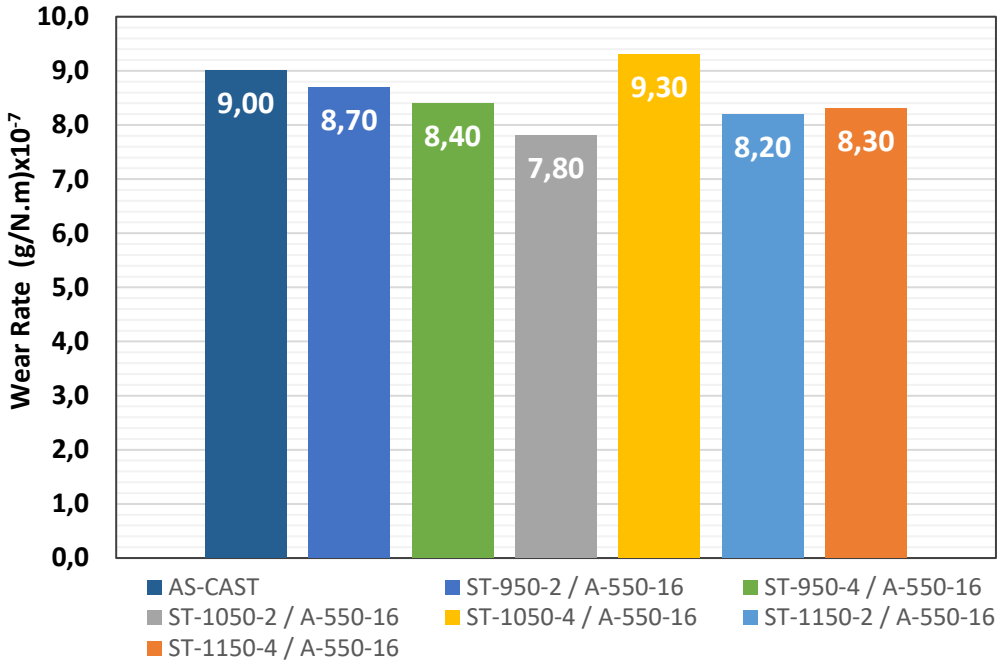

Figure 4.37 Wear test results of as-cast and 2-4 hour solution heat treatment at 950-1050-1150°C and then 16-hour aged samples at 550°C

After the solution temperature and time (1000°C-4h) fixed after Test Level S, the wear test results after aging for 4-16-64 hours at 500°C are given in *Figure 4.38* for Test Level A. After aging for 4 hours, the wear test result was 10.30×10^{-7} g/N.m. When the aging time was increased to 16 hours, the wear rate was calculated as 11.90×10^{-7} g/N.m. At the final aging for 64 hours, the wear rate was 11.50×10^{-7} g/N.m.

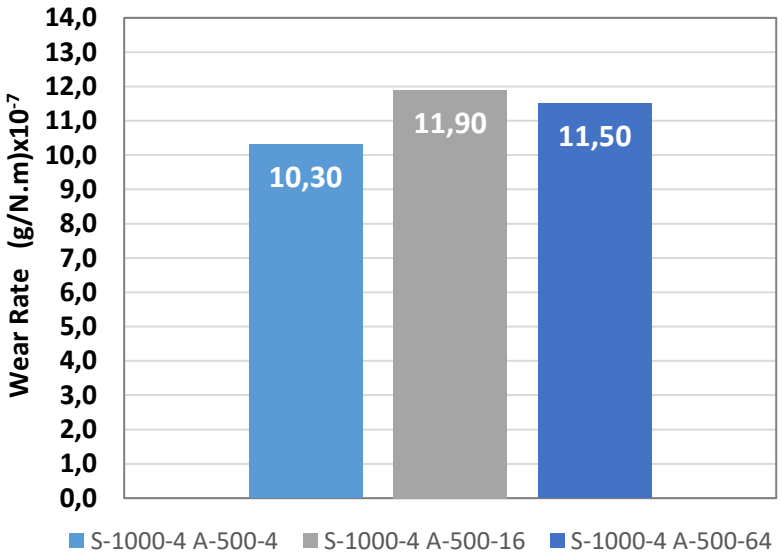

Figure 4.38 Wear test results after 1000°C - 4h solution and 4-16-64 aging at 500°C

Figure 4.39 shows the wear test values after aging at 550°C. Wear test results of 11.70×10^{-7} g/N.m after 4 hours of aging, 12.00×10^{-7} g/N.m after 16 hours of aging, and finally 13.60×10^{-7} g/N.m after 64 hours of aging were obtained.

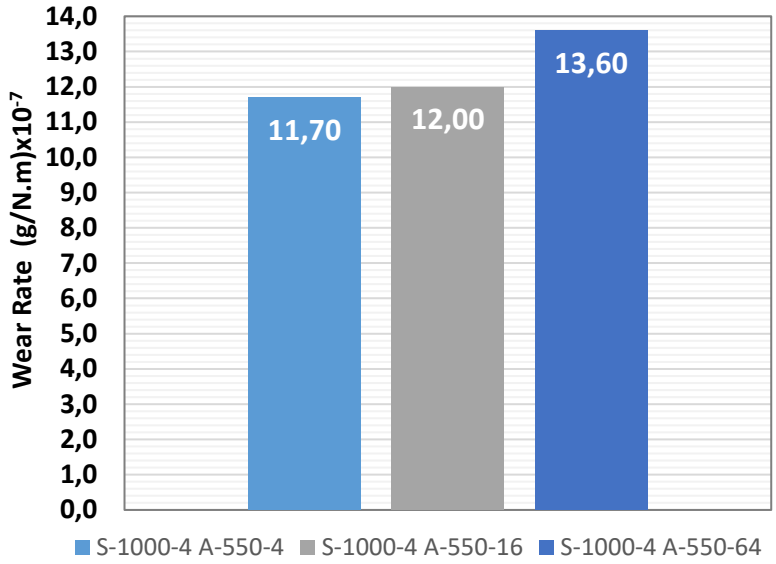

Figure 4.39 Wear test results after 1000°C - 4h solution and 4-16-64 aging at 550°C

As shown in *Figure 4.40*, in the wear tests performed after aging at 600°C for 4-16-64 hours, the results were calculated as 13.10×10^{-7}, 12.70×10^{-7} and 10.50×10^{-7} g/N.m.

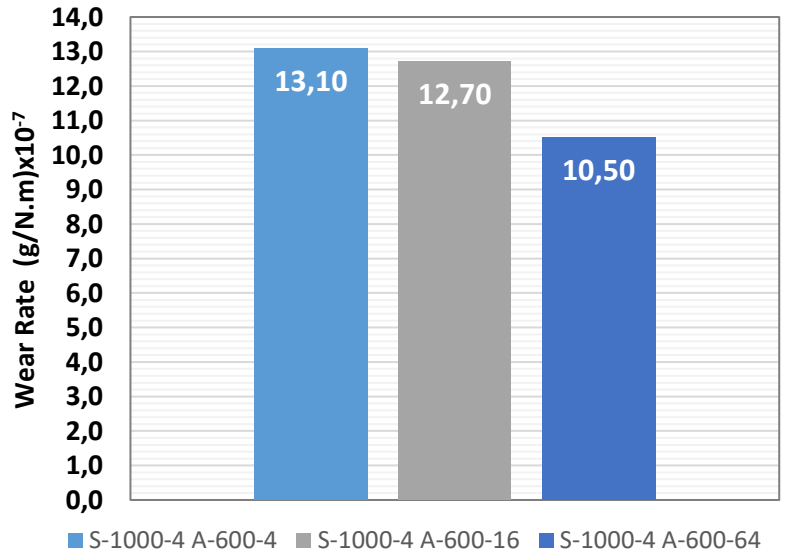

Figure 4.40 Wear test results after 1000°C - 4h solution and 4-16-64 aging at 600°C

Table 4.6 shows the wear test results of samples that were solution heat treated at 950-1050-1150°C for 2 and 4 hours and then aged at 500-550-600°C for 4-16-64 hours in solution at 1000°C for 4 hours. Additionally, for comparison purposes, wear tests were performed on AISI 4140 (385.6 HB) steel under the same test conditions and results are included in the table.

Table 4.6 Wear test results of solution and aging samples at different temperatures and time ((g/N.m)x10^{-7})

SOLUTION HEAT TREATMENT		**AGING**								
		500°C			550°C			600°C		
		4h	16h	64h	4h	16h	64h	4h	16h	64h
950°C	2h	-	-	-	-	8.70	-	-	-	-
	4h	-	-	-	-	8.40	-	-	-	-
1000°C	4h	10.30	11.90	11.50	11.70	12.00	13.60	13.10	12.70	10.50
1050°C	2h	-	-	-	-	7.80	-	-	-	-
	4h	-	-	-	-	9.30	-	-	-	-
1150°C	2h	-	-	-	-	8.20	-	-	-	-
	4h	-	-	-	-	8.30	-	-	-	-
AS-CAST		9.00								
AISI 4140		12.80								

Three different samples were selected for cross-sectional SEM examination after wear tests. These samples were the as-cast sample, sample subjected to solution heat treatment at 1000°C for 4 hours and the sample aged at 550°C for 16 hours after solution heat treatment at 1000°C - 4 hours. In *Figure 4.41*, the regions where SEM images were taken are shown schematically.

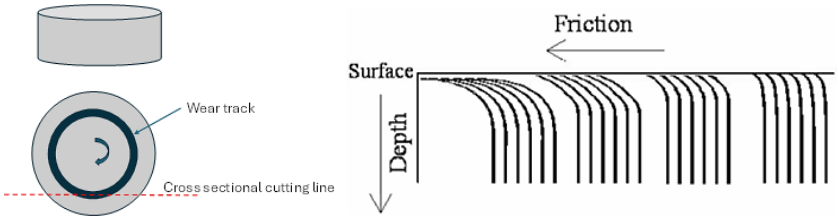

Figure 4.41 Schematic representation of the wear test SEM analysis area

Figure 4.42 shows the SEM image of the as-cast sample after the wear test. The depth of the subsurface deformation reaches to 15.48 µm.

Figure 4.42 As-cast wear depth microstructural structure image

Figure 4.43 shows the SEM image of the wear test sample subjected to solution heat treatment at 1000°C for 4 hours. The depth of the worn sample subsurface flow line is 26.99 µm.

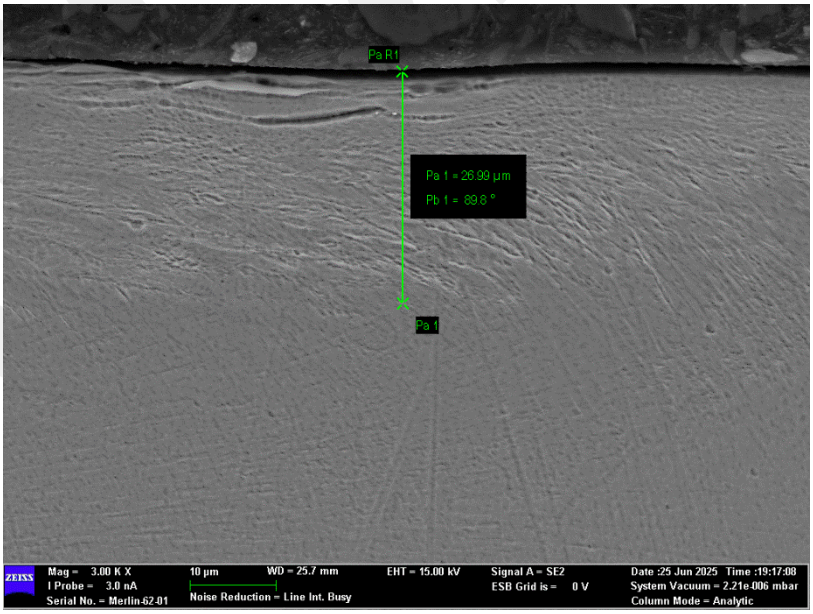

Figure 4.43 Solution heat treated sample wear depth microstructural image

Figure 4.44 shows the SEM image of the wear test sample aged at 500°C for 16 hours after solution heat treatment at 1000°C - 4 hours. The depth of the worn sample subsurface flow line is 16.25 µm.

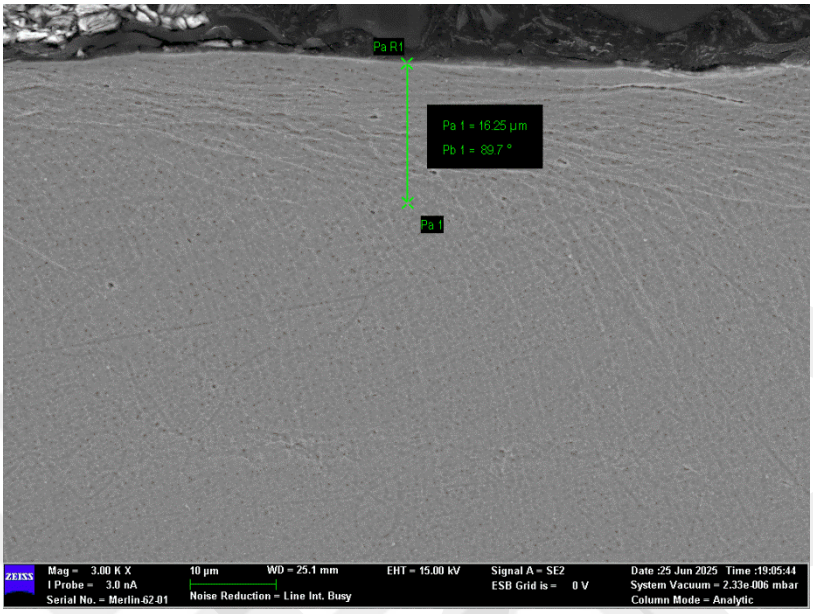

Figure 4.44 Aged sample wear depth microstructural image

CHAPTER 5

DISCUSSION

5.1. Effects of Solutionizing and Aging Conditions

The average hardness values of the as cast and different solutionizing temperatures and times are given in *Figure 5.1*. The hardness, which was 347.8 HB in the as-cast state, was measured between 190-220 HB after solution heat treatment. As the solution temperature was kept constant and time was increased, a gradual decrease in hardness was observed for all temperatures. For example, after 2-4-16 hours of solution heat treatment at 950°C, the hardness was measured as 217.6 - 213.6 - 204.6 HB. The hardness increased with the decrease in solutionizing temperature. For example, for 4 hours of solutionizing heat treatment at 950-1000-1050-1150°C, the hardness was observed as 213.6 - 212.6 - 205.4 - 189.4 HB, respectively. According to the test results, increasing the temperature or time in solution heat treatment causes a decrease in hardness. It is consistent with the literature that increasing the temperature for solution heat treatment causes a decrease in hardness (see *Table 2.4*).

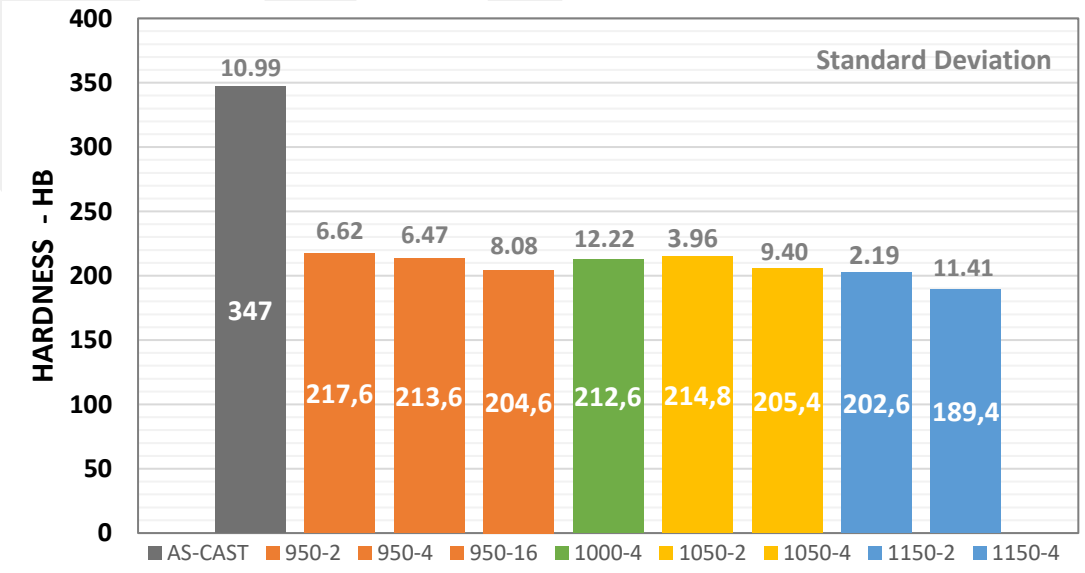

Figure 5.1 Average hardness values of the as-cast and solution heat treated samples

In addition, heterogeneous and grain boundary precipitates due to solidification in the as-cast microstructure were not observed after the solutionizing heat treatment. However, no significant difference was observed in the microstructures after solution heat treatment at different temperatures and times. In *Figure 5.2*, the microstructure images of as-cast and 950°C 2-hour solution-treated samples are shown as examples.

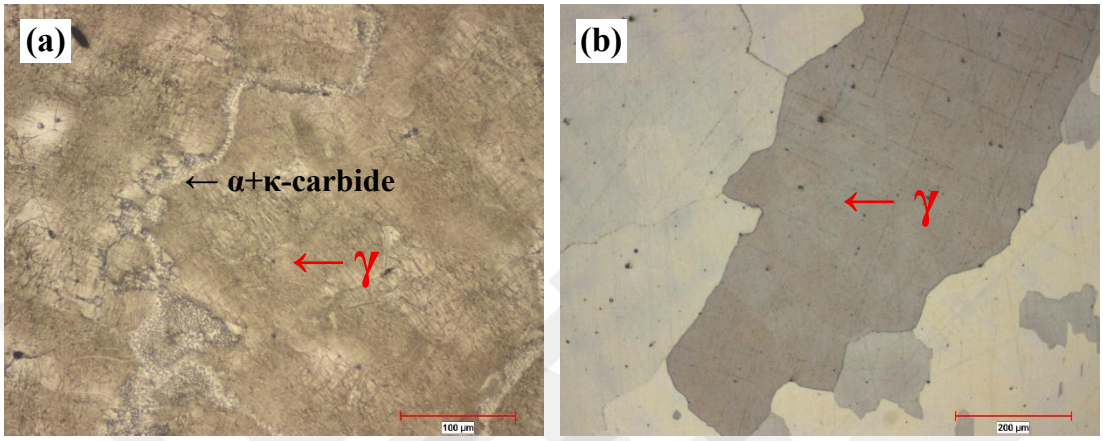

Figure 5.2 Optical microstructural images of the (a) as-cast, and (b) solution treatment at 950°C for 2 hours

In addition, since the samples were cast and not subjected to any forging or rolling process, there was no recrystallization, and therefore, the grain sizes did not show significant differences after solution heat treatment. To better understand this, the microstructure images of the samples subjected to solution treatment at 950°C for (a) 2 and (b) 16 hours are shown in *Figure 5.3*.

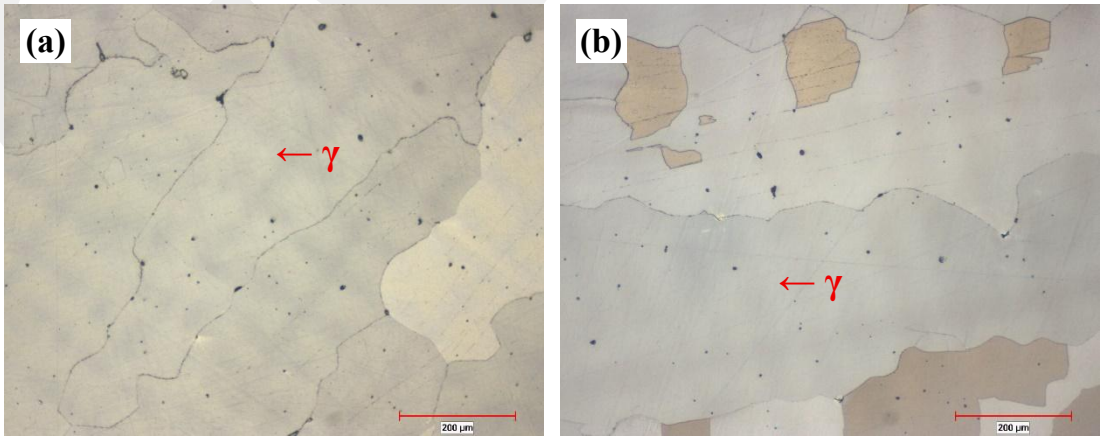

Figure 5.3 Optical microstructural images after a solution treatment at 950°C for (a) 2h, and (b) 16h

Figure 4.17 shows the as-cast SEM image, in addition to this the EDS spot analysis performed for the as-cast microstructure, measurements of the κ-carbide and α were made as shown in *Figure 4.20*. The results are summarized in *Table 5.1*. According to the analysis results, when two regions are compared based on Al, the Al content of the dark-colored regions in the picture is lower than the light-colored regions. It is known that the aluminum accelerates and increases the formation of ferrite, therefore the dark regions in the structure are κ-carbide and the light regions are α. The SEM image in *Figure 2.10* also appears in the literature to coincide with the α + κ-carbide structure that can be seen in the grain boundaries in the as-cast state. In addition, EBSD analyses in *Figure 4.23* show that for as-cast, ferrite regions are present not only at the grain boundaries but also spread throughout the microstructure.

Table 5.1 EDS point analysis results for κ-carbide and α in as-cast sample

Analysis (wt%) / **Area**	**Fe**	**Mn**	**Al**	**Si**
κ-carbide	59.42	31.04	8.30	1.24
α	53.57	34.20	11.30	0.93

The results of EDS line analysis for as-cast are summarized in *Table 5.2*. According to the analysis results, no element fluctuations were observed along the line, especially in the analysis graph including grain and grain boundary, given in *Figure 4.21*. Similarly, no element fluctuations were observed in the graph obtained from the line analysis made along the grain boundary shown in *Figure 4.22*. When the two line analyses are compared, the element distribution appears to be similar in general terms. While the Si ratio of the analysis containing the grain and grain boundary is higher than the other, the Al ratio of the analysis made along the grain boundary is higher.

Table 5.2 EDS line analysis performed on grain and grain boundary

Analysis (wt%) / **Area**	**Fe**	**Mn**	**Al**	**Si**
Grain→ Grain Boundary	58.00	31.82	9.19	0.99
Along the Grain Boundary	58.30	31.26	9.71	0.73

The results of image analyses performed with ImageJ are given in *Table 5.3* and the images in *Figure 5.4* (white regions represent austenite, black regions represent precipitates, inclusions, etc.). The results show that precipitate formation increases with the increase in aging temperature or time, and at the same time, the amount of austenite decreases accordingly.

Table 5.3 ImageJ phase distribution results of solutionized and aged samples.

Sample	Austenite	Precipitates, Inclusions, etc.
ST : 1000°C – 4h	~ 99.3%	Rest
ST : 1000°C – 4h **AGING : 550°C – 4h**	~ 99.1%	Rest
ST : 1000°C – 4h **AGING : 550°C – 16h**	~ 98.2%	Rest
ST : 1000°C – 4h **AGING : 550°C – 64h**	~ 96.2%	Rest

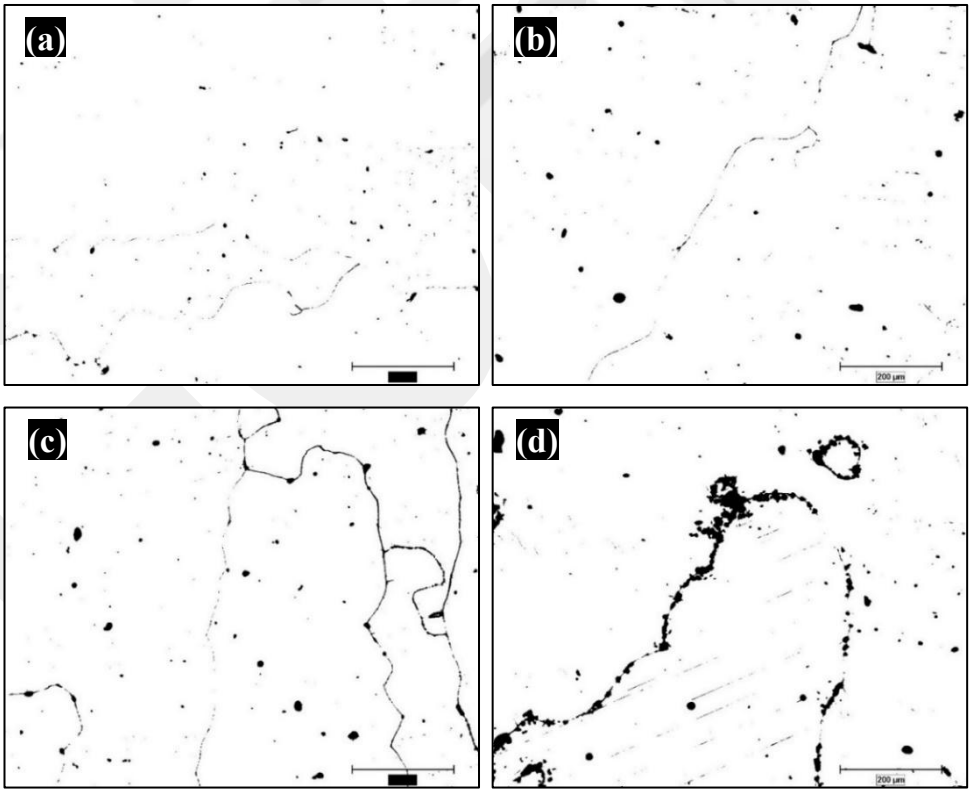

Figure 5.4 Microstructure images from ImageJ: (a) ST: 1000°C - 4h, (b) ST: 1000°C - 4h / AGING: 500°C - 4h, (c) ST: 1000°C - 4h / AGING: 500°C - 16h, (d) ST: 1000°C - 4h / AGING: 500°C - 64h

In *Figure 5.5*, the hardness of the disk samples taken into solution and then subjected to 550°C - 16 hours aging process is shown graphically. While the hardness of the sample applied with solution heat treatment at 950°C for 2 hours was 217.6 HB, the hardness after aging reached 396.4 HB, the sample applied for 4 hours increased from 213.6 HB to 411.8 HB after aging, the hardness was 204.6 HB after 16 hours and reached 376 HB with aging. After the solution heat treatment at 1000°C – 4 hours, the hardness was 212,6 HB, but after aging, the hardness increased to 368 HB. For solution heat treatment at 1050°C, the hardness increased from 214.8 HB after 2 hours to 370.8 HB after aging, and from 205.4 HB for 4 hours to 381.2 HB after aging. For solution heat treatment at 1150°C, the hardness increased from 202.6 HB after 2 hours to 356.6 HB after aging, and from 189.4 HB for 4 hours to 361.8 HB after aging. When all data were examined, it was seen that the highest hardness increase (92.77%) from 213.6 HB to 411.8 HB belonged to the sample that was solution heat treated at 950°C for 4 hours and aged at 550°C for 16 hours. The lowest hardness increase (72.66%) from 214.8 HB to 370.8 HB belonged to the sample that was solution heat treated at 1050°C for 2 hours and aged at 550°C for 16 hours.

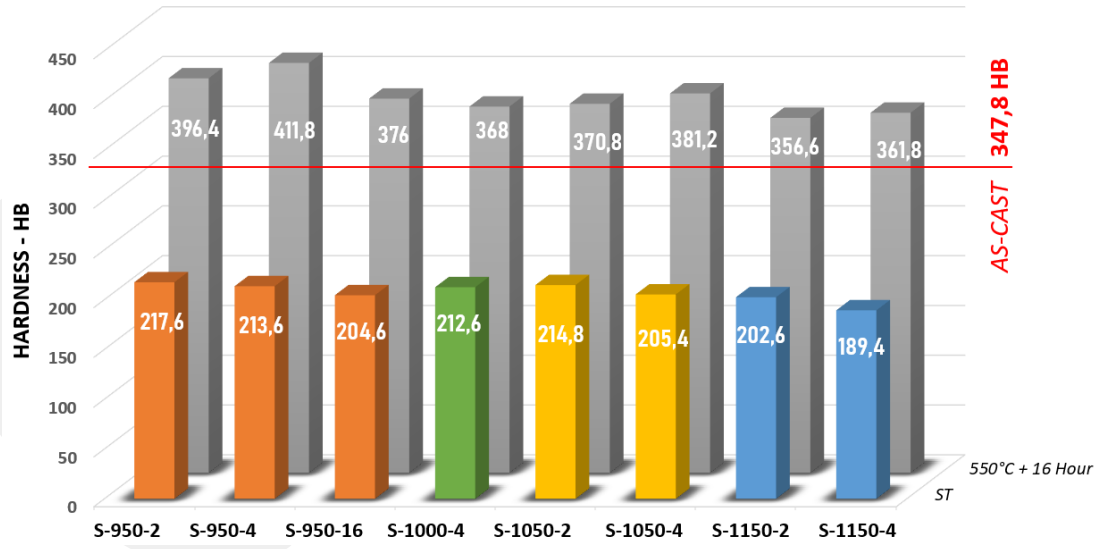

Figure 5.5 Average hardnesses obtained after solution heat treatment at different temperatures and times while aging condition is fixed

The hardnesses obtained after solution heat treatment and aging are in the range of 360-410 HB and are consistent with the literature. The highest value obtained belongs to the sample aged at 550°C for 16 hours after solution heat treatment at 950°C - 4

hours and the hardness is 411.8 HB. The lowest hardness value observed belongs to the sample aged at 550°C for 16 hours after solution heat treatment at 1150°C - 2 h with 356.6 HB. One of the important observations in the tests performed is that the hardness values of the samples subjected to 2 and 4 hours of solution heat treatment (950-1050-1150°C) were lower in the 4-hour samples, while the hardness values of the 4 hour solutionized samples after the same aging conditions were applied (550°C-16 h) were always higher than the 2 hour sample. This may be because higher diffusion rates are reached in the microstructure with the increase of solution time and alloying elements are more homogeneously distributed in the structure for precipitates to form during aging. To see the effect of this situation more clearly, when the solution time at 950°C was kept longer (16 hours), it was observed that the hardness value after aging decreased compared to the 4 hour solution time. Considering these heat treatments, it can be said that 4 hours of solution heat treatment is optimum. When the temperature increased while keeping the 4 hour solution heat treatment time constant, the hardness decreased under similar aging conditions (550°C-16 hour).

- **ST** 950°C – 4 Hour: **213.6 HB** → **AGING** 550°C-16 Hour: **411.8 HB** (%92.8)
- **ST** 1000°C – 4 Hour: **212.6 HB** → **AGING** 550°C-16 Hour: **368.0 HB** (%73.2)
- **ST** 1050°C – 4 Hour: **205.4 HB** → **AGING** 550°C-16 Hour: **381.2 HB** (%85.6)
- **ST** 1150°C – 4 Hour: **189.4 HB** → **AGING** 550°C-16 Hour: **361.8 HB** (%91.1)

As a result of the evaluations made with the data obtained in Test Level S, the fixed solution heat treatment temperature and time determined for Test Level A were determined as 1000°C and 4 hours. The hardness values obtained after aging at different 500-550-600°C for 4-16-64 hours with the fixed solution heat treatment temperature are given in *Figure 5.6* as a graph. As can be seen in the graph, the decrease in the aging temperature resulted in higher hardness values at similar hours. At 500°C and 550°C, the hardness increased with the aging time extending from 4 to 16 hours and the hardness decreased when 64 hours were reached. Additionally, hardness decreases with longer aging times has been observed in the literature (see *Figure 2.27*). For 600°C, the hardness increased by 3 HB from 4 to 64 hours, and according to this graph, the hardness increase obtained in the aging for 600°C can be

ignored. In general, the graph can be selected as the time when the aging time reached its peak value at the end of 16 hours for all temperatures, and the highest hardness was obtained. The highest hardness obtained was 378.8 HB after 16 hours of aging at 500°C. The decrease in hardness with the increase in aging temperature and time may be due to the precipitates coarsening formed in the structure and at the grain boundaries.

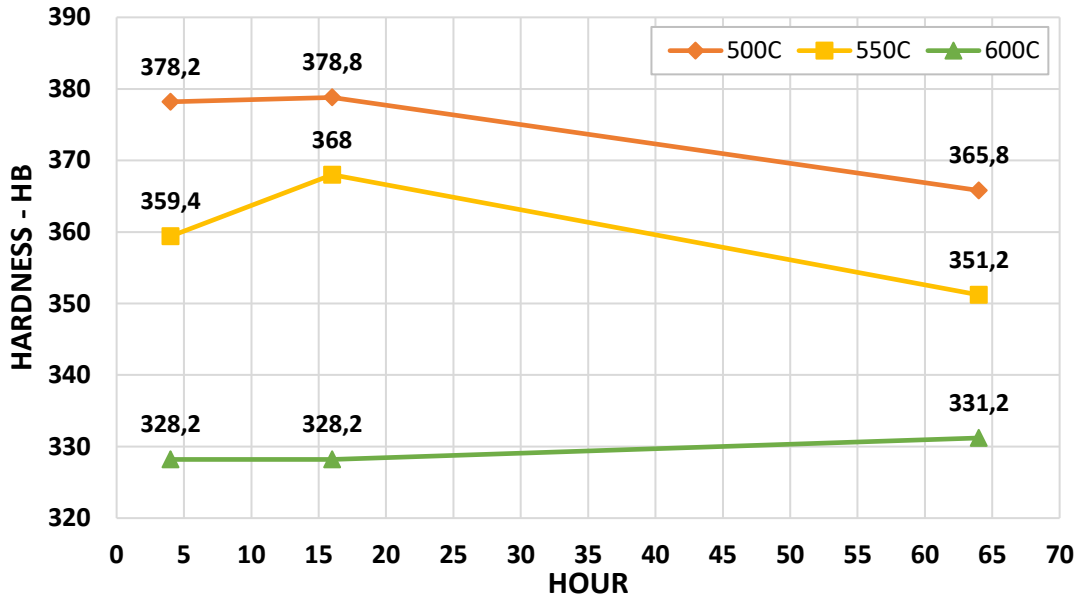

Figure 5.6 Average hardness results after aging at 500-550-600°C for 4-16-64 hours

To see more clearly the precipitates formed in the microstructure depending on the increasing aging time and time, the microstructures after aging at 600°C for 4-16-64 hours are shown in *Figure 5.7*. This aging at 600°C clearly shows that with the increase of aging time, precipitate formation occurs at the grain boundaries, which has a negative effect on the mechanical properties.

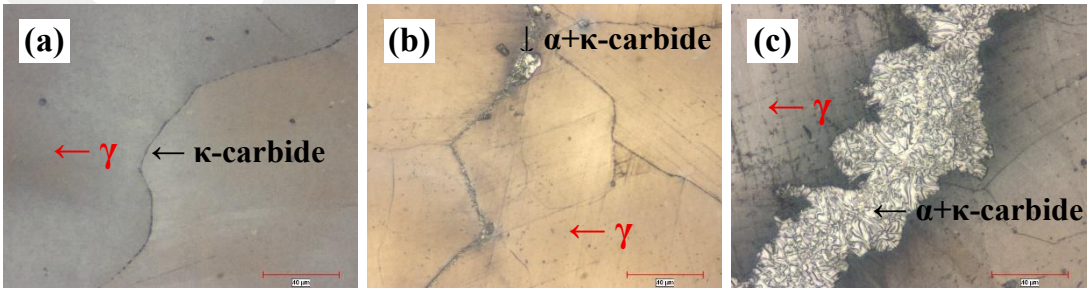

Figure 5.7 Optical microstructural images after solution heat treatment at 1000°C for 4 hours and aging at 600°C for (a) 4h, (b) 16h, and (c) 64h (Vilella etched, 500X)

After the solution temperature and time were fixed and aging processes were carried out at 500-550-600°C for 4-16-64 hours, 16 hours was selected as the most suitable time both in terms of hardness and not causing undesirable precipitate coarsening at grain boundaries.

The aging results at different temperatures (400-450-500-550-600-650-700°C) for a fixed time of 16 hours are shown in the graph in *Figure 5.8*. Here, as in *Figure 5.6*, the highest hardness was seen at 500°C. As a result of the decrease in temperature, the hardness values decreased due to the decrease in the energy given to the system and the decrease in the precipitates that will form as a result of this, while the coarse precipitates formed at the grain boundaries with the increase in temperature can again cause a decrease in hardness. In addition, information in the literature confirms precipitate coarsening with increasing temperature or time (*see Figure 2.7*).

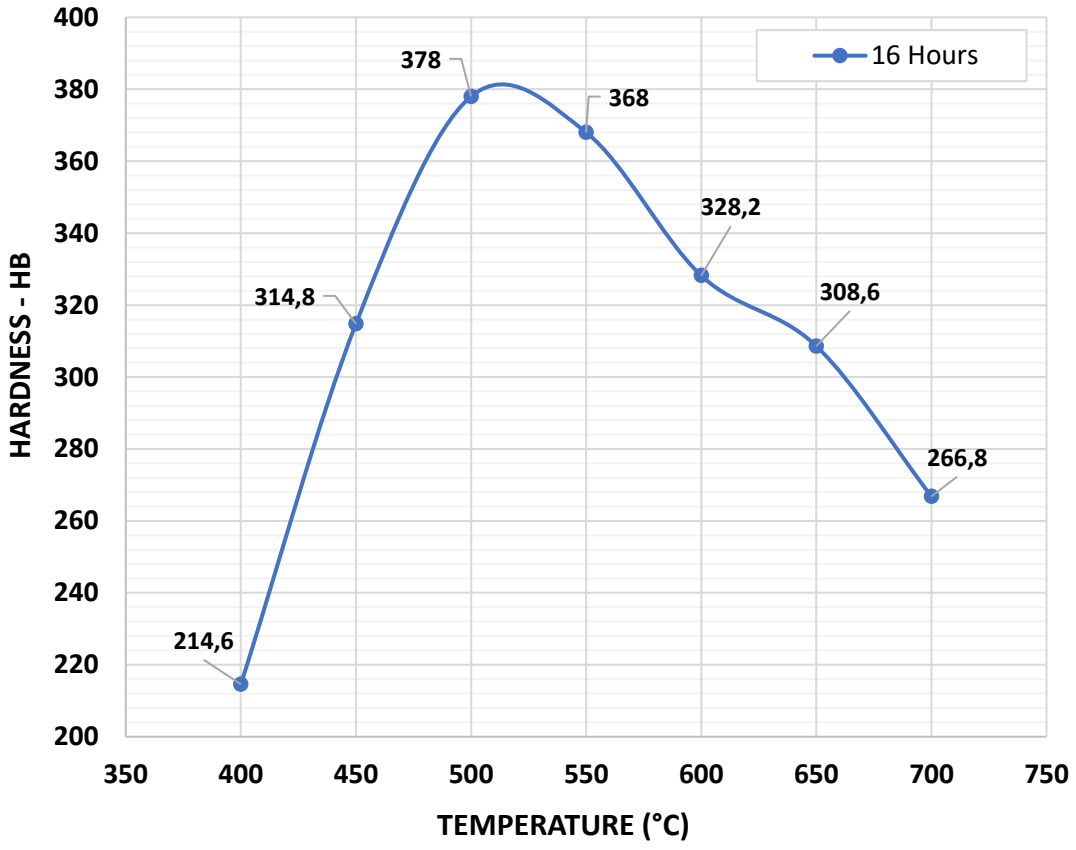

Figure 5.8 Average hardness results after solutionizing at 1000°C for 4 hours and aging at 400-450-500-550-600-650-700°C for 16 hours

5.2. Effect of Heat Treatments on Phase Distribution

XRD analyses were performed to see the phases/precipitates formed by the applied solution and aging heat treatments. *Figure 5.9* shows the comparison of the 1000°C 4 hour solution heat treatment selected after Test Level S with as-cast. This comparison clearly shows us that after the solution heat treatment, the precipitates (κ-carbides, etc.) especially at the grain boundaries in the as-cast microstructure were eliminated. At the same time, since the microstructure became more homogeneous after the solution and reached higher intensity values in the XRD analysis, a much clearer graphic could be obtained.

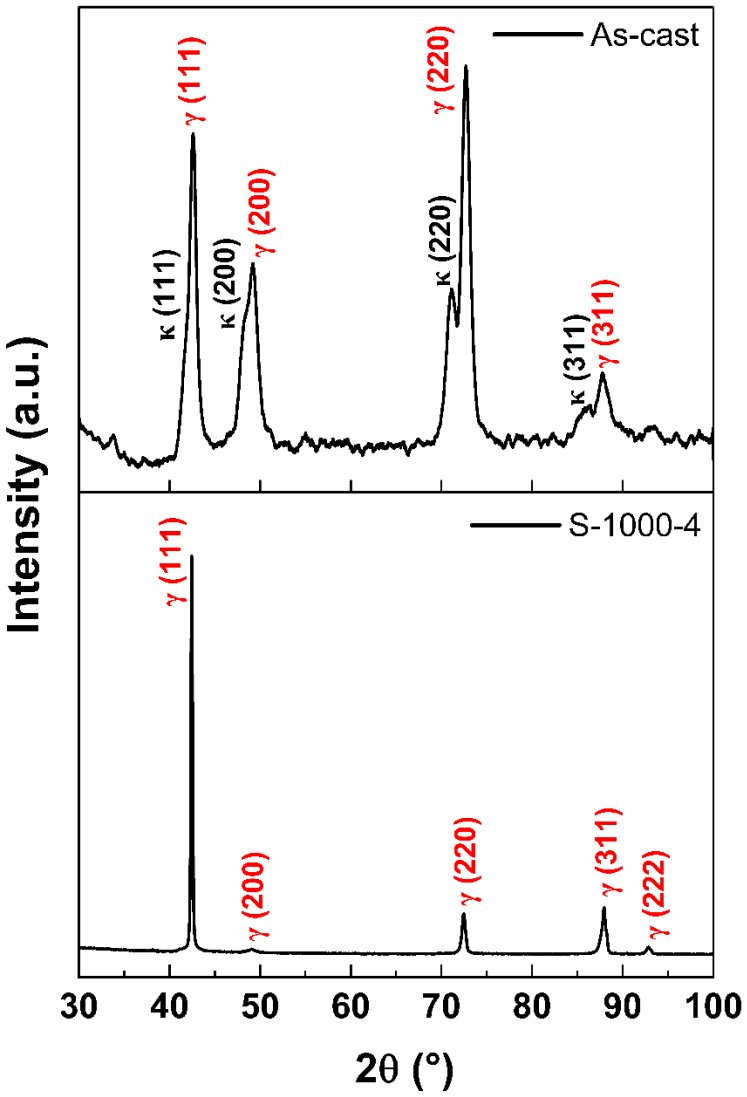

Figure 5.9 XRD results of as-cast and solution heat treatment at 1000°C for 4 hours

Another important comparison is given in *Figure 5.10*. As discussed in the previous section, it was observed that the 16-hour aging time gave the highest hardness value in light of the data obtained. The graph below shows the XRD results of the samples aged at 1000°C for 4 hours and then at 500-550-600°C for 16 hours. As seen in the graph, no κ-carbides peak is seen in the samples aged for 16 hours at 500°C and 550°C, while a κ-carbides peak is detected for the sample aged at 600°C for 16 hours. This can be attributed to the acceleration of precipitate formation due to the increase in diffusion rate with increasing temperature.

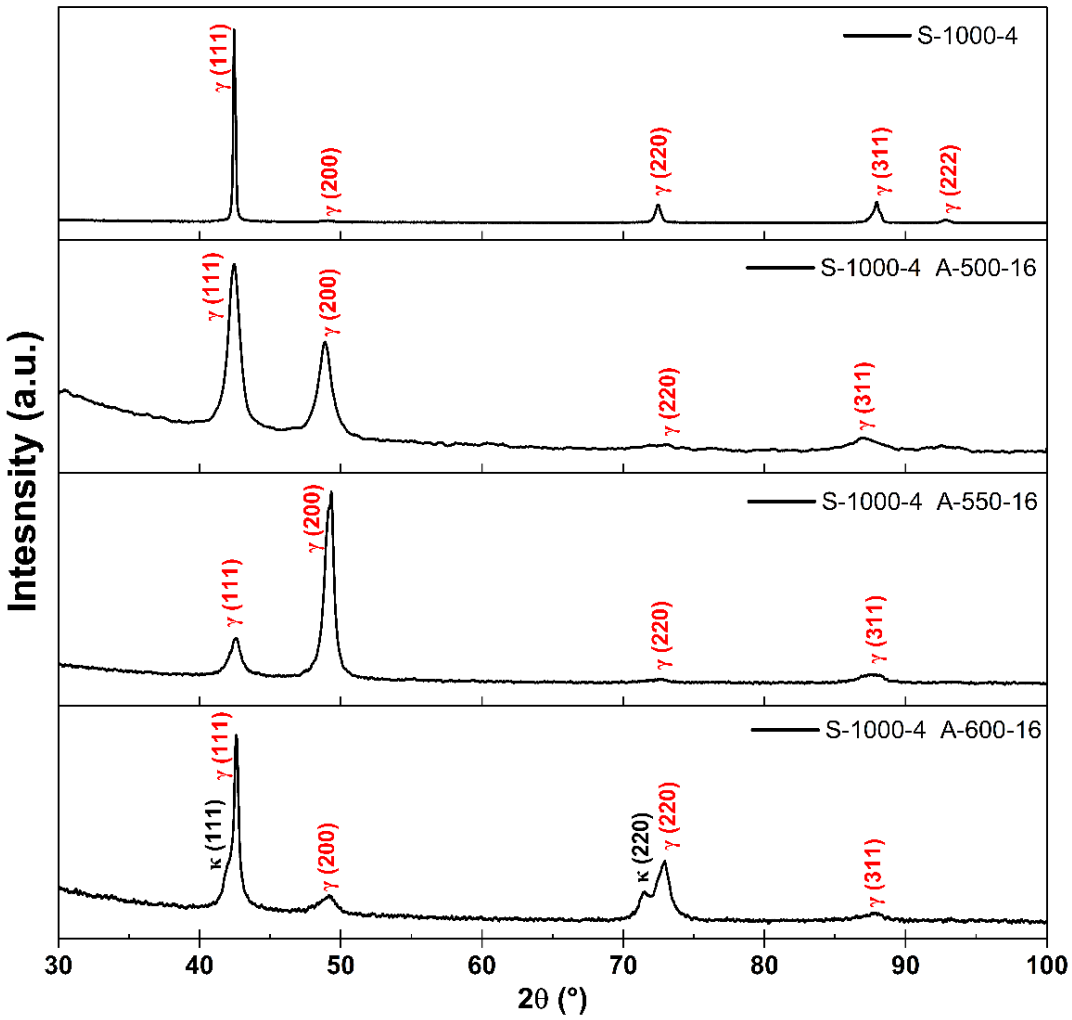

Figure 5.10 XRD results for solution heat treatment at 1000°C for 4 hours followed by aging at 500-550-600°C for 16 hours

A similar observation result is given in *Figure 5.11*. In the XRD analysis performed after 4 hours of solution heat treatment at 1000°C and 4 hours of aging at 500-550-600°C, the 70-75° range is shown in the graph. The (220) κ peak, which becomes more pronounced with increasing temperature, is seen on the left side of the (220) austenite peak. This is another indication that increasing temperature causes precipitate coarsening. Another important observation according to the graph is that the (220) austenite peak shifts to higher angles with increasing temperature. The reason for this, as mentioned before, is the increase in the diffusion rate and the decrease in the lattice parameter of the austenite matrix.

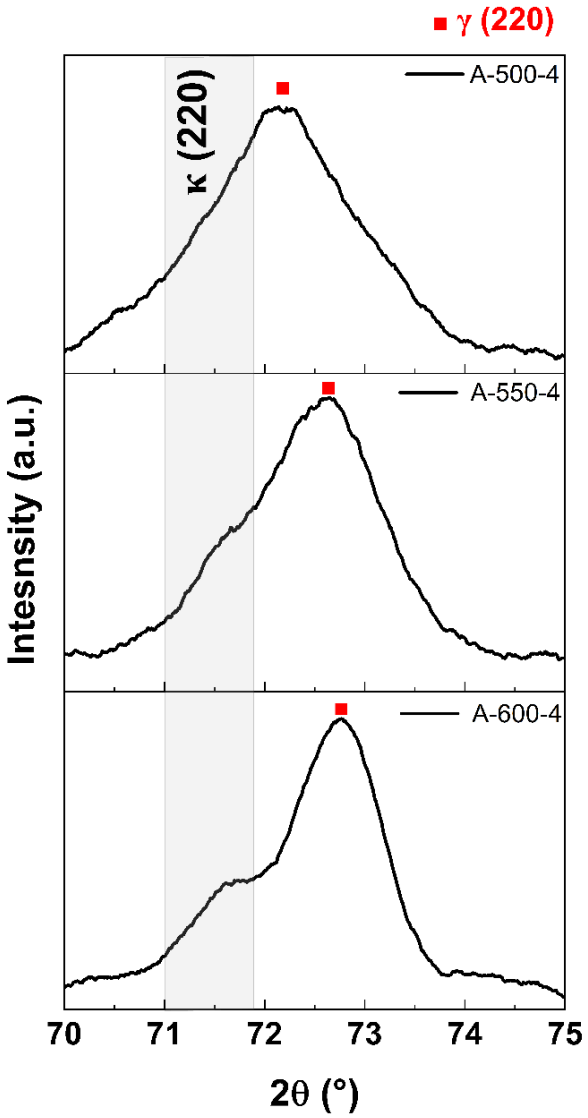

Figure 5.11 XRD results of samples aged at 500-550-600°C for 4 hours after solution heat treatment at 1000°C for 4 hours

Another comparison is given in *Figure 5.12* for different aging times at the same temperature. After aging from 4 to 64 hours at 600°C, the (111) κ-carbide peak appears on the left side of the (111) austenite peak with the increase of aging time, as in the previous graph. Unlike other temperatures, the (110) α peak at 600°C also appears with an increase in ageing time. In this graph, it is seen that the (111) austenite peak shifts to the right with the increase of aging time. This has been previously determined in the literature and is consistent with the results obtained (*see Figure 2.16*).

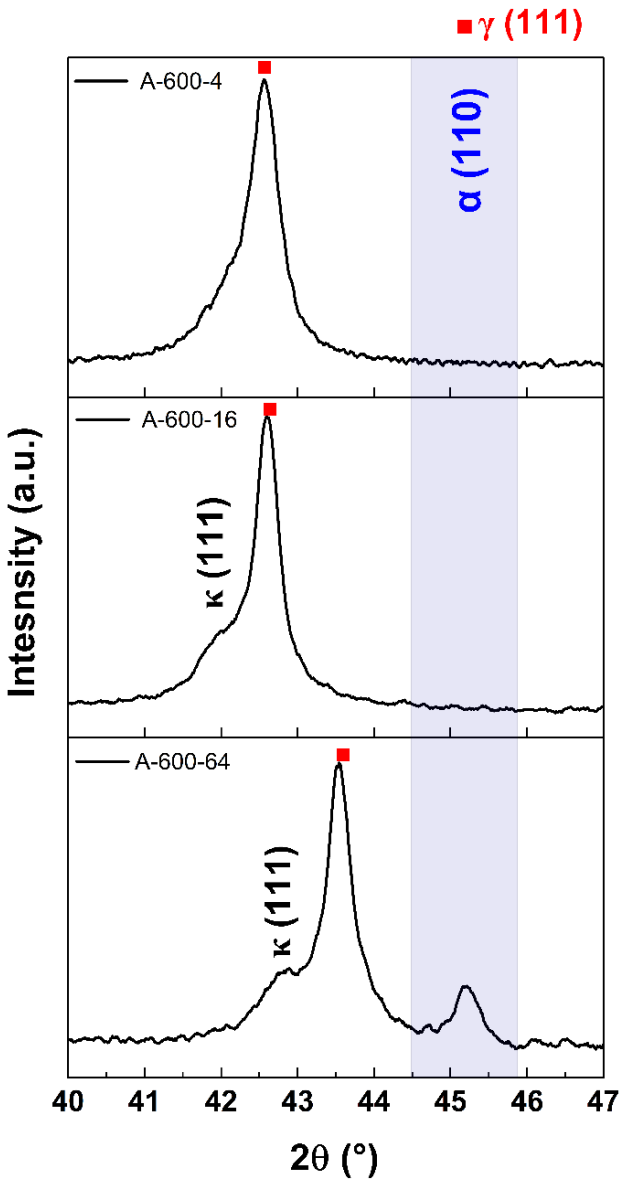

Figure 5.12 XRD results of samples aged at 600°C for 4-16-64 hours after solution heat treatment at 1000°C for 4 hours

5.3. Wear Behavior of the Samples

Wear tests and hardness values of samples for Test Level S are shown in *Figure 5.13*. After solution heat treatments at 950-1050-1150°C for 2 and 4 hours, followed by 550°C for 16 hours and constant aging, the wear results were between 8.20×10^{-7} – 9.30×10^{-7} g/N.m. The hardness range for the same samples was measured as 356-411 HB. Firstly, the wear test results of the solution samples at 1150°C for 2 and 4 hours were 8.20×10^{-7} and 8.30×10^{-7} g/N.m, respectively, and the sample hardnesses were measured as 356.6 and 361.8 HB. Increasing the solution time from 2 to 4 hours resulted in a minimal increase in wear, accompanied by a slight increase in hardness. A similar trend was observed in the wear test and hardness results after 2 and 4 h solution heat treatments at 1050°C. The wear test results for the 1050°C 2 and 4 h samples were 7.80×10^{-7} and 9.30×10^{-7} g/N.m, while the hardnesses were measured as 370.8 and 381.4 HB. This resulted in an increase in the wear and hardness values at 1050°C as the solution time extended from 2 to 4 h. The wear test results for 2 and 4 hours at 950°C were 8.70×10^{-7} and 8.40×10^{-7} g/N.m, respectively, and the hardness was 396.4 and 411.8 HB. Here, unlike 1150°C and 1050°C, increasing the solution time from 2 to 4 hours caused an increase in hardness but a decrease in wear test results.

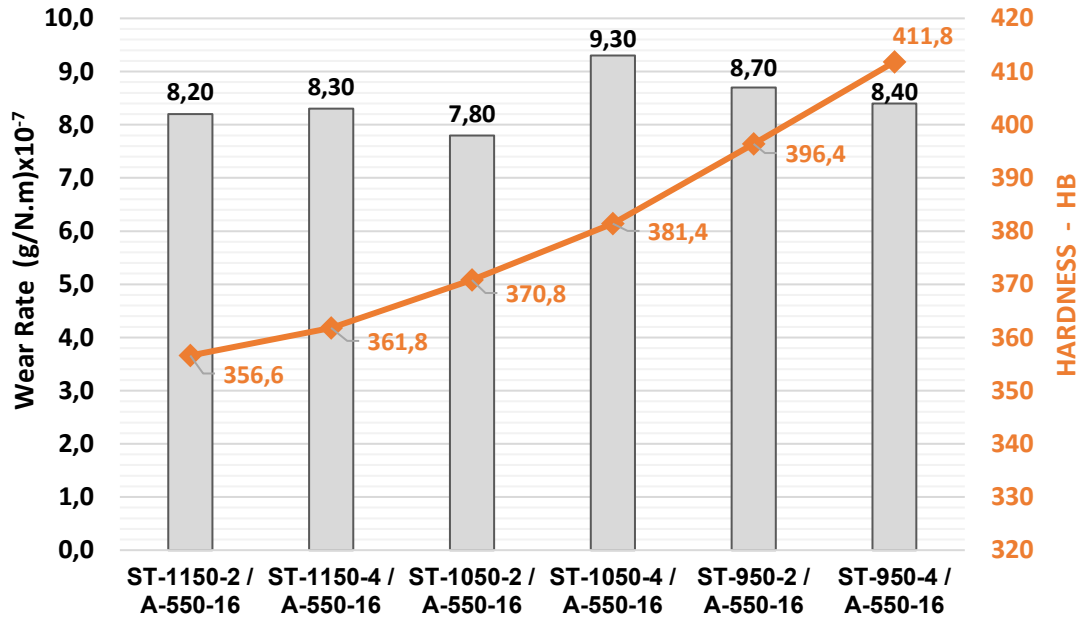

Figure 5.13 Results of hardness and wear tests of the samples solutionized at 950-1050-1150°C for 2 and 4 hours followed by aging at 550°C for 16 hours

The first of the wear tests for Test Level A, the wear and hardness graph of aging at 500°C for 4-16-64 hours after 1000°C 4 hours of solution treatment, is shown in *Figure 5.14*. When the aging time was increased from 4 to 64 hours, the wear test results were 10.30×10^{-7}, 11.90×10^{-7}, and 11.50×10^{-7} g/N.m, and the hardnesses were measured as 378.2, 378.8, and 365.8 HB. The hardness and wear results increased with the aging time increasing from 4 to 16 hours, then decreased in both values when the aging time reached 64 hours. The peaks for wear and hardness for 500°C appear after 16 hours of aging. According to the graph, it can be said that there is a relationship between hardness and wear behavior for 500°C.

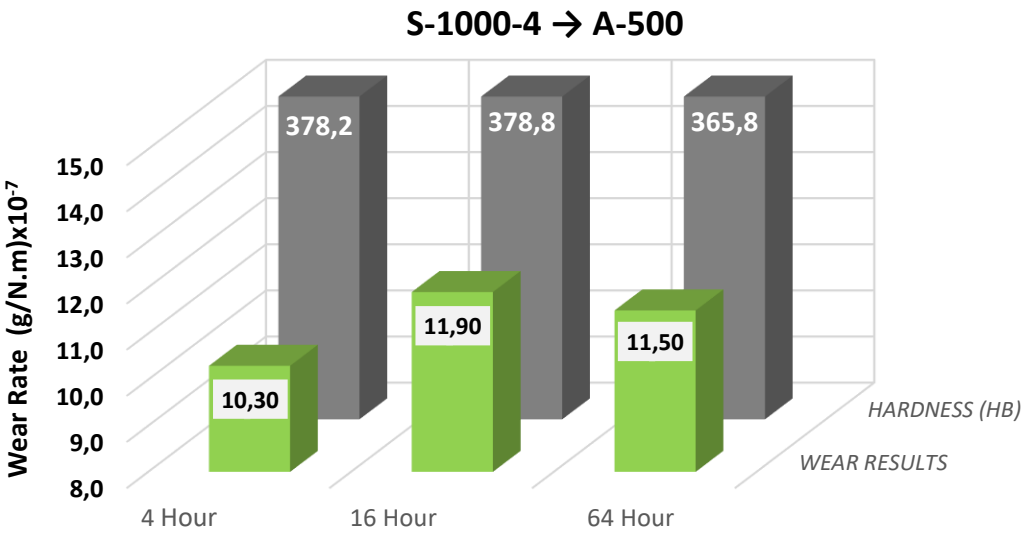

Figure 5.14 Results of wear and hardness tests after 1000°C 4 hours solution and aging at 500°C for 4-16-64 hours

The test results at 550°C are given in the graph in *Figure 5.15*. After aging at 550°C for 4-16-64 hours, the wear and hardness data were measured as 11.70×10^{-7}, 12.00×10^{-7}, and 13.60×10^{-7} g/N.m, respectively, and the hardnesses were measured as 359.2, 368, and 351.2 HB. While the hardnesses reached their peak at 16 hours, similar to the previous one, the wear results gradually increased with an increase in the aging time from 4 hours to 64 hours. According to the graph, no relationship was established between the wear and hardness values.

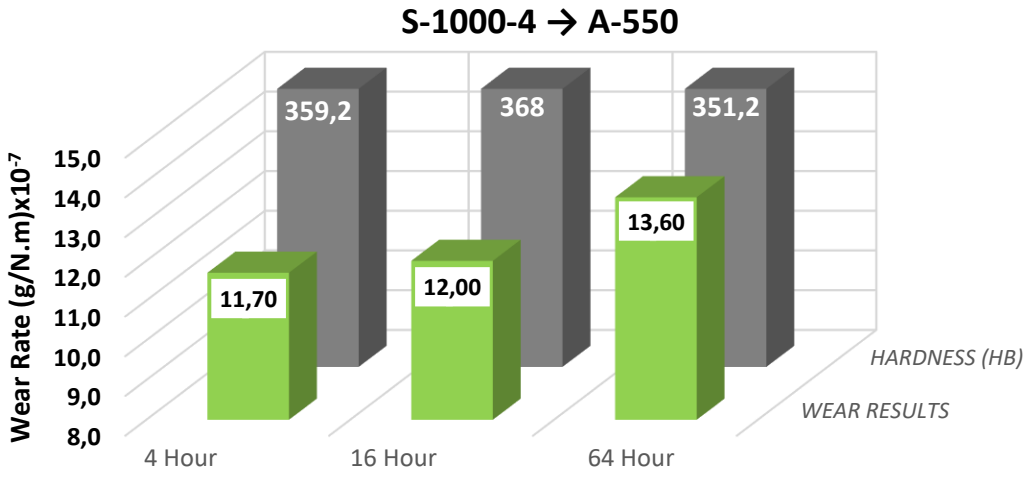

Figure 5.15 Results of wear and hardness tests after 1000°C 4 hours solution and aging at 550°C for 4-16-64 hours

The results for the last wear test performed for Test Level A, which was the aging temperature of 600°C, are shown in *Figure 5.16*. After aging for 4-16-64 hours, the wear results were measured as 13.10×10^{-7}, 12.70×10^{-7}, and 10.50×10^{-7} g/N.m, respectively, and the hardnesses were 328.2, 328.,2, and 331.2 HB. According to the results, the hardnesses showed a minimal increase with the increase of the aging time from 4 to 64 hours, while the wear results gradually decreased with the increase of time. According to the graph, it can be said that there is a negative correlation between hardness and wear.

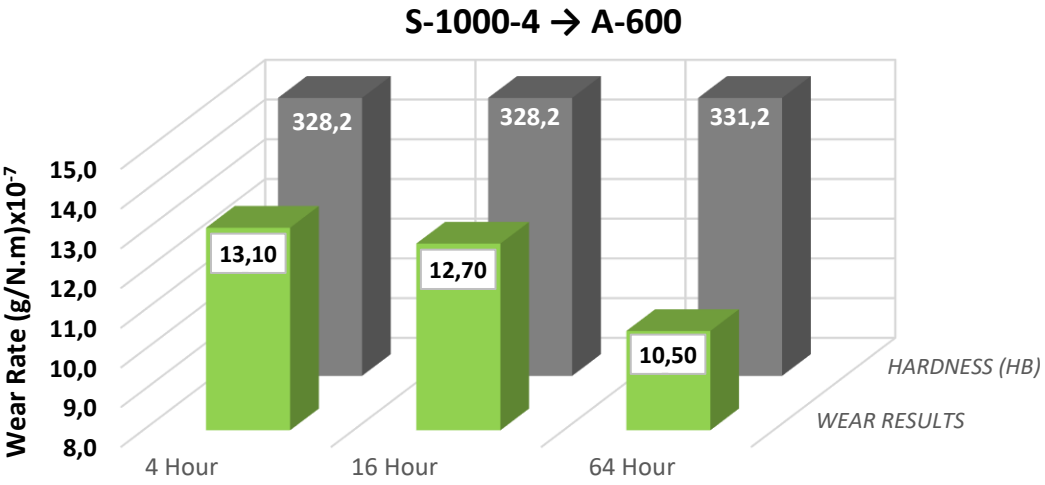

Figure 5.16 Results of wear and hardness tests after 1000°C 4 hours solution and aging at 600°C for 4-16-64 hours

In the graph given in *Figure 5.17*, the wear test results and hardness values for Test Level A were given between 400-700°C, keeping the time (16 hours) when the highest hardness results were obtained constant. According to the graph, a decrease in hardness was observed, especially with the increase of the aging temperature from 500°C to 700°C, and at the same time, the wear rate in the samples increased. Accordingly, it can be said that there is a correlation between hardness and wear rate for this range in the graph. In addition, the wear and hardness results for AISI 4140 steel using the same test conditions are also given in this graph. For example, when a comparison is made at similar hardness values (AISI 4140 – 385.6 HB / S-1000-4 A-500-16 - 378.8 HB), the S-1000-4 A-500-16 sample, with a wear value of 11.90×10^{-7} g/N.m, has a lower wear rate compared to AISI 4140 steel, which has a wear value of 12.80×10^{-7} g/N.m. In other words, the S-1000-4 A-500-16 sample exhibits higher wear resistance.

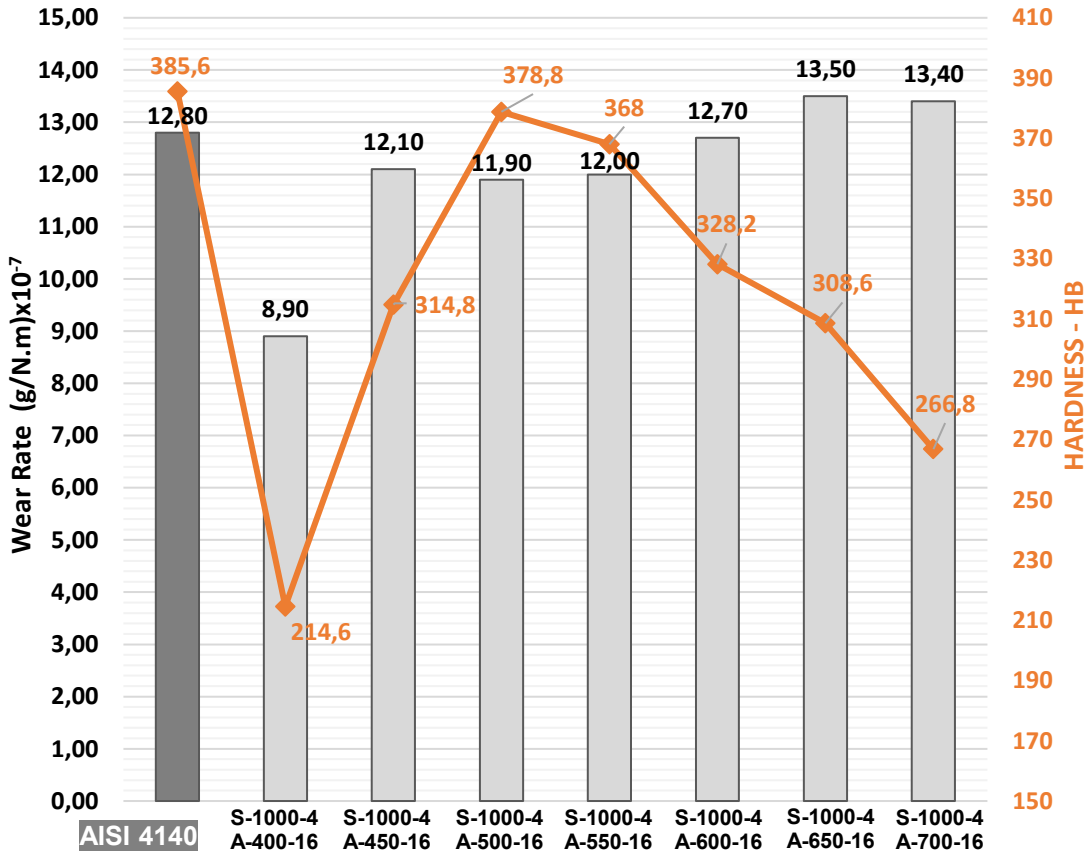

Figure 5.17 Hardness and wear test results of samples aged at 400-700°C for 16 hours after 1000°C for 4 hours and water quenched, comparison with AISI 4140 steel

Table 5.4 shows the hardness, wear test results, and wear depths (measured using SEM) of as-cast, solution heat treated, and aged samples. According to the table, the as-cast sample had a hardness of 347.8 HB and a wear depth of 15.48 μm. After solution heat treatment, the hardness decreased to 212.6 HB, and the wear depth became 26.99 μm. With subsequent aging, the hardness increased to 378.8 HB, and the wear depth became 16.25 μm. According to these results, wear depths were lower (~15-16 μm) at higher hardnesses (350-380 HB), while wear depth increased (~26 μm) with decreasing hardness. It can be concluded that the increase in hardness is directly proportional to the decrease in wear depth of deformation.

Table 5.4 Hardness, wear test, and deformation depth results of as-cast, solution heat treated, and aged samples

	AS-CAST	**ST**	**AGING**
Temperature/Time	-	1000°C - 4 Hours	1000°C - 4 Hours 500°C – 16 Hours
Hardness (HB)	347.8	212.6	378.8
Wear Rate ((g/N.m)x$10^{-7)}$	9.00	11.90	11.90
Deformation Depth (μm)	15.48	26.99	16.25

5.4. General Discussion

The analysis of the data obtained from all the tests performed reveals important insights. The chemical composition data found in the literature supports the successful attainment of the desired phases. As demonstrated in this study, the targeted phase can be achieved in a casting that adheres to the chemical composition range specified for austenitic steels in existing research.

Typically, austenitic steels undergo hot or cold rolling, or forging, followed by solution heat treatment and aging. While some studies do not employ these rolling or forging processes, the prevailing trend in literature emphasizes their significance. In this

research, the aim was to optimize mechanical and microstructural properties by applying heat treatment—specifically solution treatment followed by aging—to the cast materials without resorting to plastic deformation (hot or cold rolling or forging).

The results obtained, particularly concerning hardness values, align with findings in literature. However, the absence of recrystallization, due to the lack of hot or cold rolling or forging, meant that grain sizes remained coarse, relatively heterogeneous and textured even after solution heat treatment. Moreover, conducting mechanical tests would provide clearer insights into how hot or cold rolling, or forging, impacts yield strength, tensile strength, and percent elongation.

This thesis highlights that varying parameters such as temperature and time—specifically 2, 4, and 16 hours at 950-1000-1050-1150°C—significantly affect the hardness achieved after aging, consistent with information found in the literature. On the other hand, the aging temperature and time were examined after solution heat treatment across a broad range of temperatures (400-700°C) and time periods (4, 16, and 64 hours). These studies confirmed that the aging and temperature data found in the literature are consistent. Notably, precipitates that coarsen and form at the grain boundaries with increasing temperature and time were also observed in this research.

When evaluating all the test results presented in this thesis, it is evident that the development of materials with a high specific strength (strength-to-weight ratio) has become increasingly important in light of rising emission rates. While new-generation advanced high-strength steels aim to enhance their specific strength by improving mechanical properties while maintaining constant density, lightweight steels strive to improve both their mechanical properties and overall performance. In this context, both the literature studies and the data gathered in this thesis will facilitate the short- to medium-term industrial application of Fe-Mn-Al-C based lightweight steels.

CHAPTER 6

CONCLUSIONS

6.1. Main Conclusions

An experimental Fe-Mn-Al-C-Si lightweight steel has been cast and the effects of various solutionizing (950-1000-1050-1150°C for 2-4-16 hours) and aging (400-450-500-550-600-650-700°C for 4-16-64 hours) treatments on its microstructure, hardness, XRD, SEM (EDS-EBSD) and wear resistance have been studied. The main conclusions that can be drawn from this work are as follows:

- The casting of lightweight steel based on Fe-Mn-Al-C-Si yielded a density of 6.60 g/cm³, representing an approximately 15% reduction in density compared to conventional and advanced high-strength steels with a density of about 7.80 g/cm³, while the austenitic structure was obtained.

- After all the results were obtained, the highest hardness increase was observed in the sample that was solutionized at 950°C for 4 hours and then aged at 550°C for 16 hours with a hardness value of 411.8 HB. This corresponds to an increase of 64 HB (18.4%) compared to the hardness of the as-cast sample (347.8 HB).

- Aging experiments conducted across a wide temperature range (400–700°C) and times (4–64 hours) revealed that the highest hardness increase was achieved after aging at 500°C. Regarding aging time, it was determined that the optimum hardness enhancement occurred at 16 hours. An important conclusion drawn from this study is that extended aging temperature and time led to the formation and coarsening of precipitates along the grain boundaries.

- XRD results confirmed that the different phases present in the as-cast microstructure were not observed after the solution heat treatment, verifying the formation of a fully austenitic microstructure. Additionally, it was observed that with increasing aging temperature and time, the austenite peak shifted towards higher 2θ angles, which was also accompanied by the coarsening of precipitates and the sharpening of peaks corresponding to κ-carbides.

- The sample solution heat treated at 1000°C for 4 hours and aged at 500°C for 16 hours exhibited a wear rate of 11.90×10^{-7} g/N.m, which is lower than that of AISI 4140 steel (12.80×10^{-7} g/N.m) at similar hardness levels (378.8 HB and 387 HB), indicating superior wear resistance.

6.2. Suggestions for Future Work

- Evaluation of mechanical properties, particularly tensile strength and elongation, through tensile testing after solution treatment and aging.
- Developing various etchants or methods for preparing microstructures.
- Comparing the as-cast sample with rolled and/or forged samples with similar heat treatments.
- Observation of mechanical properties after subjecting the rolled or forged sample to a solutionizing treatment at 950°C for 4 hours, followed by aging at 500°C for 16 hours.

REFERENCES

[1] "A New Global Formability Diagram.", Internet: https://ahssinsights.org/blog/a-new-global-formability-diagram/, [Mar. 01, 2025].

[2] H. Ritchie, M. Roser, "CO_2 emissions - Our World in Data.", Internet: https://ourworldindata.org/co2-emissions, [Mar. 01, 2025].

[3] I. Gutierrez-Urrutia, "Low Density Fe–Mn–Al–C Steels: Phase Structures, Mechanisms and Properties," *ISIJ International*, vol. 61, no. 1, pp. 16–25, Jan. 2021.

[4] R. Rana, *High-Performance Ferrous Alloys*. Cham: Springer International Publishing, 2021.

[5] H. Ding, D. Liu, M. Cai, and Y. Zhang, "Austenite-Based Fe-Mn-Al-C Lightweight Steels: Research and Prospective," *Metals (Basel)*, vol. 12, no. 10, p. 1572, Sep. 2022.

[6] "Scopus - Homepage.", Internet: https://www.scopus.com/pages/home#basic, [May 19, 2025].

[7] R. HADFIELD, "Special Steels," *Nature*, vol. 135, no. 3418, pp. 741–745, May 1935.

[8] R. S. Dean, C. T. Anderson, "Alloys" USA, Patent US2329186A, Sept. 14 1943.

[9] C. R. E. Ham J. L., "Manganese Joins Aluminum to Give Strong Stainless," *Product Engineering*, pp. 51–52, Dec. 1958.

[10] G. L. Kayak, "Fe−Mn−Al precipitation-hardening austenitic alloys," *Metal Science and Heat Treatment 1969 11:2*, vol. 11, no. 2, pp. 95–97, Feb. 1969.

[11] Banerji SK, “An update on Fe–Mn–Al steels as a replacement for Ni–Cr stainless steels,” in *CONSERVATION AND SUBSTITUTION TECHNOLOGY FOR CRITICAL MATERIALS*, vol. VOLUME I, Proceedings of Public Workshop sponsored by U S. Department of Commerce/National Bureau of Standards and U.S. Department of the Interior/Bureau of Mines, pp. 180–228, 1981.

[12] J. C. Benz and H. W. Leavenworth, “An Assessment of Fe-Mn-Al Alloys as Substitutes for Stainless Steels,” *JOM*, vol. 37, no. 3, pp. 36–39, Mar. 1985.

[13] Y. G. Kim, Y. S. Park, and J. K. Han, “Low temperature mechanical behavior of microalloyed and controlled-rolled Fe-Mn-Al-C-X alloys,” *Metallurgical Transactions A*, vol. 16, no. 9, pp. 1689–1693, Sep. 1985.

[14] George S.Brady and Henry R. Clauser, *Materials Handbook - An Encyclopedia for Managers, Technical Professionals, Purchasing and Production Managers, Technicians, Supervisors, and Foremen*, Twelfth. McGraw Hill Book Company, 1989.

[15] C. Y. Chao and T. F. Liu, “Phase Transformations in an Fe-7.8Al-29.5Mn-1.5Si-1.05C Alloy,” *MTA*, vol. 24, no. 9, pp. 1957–1963, Sep. 1993.

[16] G. Frommeyer and U. Brüx, “Microstructures and Mechanical Properties of High-Strength Fe-Mn-Al-C Light-Weight TRIPLEX Steels,” *Steel Res Int*, vol. 77, no. 9–10, pp. 627–633, Sep. 2006.

[17] R. A. Howell and D. C. Van Aken, “A Literature Review of Age Hardening Fe-Mn-Al-C Alloys,” *Iron and Steel Technology*, vol. 6, p. 193, 2009.

[18] B. C. De Cooman, L. Chen, H. S. Kim, Y. Estrin, S. K. Kim, and H. Voswinckel, “State-of-the-Science of High Manganese TWIP Steels for Automotive Applications,” *Microstructure and Texture in Steels*, pp. 165–183, 2009.

[19] S. Chen, R. Rana, A. Haldar, and R. K. Ray, “Current state of Fe-Mn-Al-C low density steels,” Aug. 01, 2017.

[20] S. Hu, Z. Zheng, W. Yang, and H. Yang, “Fe–Mn–C–Al Low-Density Steel for Structural Materials: A Review of Alloying, Heat Treatment, Microstructure, and Mechanical Properties,”, *John Wiley and Sons Inc,* Sep. 01, 2022.

[21] R. Howell, T. Weerasooriya, and D. Van Aken, “Tensile, high strain rate compression and microstructural evaluation of lightweight age hardenable cast Fe-30Mn-9Al-XSi-0.9c-0.5Mo steel,” *International Journal of Metalcasting*, vol. 4, no. 1, pp. 7–18, Nov. 2010.

[22] O. A. Zambrano, “A general perspective of Fe–Mn–Al–C steels,” *J Mater Sci*, vol. 53, no. 20, pp. 14003–14062, Oct. 2018.

[23] K. Ishida, H. Ohtani, N. Satoh, R. Kainuma, and T. Nishizawa, “Phase Equilibria in Fe-Mn-AI-C Alloys,” *ISIJ International*, vol. 30, no. 8, pp. 680–686, 1990.

[24] D. J. Schmatz, “ Formation of beta manganese-type structure in iron-aluminum-manganese alloys,” *Trans. AIME*, vol. 215, pp. 112–114, 1959.

[25] L. Bartlett and D. Van Aken, “High Manganese and Aluminum Steels for the Military and Transportation Industry,” *JOM*, vol. 66, no. 9, pp. 1770–1784, Sep. 2014.

[26] Z. Wang *et al.*, “Formation mechanism of κ-carbides and deformation behavior in Si-alloyed FeMnAlC lightweight steels,” *Acta Mater*, vol. 198, pp. 258–270, Oct. 2020.

[27] O. Acselrad, I. S. Kalashnikov, E. M. Silva, R. A. Simao, C. A. Achete, and L. C. Pereira, “Phase transformations in FeMnAlC austenitic steels with Si addition,” *Metall Mater Trans A Phys Metall Mater Sci*, vol. 33, no. 11, pp. 3569–3573, 2002.

[28] L. N. Bartlett, D. C. Van Aken, K. D. Peaslee, and R. A. Howell, “Effect of Phosphorus and Silicon on the Precipitation of κ-carbides in Fe-30%Mn-9%Al-X%Si-0.9%C-0.5%Mo Alloys,” *AFS Transactions 2010 © American Foundry Society*, pp. 413–424, 2010.

[29] B. Hallstedt, A. V. Khvan, B. B. Lindahl, M. Selleby, and S. Liu, “PrecHiMn-4—A thermodynamic database for high-Mn steels,” *Calphad*, vol. 56, pp. 49–57, Mar. 2017.

[30] M. C. Li, H. Chang, P. W. Kao, and D. Gan, “The effect of Mn and Al contents on the solvus of κ phase in austenitic Fe-Mn-Al-C alloys,” *Mater Chem Phys*, vol. 59, no. 1, pp. 96–99, Apr. 1999.

[31] D. Connétable and P. Maugis, “First principle calculations of the κ-Fe3AlC perovskite and iron-aluminium intermetallics,” *Intermetallics (Barking)*, vol. 16, no. 3, pp. 345–352, Mar. 2008.

[32] Y. Feng, R. Song, Y. Wang, M. Liu, H. Li, and X. Liu, “Aging hardening and precipitation behavior of Fe-31.6Mn-8.8Al-1.38C austenitic cast steel,” *Vacuum*, vol. 181, Nov. 2020.

[33] A. P. Bentley, “Ordering in Fe-Mn-Al-C austenite,” *J Mater Sci Lett*, vol. 5, no. 9, pp. 907–908, Sep. 1986.

[34] S. M. Chu, P. W. Kao, and D. Gan, “Growth kinetics of κ-carbide particles in Fe-30Mn-10Al-1C-1Si alloy,” *Scripta Metallurgica et Materialia*, vol. 26, no. 7, pp. 1067–1070, Apr. 1992.

[35] W.-C. Cheng, C.-Y. Cheng, C.-W. Hsu, and D. E. Laughlin, “Phase transformation of the L1 2 phase to kappa-carbide after spinodal decomposition and ordering in an Fe–C–Mn–Al austenitic steel,” *Materials Science and Engineering: A*, vol. 642, pp. 128–135, Aug. 2015.

[36] P. Chen, F. Zhang, Q. C. Zhang, J. H. Du, F. Shi, and X. W. Li, “Precipitation behavior of κ-carbides and its relationship with mechanical properties of Fe–Mn–Al–C lightweight austenitic steel,” *Journal of Materials Research and Technology*, vol. 25, pp. 3780–3788, Jul. 2023.

[37] J. A. Jiménez and G. Frommeyer, “The ternary iron aluminum carbides,” *J Alloys Compd*, vol. 509, no. 6, pp. 2729–2733, Feb. 2011.

[38] P. Chen, X. Li, and H. Yi, “The κ-Carbides in Low-Density Fe-Mn-Al-C Steels: A Review on Their Structure, Precipitation and Deformation Mechanism,” *Metals (Basel)*, vol. 10, no. 8, p. 1021, Jul. 2020.

[39] M. C. Ha, J.-M. Koo, J.-K. Lee, S. W. Hwang, and K.-T. Park, “Tensile deformation of a low density Fe–27Mn–12Al–0.8C duplex steel in association with ordered phases at ambient temperature,” *Materials Science and Engineering: A*, vol. 586, pp. 276–283, Dec. 2013.

[40] Y.-C. Lin, “Structures and superparamagnetic properties of overaged Fe–Al–Mn–C alloys,” *Acta Mater*, vol. 47, no. 18, pp. 4665–4681, Dec. 1999.

[41] C. C. Wu, J. S. Chou, and T. F. Liu, “Phase transformation in an Fe-10.1Al-28.6Mn-0.46C alloy,” *Metallurgical Transactions A*, vol. 22, no. 10, pp. 2265–2276, Oct. 1991.

[42] C. Y. Chao, C. N. Hwang, and T. F. Liu, “Grain boundary precipitation behaviors in an Fe-9.8Al-28.6Mn-0.8Si-1.0C alloy,” *Scr Mater*, vol. 34, no. 1, pp. 75–81, Jan. 1996.

[43] K. Lee, S.-J. Park, J. Moon, J.-Y. Kang, T.-H. Lee, and H. N. Han, “β-Mn formation and aging effect on the fracture behavior of high-Mn low-density steels,” *Scr Mater*, vol. 124, pp. 193–197, Nov. 2016.

[44] K. Lee *et al.*, “Effect of aging treatment on microstructure and intrinsic mechanical behavior of Fe–31.4Mn–11.4Al–0.89C lightweight steel,” *J Alloys Compd*, vol. 656, pp. 805–811, Jan. 2016.

[45] W. Song, W. Zhang, J. von Appen, R. Dronskowski, and W. Bleck, “κ-Phase Formation in Fe–Mn–Al–C Austenitic Steels,” *Steel Res Int*, vol. 86, no. 10, pp. 1161–1169, Oct. 2015.

[46] D. Field and K. Limmer, “Effect of Solution Treatment on Grain Size and Toughness of Lightweight Fe-Mn-Al-C Steel,” in *AISTech2019 Proceedings of the Iron and Steel Technology Conference*, AIST, pp. 2271–2280, May 2019.

[47] D. M. Field, K. R. Limmer, and B. C. Hornbuckle, “On the Grain Growth Kinetics of a Low Density Steel,” *Metals (Basel)*, vol. 9, no. 9, p. 997, Sep. 2019.

[48] W. K. Choo, J. H. Kim, and J. C. Yoon, “Microstructural change in austenitic Fe-30.0wt%Mn-7.8wt%Al-1.3wt%C initiated by spinodal decomposition and its influence on mechanical properties,” *Acta Mater*, vol. 45, no. 12, pp. 4877–4885, Dec. 1997.

[49] O. Acselrad, I. S. Kalashnikov, E. M. Silva, M. S. Khadyev, and R. A. Simao, “Diagram of phase transformations in the austenite of hardened alloy Fe-28% Mn-8.5% Al-1% C-1.25% Si as a result of aging due to isothermal heating,” *Metal Science and Heat Treatment*, vol. 48, no. 11–12, pp. 543–553, Nov. 2006.

[50] A. Prodhan and A. K. Chakrabarti, “A study on age hardening in cast Fe-Mn-Al-Si-C alloys,” *J Mater Sci*, vol. 25, no. 3, pp. 1856–1862, Mar. 1990.

[51] S. Bai *et al.*, “Research status and development prospect of Fe–Mn–C–Al system low-density steels,” *Journal of Materials Research and Technology*, vol. 25, pp. 1537–1559, Jul. 2023.

[52] J. Lee *et al.*, “Simulation of κ-Carbide Precipitation Kinetics in Aged Low-Density Fe–Mn–Al–C Steels and Its Effects on Strengthening,” *Metals and Materials International*, vol. 24, no. 4, pp. 702–710, Jul. 2018.

[53] L. Kang, H. Yuan, H. Li, Y. Ji, H. liu, and G. Liu, “Enhanced Mechanical Properties of Fe-Mn-Al-C Low Density Steel via Aging Treatment,” *Front Mater*, vol. 8, p. 680776, Jun. 2021.

[54] L. N. Bartlett, D. C. Van Aken, J. Medvedeva, D. Isheim, N. I. Medvedeva, and K. Song, “An Atom Probe Study of Kappa Carbide Precipitation and the Effect of Silicon Addition,” *Metallurgical and Materials Transactions A*, vol. 45, no. 5, pp. 2421–2435, May 2014.

[55] R. A. Howell, “Microstructural influence on dynamic properties of age hardenable FeMnAl alloys,” *Missouri University of Science and Technology - Doctoral Dissertations*, pp. 35–36, Jan. 2009.

[56] William D. Callister Jr. and David G. Rethwisch, “Materials Science and Engineering: An Introduction, 10th Edition,” *Wiley*, 2018.

[57] “ASTM E407 Practice for Microetching Metals and Alloys.” *ASTM International,* Nov. 2023.

[58] “Origin: Data Analysis and Graphing Software.”, Internet: https://www.originlab.com/index.aspx?go=Products/Origin, [Jun. 01, 2025].

[59] “E10 Test Method for Brinell Hardness of Metallic Materials.” *ASTM International*, Jul. 2023.

[60] “E8/E8M Standard Test Methods for Tension Testing of Metallic Materials.” *ASTM International*, Jul. 2025.

[61] “ImageJ.”, Internet: https://imagej.net/ij/, [Jul. 19, 2025].

APPENDICES

A. Microstructural Images Obtained With Different Etchants

Appendix A includes some microstructural images taken using different etchants. These etchants are 3% Nital, 5% Nital, 10% Nital and Vilella.

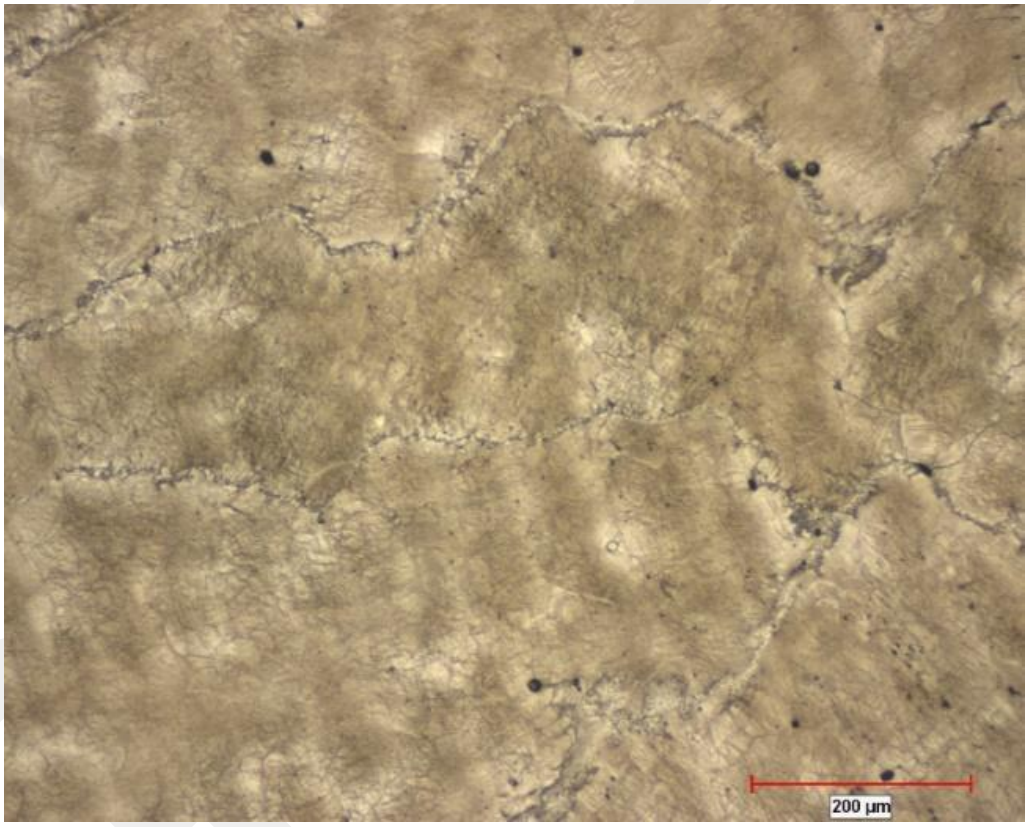

Figure A.1 As -cast microstructure etched with %3 Nital (100X)

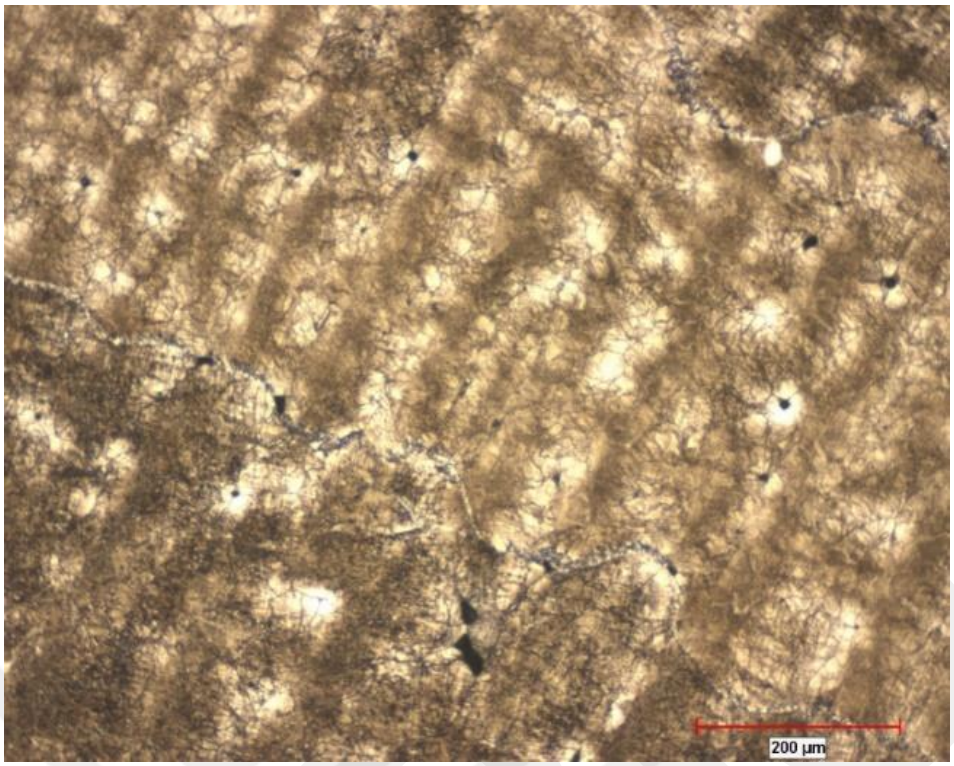

Figure A.2 As-cast microstructure etched with %5 Nital (100X)

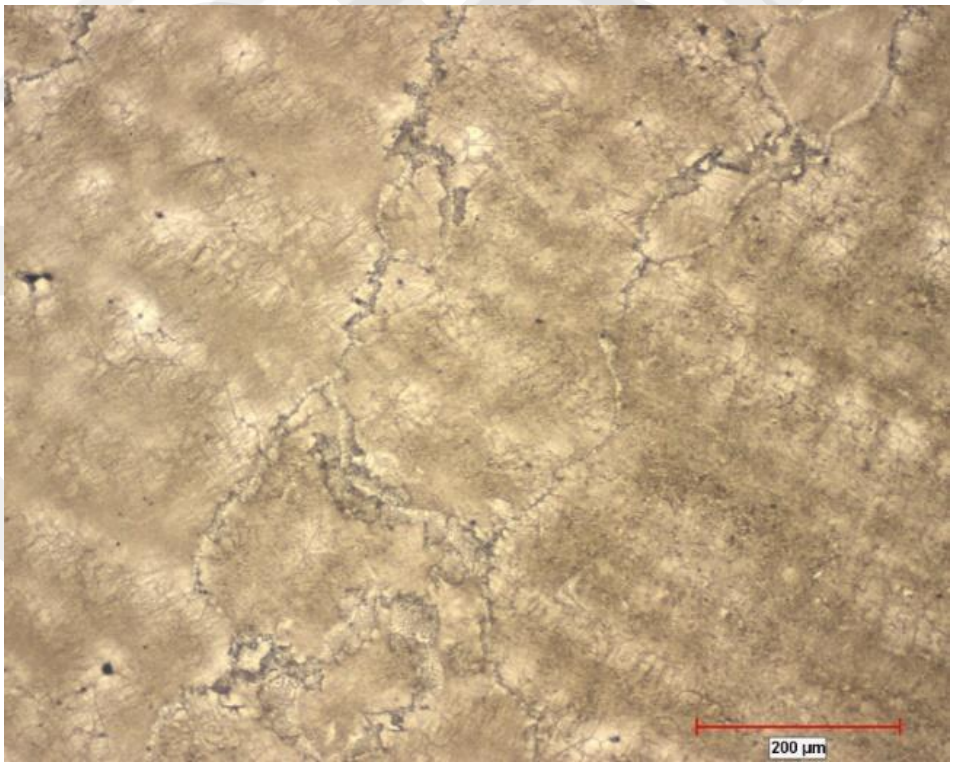

Figure A.3 As-cast microstructure etched with %10 Nital (100X)

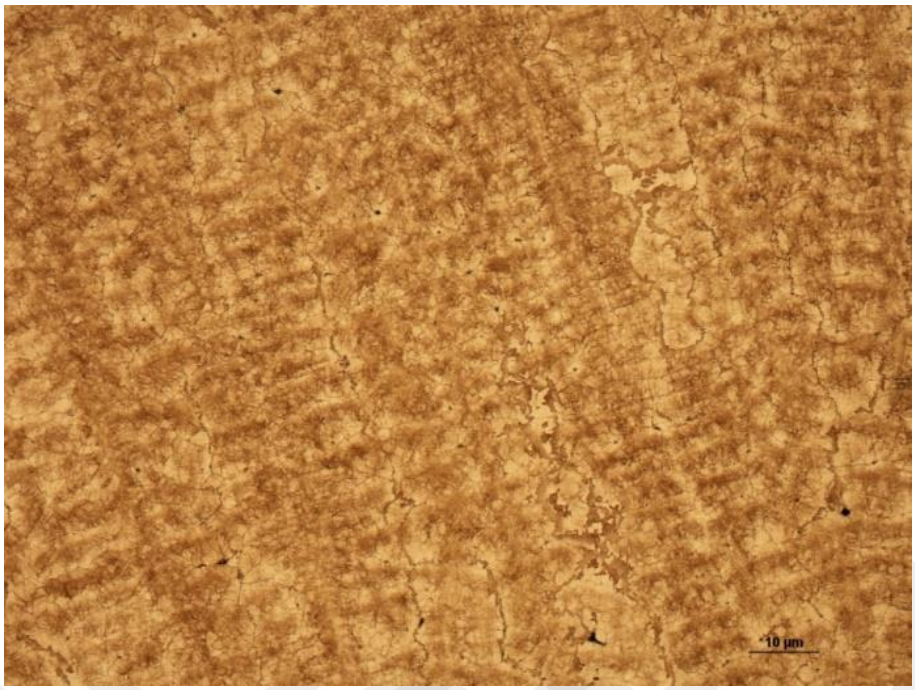

Figure A.4 As-cast microstructure etched with Vilella (100X)

After solution heat treatment at 1150°C, the samples were etched with 10% Nital and Vilella.

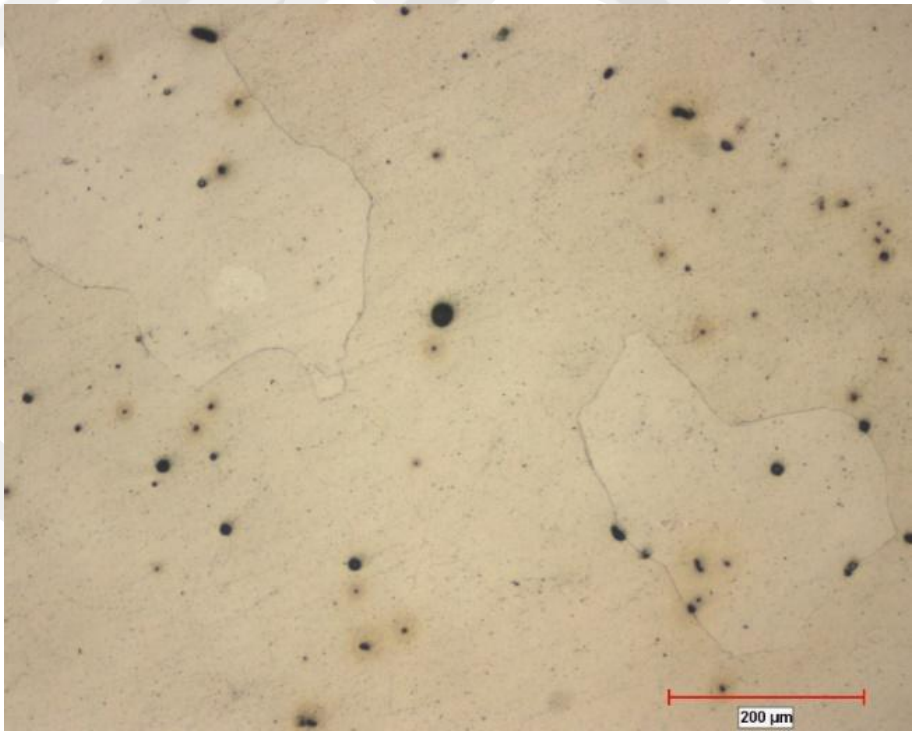

Figure A.5 Optical microstructural image of the sample solution heat treated at 1150°C for 2 hours, etched with %10 Nital (100X)

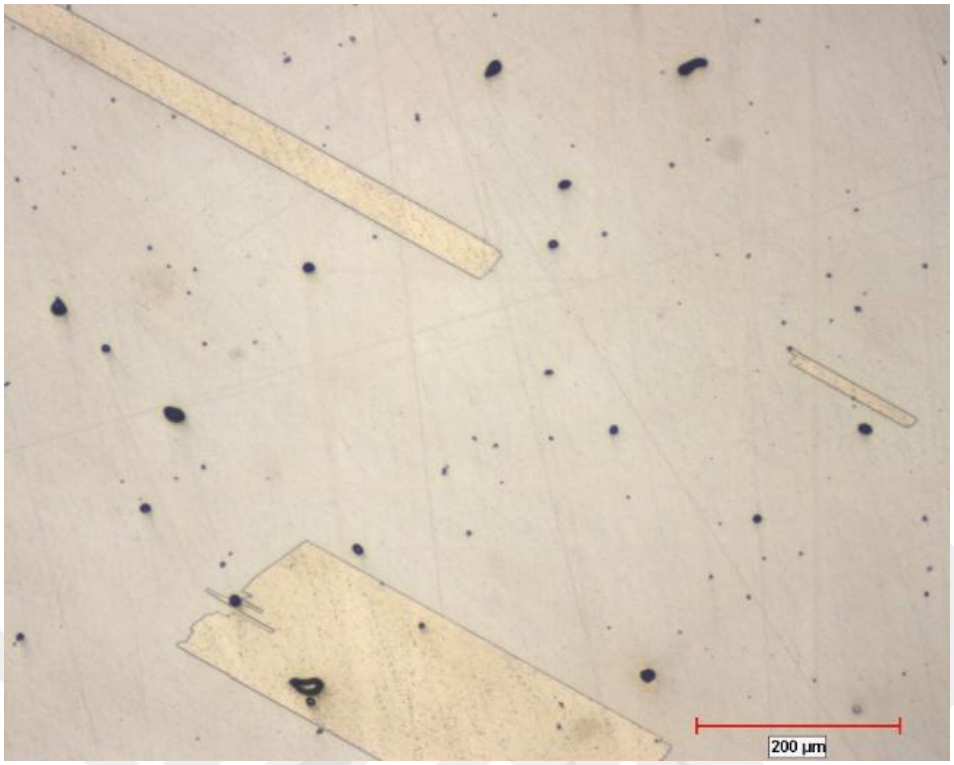

Figure A.6 Solution heat treatment at 1150°C for 2 hours, etched with Vilella (100X)

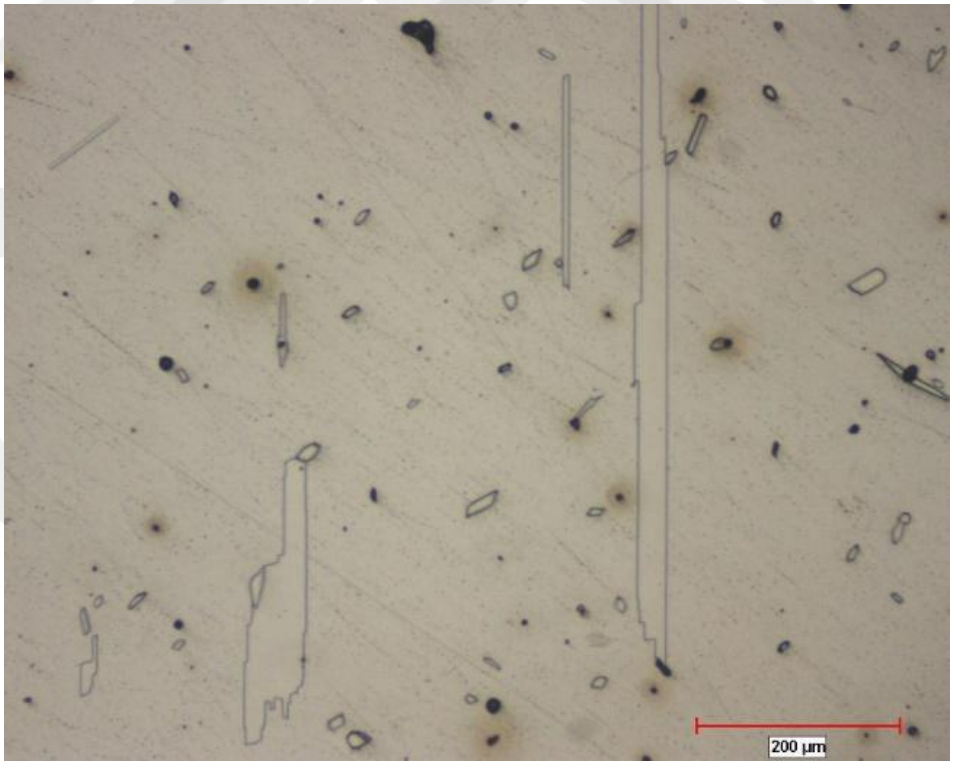

Figure A.7 Solution heat treatment at 1150°C for 4 hours, etched with %10 Nital (100X)

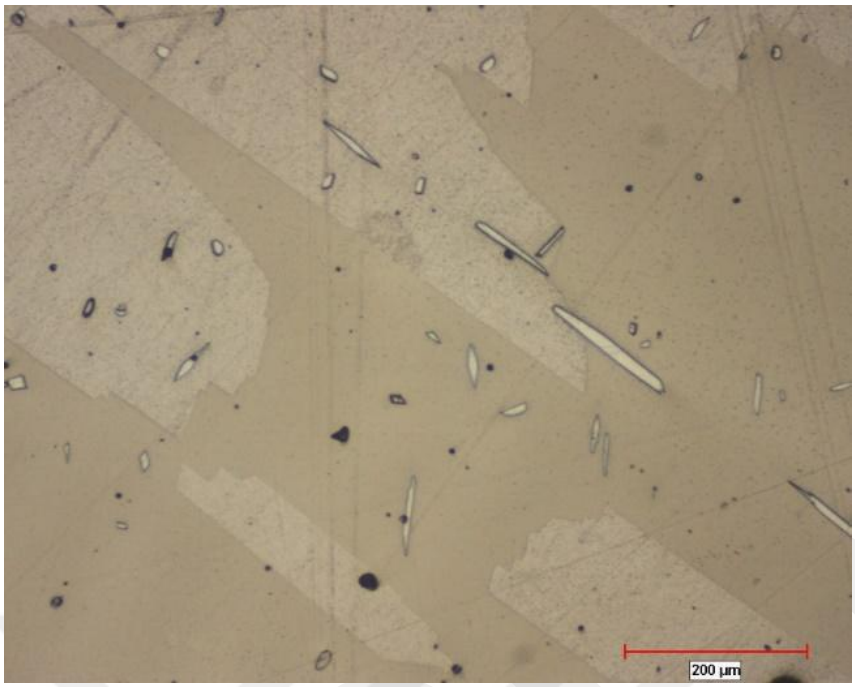

Figure A.8 Solution heat treatment at 1150°C for 4 hours, etched with Vilella (100X)

After the experiments, only Vilella was used to take the further microstructure images. For example, the microstructure image of the sample aged at 550°C for 16 hours after 4 hours of solution at 950°C was prepared with Vilella.

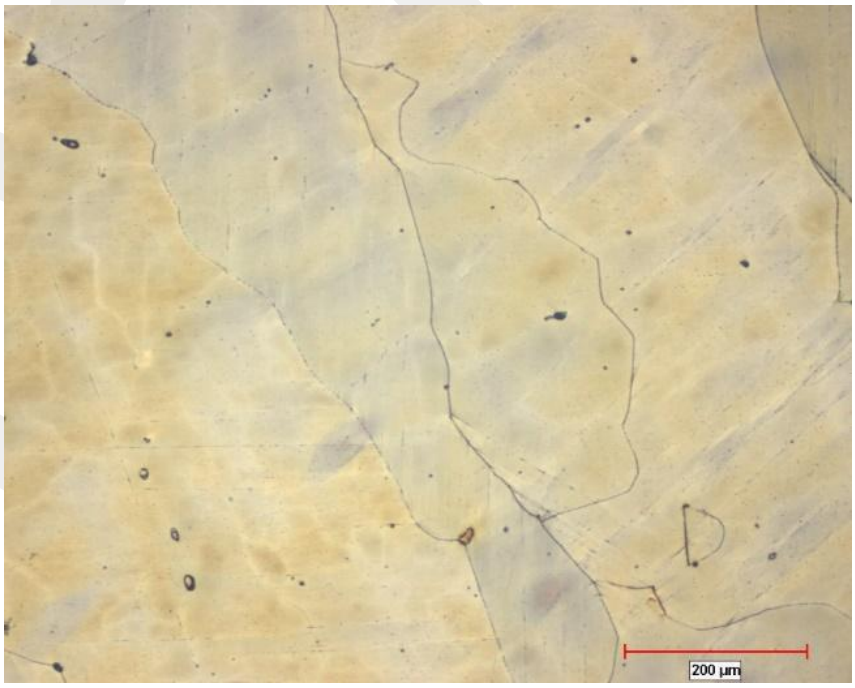

Figure A.9 ST at 950°C for 4 hours and aged at 550°C for 16 hours, etched with Villela (100X)

B. 3-Point Bending Test Results

3-point bending tests were performed with the *Instron 300DX* tensile/compression device at the Atılım University Metallurgical and Materials Engineering Department Laboratory (*Figure B.1*).

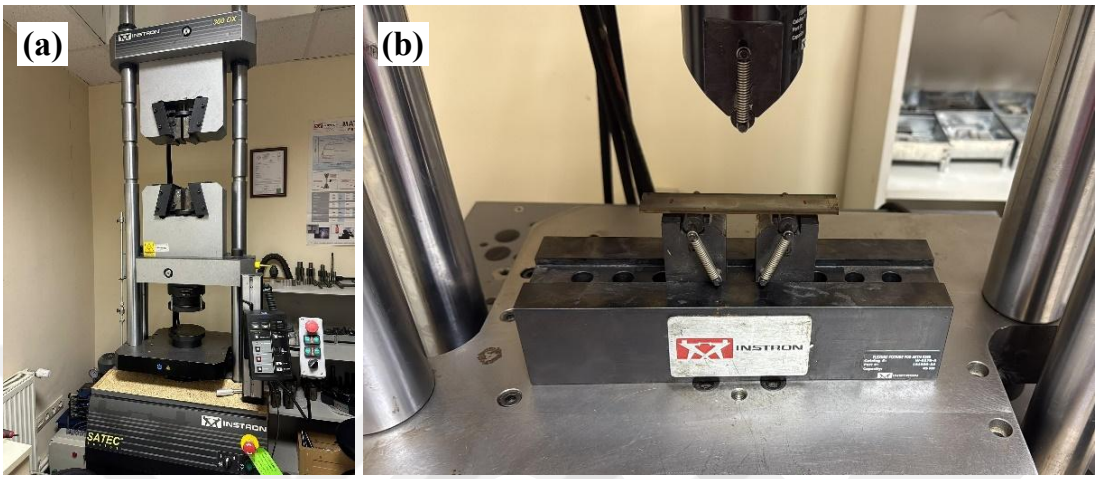

Figure B.1 3-point bending (a) test machine (b) sample placement

3-point bending test was performed on three as-cast samples. Sample images after the test are as shown in *Figure B.2*. Sample dimensions are 20 mm width, 2 mm thickness and 120 mm length. The distance between the supports is 60 mm.

Figure B.2 Sample after 3 point bending test

The results from the 3-point bending test on three different as-cast samples are presented in *Table B.1*.

Table B.1 As-cast sample 3 point bending test results

Sample	Comprasive Load (kN)	Maximum Compressive Displacement (mm)	Maximum Compressive Strain (%)	Fracture Displacement (mm)	Fracture Load (kN)	Fracture Strain (%)	0.2% Offset Yield Strain (%)
1	2.01	8.67	11.12	9.423	-0.07	12.09	11.12
2	1.58	7.43	9.53	8.221	-0.11	10.55	9.55
3	2.46	8.21	10.54	8.971	-0.15	11.51	10.35

The values obtained from the three-point bending test performed on the as-cast samples, together with the flexural strength values calculated using the formula in Equation (B.1), are summarized in *Table B2*.

$$\sigma = \frac{3FL}{2bd^2} \tag{B.1}$$

$\boldsymbol{F}$: $Force\ at\ fracture\ point\ (N)$

$\boldsymbol{L}$: $Support\ span\ length\ (mm)$

$\boldsymbol{b}$: $Width\ of\ the\ sample\ (mm)$

$\boldsymbol{d}$: $Thickness\ of\ the\ sample\ (mm)$

Table B.2 Flexural strength values calculated for the as-cast samples

Sample	**1**	**2**	**3**	**Average**
Fracture Load (kN)	0.07	0.11	0.15	**0,11**
Flexural Strength (MPa)	78.78	123.75	168.75	**123,76**

C. Worn Sample Profile Form Measurement

Figure C.1 shows the results for as-cast using the *Alicona InfiniteFocus* profile form measurement analysis method. Height step 1: 183.121 µm, height step 2: 12.930 µm, height step 3: 18.295 µm were measured.

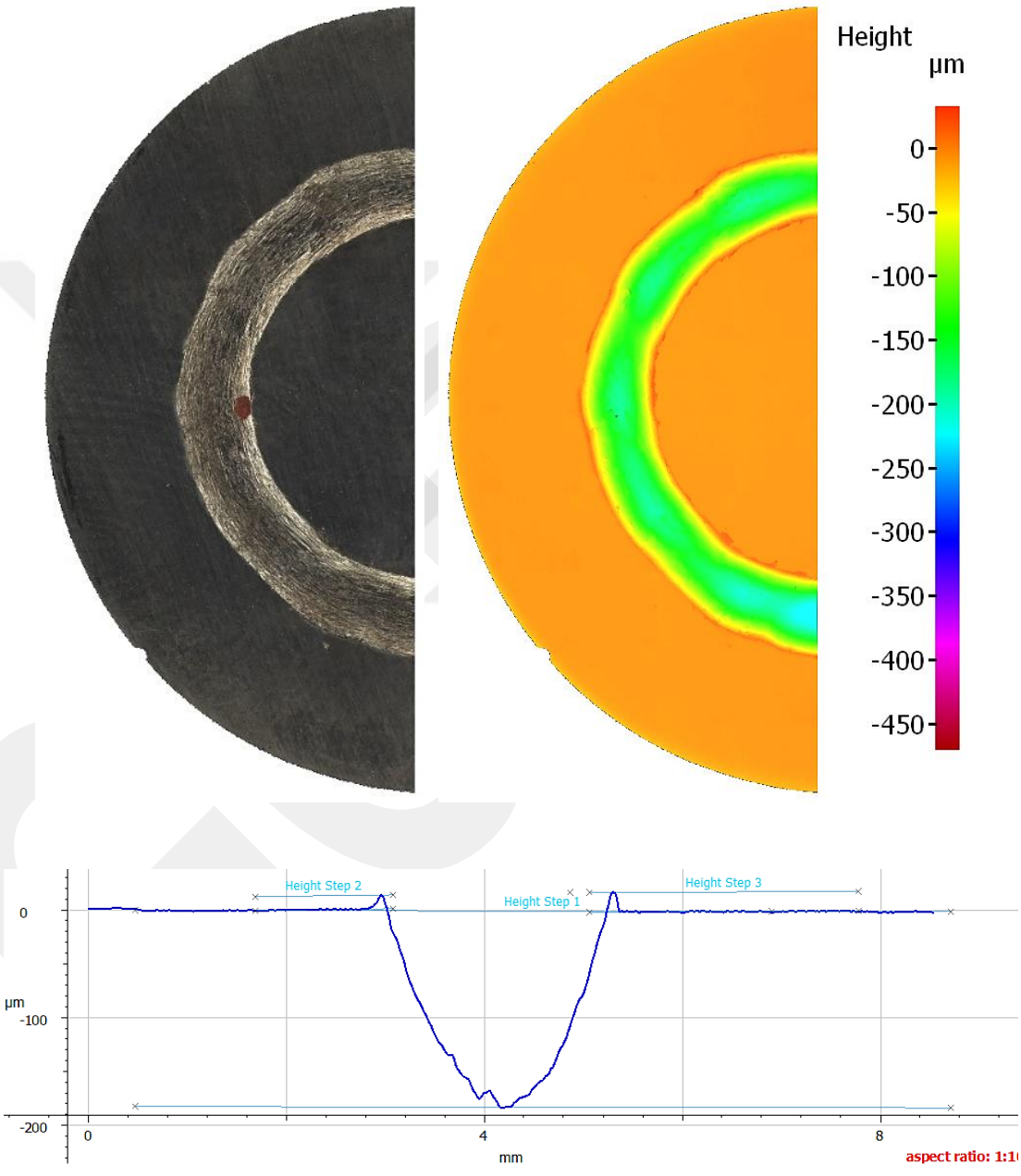

Figure C.1 Alicona profile form measurement analysis of as-cast worn sample

Figure C.2 shows the results for sample aged at 500°C for 16 hours after solution heat treatment at 1000°C for 4 hours using the *Alicona* profile form measurement analysis method. Height step 1: 161.848 µm, height step 2: 14.658 µm, height step 3: 10.764 µm were measured.

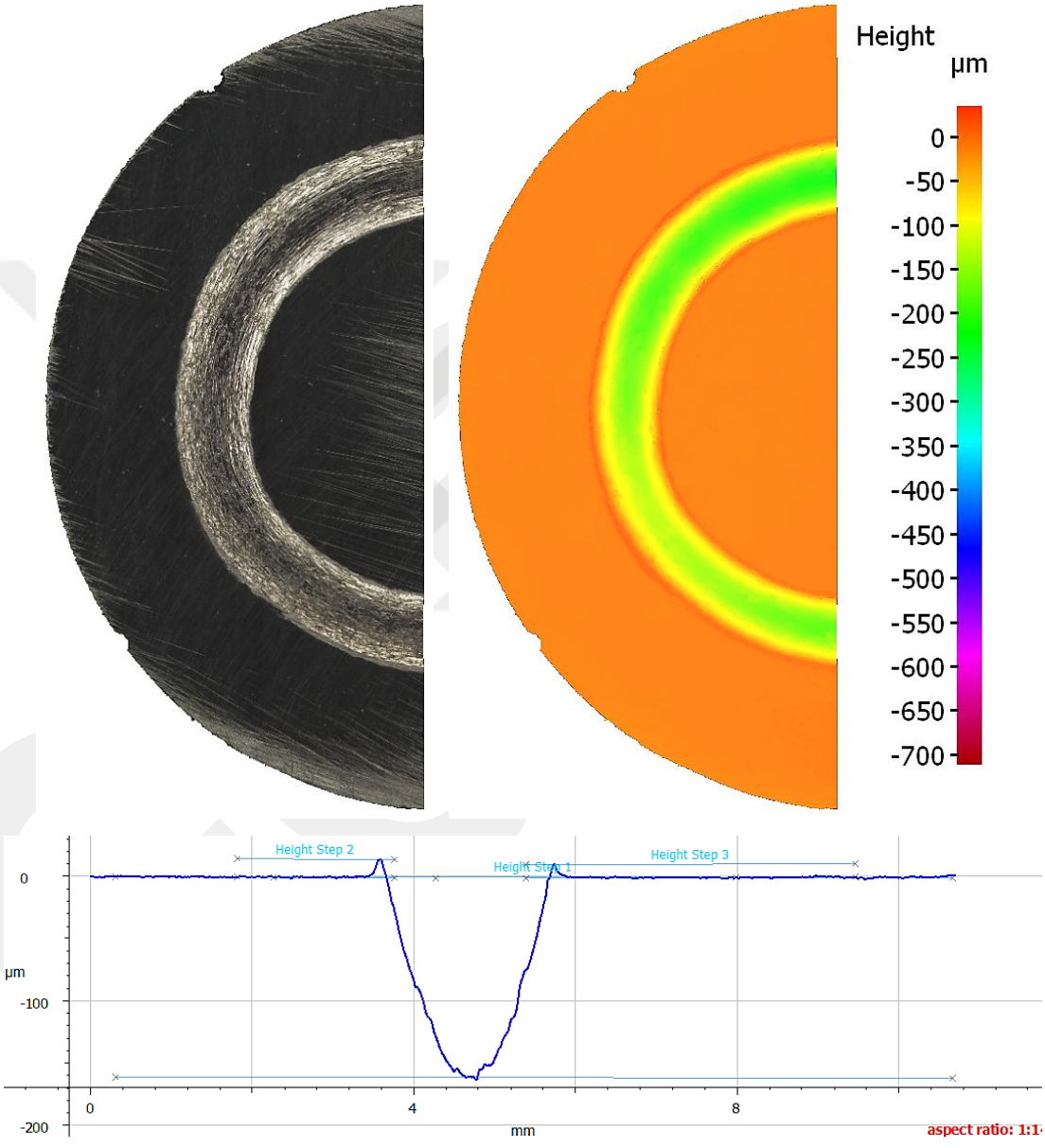

Figure C.2 Alicona profile form measurement analysis of the worn sample that was aged at 500°C for 16 hours after solution heat treatment at 1000°C for 4 hours